AFRL-OSR-VA-TR-2014-0240

STUDYING THE DEPENDENCY OF INTERFACIAL FORMATION WITH CARBON NANOTUBE

MARILYN MINUS
NORTHEASTERN UNIVERSITY

08/27/2014
Final Report

Air Force Research Laboratory
AF Office Of Scientific Research (AFOSR)/ RTD
Arlington, Virginia 22203
Air Force Materiel Command

REPORT DOCUMENTATION PAGE

Form Approved
OMB No. 0704-0188

1. REPORT DATE *(DD-MM-YYYY)*
23-08-2014

2. REPORT TYPE
Final Report

3. DATES COVERED *(From - To)*
07/1/2011 to 06/30/2014

4. TITLE AND SUBTITLE
Studying the Dependency of Interfacial Formation with Carbon Nanotube

5a. CONTRACT NUMBER

5b. GRANT NUMBER
FA9550-11-1-0153

5c. PROGRAM ELEMENT NUMBER

6. AUTHOR(S)
Dr. Marilyn Minus

5d. PROJECT NUMBER

5e. TASK NUMBER

5f. WORK UNIT NUMBER

7. PERFORMING ORGANIZATION NAME(S) AND ADDRESS(ES)
Northeastern University
360 Huntington Avenue
Boston, MA 02115-5005

8. PERFORMING ORGANIZATION REPORT NUMBER
N/A

9. SPONSORING / MONITORING AGENCY NAME(S) AND ADDRESS(ES)
USAF, DUNS DUNS143574726
AF Office of Scientific Research
875 North Randolph Street, RM 3112
Arlington, VA 22203

10. SPONSOR/MONITOR'S ACRONYM(S)
AFOSR

11. SPONSOR/MONITOR'S REPORT NUMBER(S)
N/A

12. DISTRIBUTION / AVAILABILITY STATEMENT

Approved for Public Release

13. SUPPLEMENTARY NOTES
N/A

14. ABSTRACT

The proposed work was focused on understanding the capabilities of polymeric materials to form interfacial structures around carbon nanotubes and other nano-carbon materials. The proposed effort led to the development of a new processing route for dispersing nano-carbons in dilute polymer solutions. This dispersion process involved steps of sonication, shearing, and crystallization. The specific combination of these processes resulted in the formation of polymer interfacial growth (i.e., interphase structures) on the nano-carbon surfaces. The interphase formed consisted of either extended-chain or folded-chain polymer crystals depending on the processing route used. This processing approach for the dispersion of nano-carbons and formation of polymer interphase was implemented into fiber processing procedures. In general, these studies showed that the inclusion of interphase structures in the composite fibers led to dramatic increases in the mechanical properties. Beyond mechanical enhancement, the composite fiber morphology was also examined to understand the fundamental links between the processing route use and the resultant structure-property relationship.

15. SUBJECT TERMS
Carbon Nanotube, polymer, interphase, interfacial, crystallization, composite

16. SECURITY CLASSIFICATION OF:
a. REPORT U
b. ABSTRACT U
c. THIS PAGE U

17. LIMITATION OF ABSTRACT
UU

18. NUMBER OF PAGES

19a. NAME OF RESPONSIBLE PERSON
Marilyn Minus

19b. TELEPHONE NUMBER *(include area code)*
617-373-2608

Standard Form 298 (Rev. 8-98)
Prescribed by ANSI Std. Z39.18

FINAL REPORT

STUDY THE DEPENDENCY OF INTERFACIAL FORMATION WITH CARBON NANOTUBE

GRANT/CONTRACT NUMBER:
FA9550-11-1-0153

DATES COVERED:
07/01/2011 to 06/30/2014

PRINCIPAL INVESTIGATOR (PI):
Dr. Marilyn L. Minus
Department of Mechanical and Industrial Engineering
Northeastern University, Boston, MA, USA

PROGRAM MANAGER:
Dr. Joycelyn Harrison
Low Density Materials

ABSTRACT

The proposed work was focused on understanding the capabilities of polymeric materials to form interfacial structures around carbon nanotube and other nano-carbon materials. The proposed effort led to the development of a new processing route for dispersing nano-carbons in dilute polymer solutions. This dispersion process involved steps of sonication, shearing, and crystallization. The specific combination of these processes resulted in the formation of polymer interfacial growth (i.e., interphase structures) on the nano-carbon surfaces. The interphase formed consisted of either extended-chain or folded-chain polymer crystals depending on the processing route used. This processing approach for the dispersion of nano-carbon and formation of polymer interphase was implemented into fiber processing procedures. Polymer materials used in these composite fiber studies include polyacrylonitrile (PAN), polyvinyl alcohol (PVA), and polyethylene (PE). The nano-carbons include carbon nanotubes (CNT) and carbon nano-chips (CNC) (i.e., platelet morphology). In addition, boron nitride platelets were also studied. Several process modifications were made to the fiber spinning procedure to ensure the formation of interphase structures within the composites. It was found that polymer crystal growth should be well-controlled to form a desired interphase morphology. For this reason, crystallization studies were also performed for all the polymers used in the presence of the nano-materials. In general these composite fiber studies showed that the inclusion of interphase structures in the composite fiber led to dramatic increases in the mechanical properties. Beyond mechanical enhancement, the composite fiber morphology was also examined to understand the fundamental links between the processing route use and the resultant structure-property relationship.

SECTION I: RESULTS RELATED TO OBJECTIVES 1

Objective 1: Investigate the dependency of interfacial formation and structure on the increase of the single-wall carbon nanotube (SWNT) length in the composite fiber.

In general, the *Objectives 2* to *4* are all linked to *Objective 1*. Sections II to IV outlines the various studies performed over the duration of this project toward understanding the interfacial formation and dependency on SWNT and its relationship to the nanotube length.

SECTION II: RESULTS RELATED TO OBJECTIVES 2

Objective 2: Investigate the influence of current state-of-the-art processing steps for polymer nano-composites (e.g. sonication and homogenization) on the morphology and its effect on the nano-inclusion structure (i.e. breaking down the SWNT length).

***Relationship to Objective 1: Understanding the change of CNT length during dispersion processing.*

II.1. SWNT Dispersion Study

This study focuses dispersion of carbon nanotubes in solvent by sonication. The general goal was to get an understanding regarding the population distribution of SWNT dispersed in a solvent in terms of the length, bundle diameter, and extend of exfoliation.

Experimental Section

Materials

Vertical SWNT array (~1 mm in length, 1-5 nm in diameter)[1] used in this work was obtained from the Center for High-Rate Nanomanufacturing (CHN) at Northeastern University. SWNT powder was obtained from Cheaptubes Inc. (5-30 μm in length, 1-2 nm in diameter and purity >90 wt%, as reported by manufacturer). DMF (CAS# 68-12-2) solvent was purchased from Fisher Scientific. All materials were used as received without further modification.

Solution Preparation

SWNT array and SWNT powder samples were sonicated in DMF using a Fisher F530 bath sonicator (frequency 43 kHz, power 150 W). A SWNT concentration of 20 mg/L was used in all cases. Samples were removed from dispersion sonicated at time intervals of 30 (optically uniform solution first observed), 48, 72 and 96 hrs, respectively. The dispersion samples were diluted to 20 times the original concentration by DMF for subsequent characterization.

Sample Characterization

Microscopy characterization was performed on Zeiss Supra 25 Field Emission SEM (operating voltage 5 kV). All solution samples were dried on polished silicon wafers for imaging analysis. Raman spectroscopy was conducted on a Jobin Yvon LabRam HR800 (laser wavelength 532 nm). For X-ray analysis, thin films were prepared by drying the undiluted solution samples in a vacuum oven. Some samples could not form free-standing films, and therefore the material was placed into quartz capillaries (purchased from Hampton Research, Cat# HR6-140, wall thickness 0.7 mm) for XRD tests. SAXS experiments were performed directly on the SWNT dispersions placed in quartz capillary tubes. SAXS patterns were analyzed using Rigaku NANO-Solver^{TM} (version 3.6) software.

Results and Discussions

Homogeneous dispersion of SWNT is exceedingly important for fabrication of composites. Processing results in tube damages, therefore, preservation of the nanotube structure is of critical importance to producing composites with high mechanical performance. SWNT dispersion experiments were carried out in N, N dimethylformamide at a concentration of 20 mg/L. Characterization of the tube breakdown during dispersion was conducted using microscopy and spectroscopy. Statistical analysis of the length distribution was accomplished versus sonication time. Nanotube debundling and reaggregation during sonication were investigated through SWNT bundle diameter distribution analysis performed by small-angle X-ray scattering. It was found that two distinct populations of SWNT existed in sonicated dispersions. Bundle size distributions indicate a population of well-exfoliated SWNT bundles as well as a population of large SWNT ropes due to hierarchical rearrangement. It was also found that both shortening and reaggregation of SWNT changed as a function of processing time.

Initial Characterizations of the As-received SWNT Materials

Electron microscopy images of the as-received SWNT powder and array are shown in Figures 2.1a and 2.1b, respectively. Raman spectra (Figure 2.1c) shows a high D/G ratio for SWNT array sample as compared to that for the powder samples, which indicates a large presence of graphitic defects in the graphitic structure or disordered carbon structure for the array. These defective structures may act as weak points during dispersion causing tube shortening due to fracture.

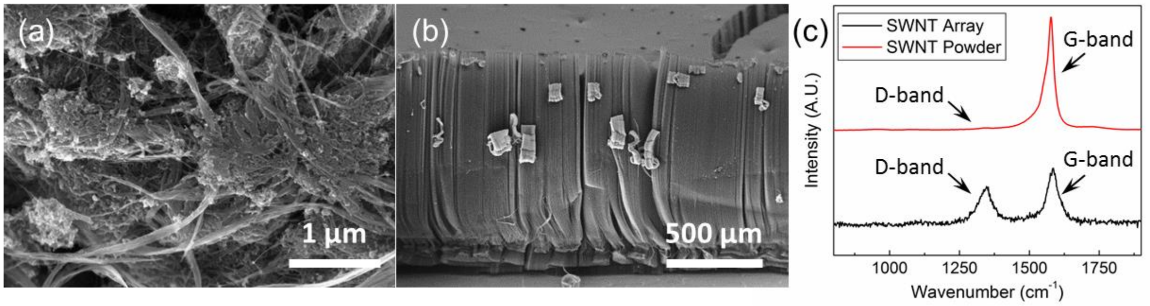

Figure 2.1. *Scanning electron micrographs of (a) as-received SWNT powder, and (b) cross-section of SWNT array. (c) Raman spectra of as-obtained SWNT powder and array.*

SWNT Length Breakdown as a Function of Processing Time

Figures 2.2a, 2.2b and 2.2c are some typical SEM images of the dispersed SWNT dried from diluted sonicated solutions, representing the morphological diversity, especially in length and bundle size, for different SWNT materials after processing. The shortening process of nanotubes is analyzed separately for long (> 1 µm) and short (< 1 µm) tubes. After 30 hrs sonication, the average lengths of nanotubes are similar regardless of the starting length of the powder or the array as shown in Figure 2.2d. Large standard deviations are found for the length distribution of both nanotubes after sonication. The overall average length of SWNT powder decreases with sonication time and reaches a plateau beyond 48 hrs (Figure 2.2e). However, the average length of SWNT array continues decreasing although at a lower rate after 48 hrs (Figure 2.2f). The drastic breakdown of the array tubes before 30 hrs and the continuous breakdown beyond 48 hrs may be due to the presence of higher defective graphitic content in the original sample, as evidenced by the D-band in the Raman spectroscopy (Figure 2.1c). For both SWNT materials, the longer tubes continue to break at a slower rate with prolonged sonication, while the shorter tubes generally maintain a constant average length despite processing time (Figures 2.2e and 2.2f). It is assumed that at a fixed sonication power, the shearing forces generated around nanotubes diminish with the decrease of nanotube length and eventually reach a critical value, where tube breakage no longer occurs.[2] The group of shorter tubes also consists of many small CNT fragments (<< 300 nm). This population of fragmented SWNT pieces may behave as defects in the composite fibers since their alignment is not easily controllable.

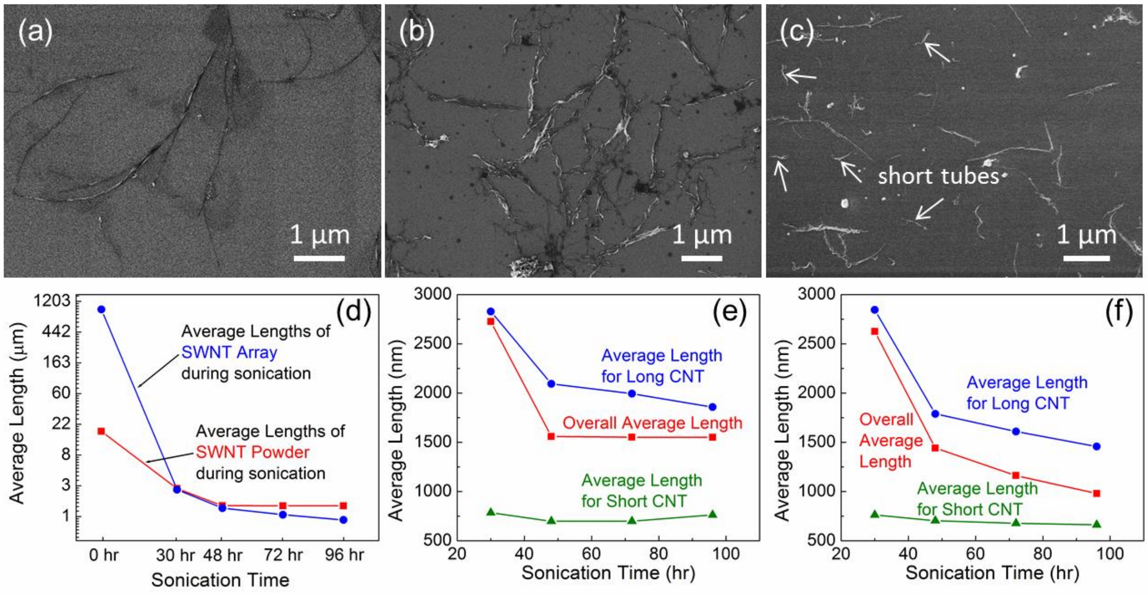

Figure 2.2. *Typical SEM images of (a) dispersed SWNT powder, (b) large bundles and (c) small bundles of dispersed SWNT array. SWNT length breakdown as a function of sonication time: (d) log plot of average SWNT length from powder and array (0 to 96 hr); (e) average length of SWNT from powder (30 to 96 hr); (f) average length of SWNT from array (30 to 96 hr).*

Hierarchical Reorganization of Dispersed SWNT

Observations from Figures 2.3a and 2.3b indicate that for sonicated dispersions left unperturbed, reaggregation of the nanotubes increase as a function of processing time for both SWNT materials used. SAXS analysis of the SWNT dispersions for each sample reveals two dominant peaks which correspond to the distributions of tube bundle sizes. Bundle size (Figure 2.3c) and population (Figure 2.3d) distributions as a function of sonication time indicated that dispersions containing shorter tubes displayed both faster reaggregation rate and a higher degree of aggregation. The reason for SWNT bundle reaggregation is assumed to be related to the attraction of the tubes by van der Waals forces and their ability to pack in a crystalline trigonal (2D hexagonal) arrangement.[3] The crystalline nature of these tube bundles moving from a pseudo-hexagonal (low order) to a trigonal (high order) crystalline symmetry becomes more pronounced with tube uniformity in terms of diameter and reduced curvature due to length reduction. During sonication, in addition to tube exfoliation the length is also reduced. This mechanism facilitates the reaggregation of the tubes into more ordered bundles at faster rates. Based on SAXS study of the bundle size and populations, it is concluded that 48 hrs sonication leads to the best exfoliation for both SWNT types. Sonication beyond 48 hrs is not suggested due to the increase of bundle size and the population of large bundles (i.e., reaggregation effect).

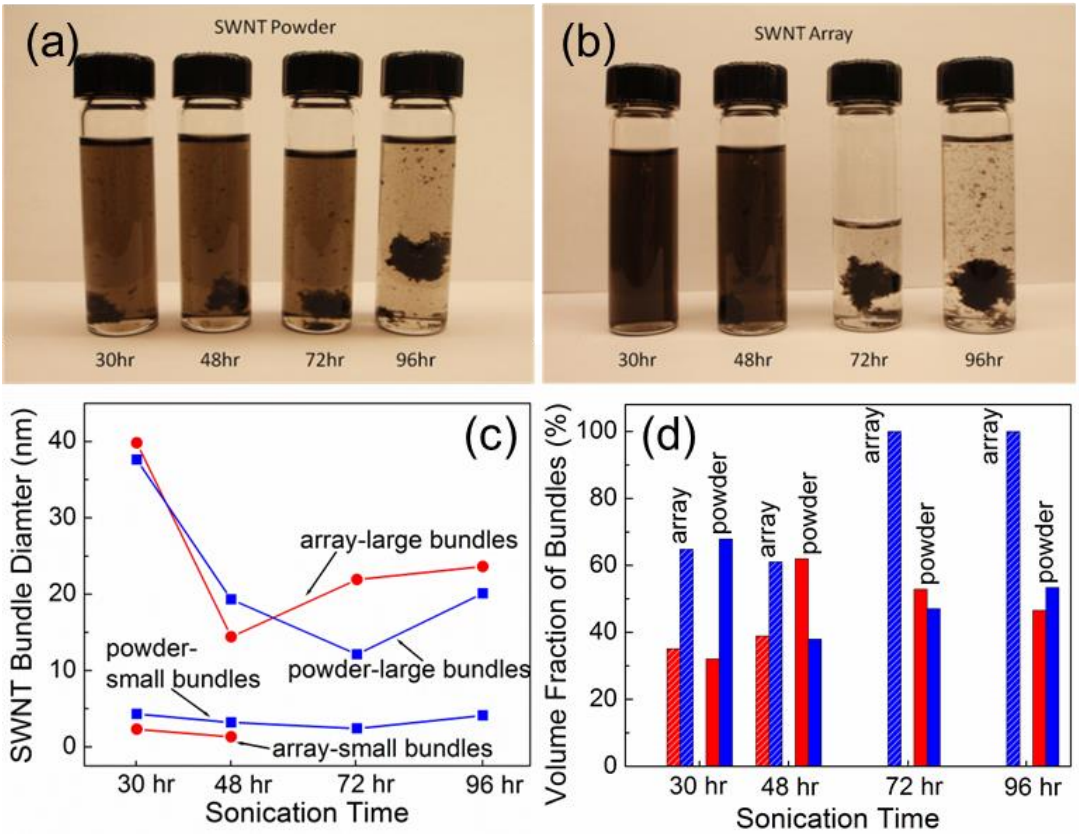

Figure 2.3. *SWNT reaggregation as a function of sonication time for both (a) powder and (b) array samples. SAXS data for SWNT reaggregation in terms of (c) SWNT bundle diameter distribution and (d) change in SWNT bundle volume fractions (red bars for small bundles and blue bars for large bundles).*

Conclusions

Regardless of the original SWNT length, 30 hrs sonication breaks both tubes to a similar level (~2.8 µm). The average length of SWNT powder reaches a plateau after 48 hrs; while SWNT array continues scission though at a low rate. The presence of intrinsic defects shown by Raman spectroscopy indicates the reason for the initial drastic breakdown and the continuous shortening of the array tubes. XRD analysis of bundle diameter suggests best exfoliation is obtained after 48 hrs of sonication. The nanotube agglomeration becomes more pronouced with sonication time, indicating hierarchical rearrangement due to the increased tube crystalline symmetry.

SECTION III: OBJECTIVE 3

Objective 3: Design new non-chemical processing regimes to effectively process polymer SWNT dispersions while hindering breakage of the carbon nanotubes (CNT).

***Relationship to Objective 1: Understanding the formation of interfacial structures as CNTs are dispersed in polymer solutions.*

III.1. POLYMER-ASSISTED DISPERSION

This study focuses dispersion of carbon nanotubes in polymer solutions. The polymers used for the dispersions are consistent with the composite matrix material. These dispersion studies are used to understand the fundamental molecular interactions between the polymer and CNT toward forming interfacial structures (i.e., interphase).

Experimental Section

Materials

The SWNT materials used here include cheaptubes (CT) SWNT obtained from Cheaptubes Inc. (purity >90 wt%, Raman spectrum G/D ratio ~7.4) and super purified (SP) SWNT from Continental Carbon Nanotechnologies, Inc. (purity ~98.9 wt%, Raman spectrum G/D ratio ~18.4). Based on SEM and HR-TEM observations, CT powder contains additional carbonaceous species (i.e., onions and carbon black. PAN (molecular weight ~520,000 g /mol) was obtained from Exlan Co., Japan. PVA (molecular weight ~ 352,000 g/mol) was obtained from Kuraray Co. Ltd, Japan. DMF (CAS# 68-12-2) and dimethyl sulfoxide (DMSO) (CAS# 67-68-5) solvents were purchased from Fisher Scientific. All materials were used as received without further modification.

Solution Preparation

Dilute polymer solutions were prepared by dissolving PAN and PVA in DMF and DMSO respectively at 90 °C. The as-received SWNT material was added to this 90 °C-PAN/DMF solution and the SWNT/PAN/DMF mixture was then transferred into a water bath for 24 hr sonication. Bath sonication was conducted using Fisher F530 bath sonicator (frequency 43 kHz, power 150 W). Some dispersion solutions were subject to a post-processing stage with shearing, while some other solutions after sonication were subsequently dried under various conditions. The optimized processing methods will be discussed in detail in the next section. The dispersions were diluted to 20 times their original concentration by same solvent for characterization. All diluted SWNT dispersions (i.e., solvent only and polymer solutions) were drop casted and dried in a vacuum oven at room temperature (22 °C) for analysis.

Sample Characterization

Microscopy characterization was performed on Zeiss Supra 25 Field Emission SEM (operating voltage 5 kV). All SEM samples were dried on polished silicon wafers and sputter coated with gold/palladium for image analysis. High-resolution TEM images were taken by a JEOL 2010 Advance High Performance TEM (operating voltage: 200 kV). TEM samples were prepared using loop tool (Electron Microscopy Sciences, Cat# 70944) to place droplets of solution samples onto lacey carbon coated copper grids (Electron Microscopy Sciences, Cat# LC200-Cu). Lattice spacing measurements from TEM images were calibrated using a graphitized carbon black standard (Electron Microscopy Sciences, Cat# 80037). WAXD was performed on a Rigaku RAPID II curved detector X-ray diffraction system equipped with a 3 kW sealed tube source (operating voltage 40 kV and current 30 mA). For X-ray analysis thin film samples were prepared by drying the PAN/SWNT solutions in a vacuum oven. XRD curve fitting and analysis was performed using softwares PDXL 2 (version 2.0.3.0) and 2DP (version 1.0.3.4).

Results and Discussions

Dispersing SWNT in dilute polymer solutions largely improve dispersion quality and stability due to the formation of interfacial polymer coating on SWNT. In order to improve stress transfer between polymer matrices and nano-fillers, controlling the structure development in the interphase region during composite processing is a necessity. For PAN/ SWNT composites, the formation of the PAN interphase in the presence of the SWNT as a function of processing conditions is studied. Under these conditions three distinct interfacial coating morphologies of PAN are observed on SWNT. In the semi-dilute polymer concentration regime subjected to shearing, PAN extended-chain tubular coatings are formed on SWNT. Dilute PAN/SWNT quiescent solutions subjected to cooling yields hybrid periodic shish-kebab structures (first observation for PAN polymer); and dilute PAN/SWNT quiescent solutions subjected to rapid cooling results in the formation of an irregular PAN crystalline coating on the SWNT. PVA tubular coating is also formed under similar processing conditions.

Polymer-Assisted SWNT Dispersion

In order to prevent SWNT reaggregation without introducing other components into the SWNT/polymer system, the matrix polymer was used to help SWNT dispersion, since polymer chains are capable to wrap around CNT to form a coating layer. Moreover, the addition of polymer into the solvent will increase the solution viscosity, which could potentially reduce the tube breakdown by cavitation forces. To compare the role of the polymer in assisting SWNT dispersion, SWNT were dispersed in DMF and dilute PAN/DMF solutions using sonication respectively. The dispersions were subsequently left unperturbed at room temperature for 12 hrs after sonication. Figure 3.1a shows a distinct difference in solution stability and uniformity. SWNT dispersed in pure solvent largely precipitated, indicating that the tubes prefer self-interaction and reaggregation into bundles. However, SWNT dispersed in dilute PAN solution remained suspended in solution, resulting in a very uniform and stable dispersion for several weeks before visible precipitates were observed. PVA-assisted SWNT dispersion showed similar results (Figure 3.1b).

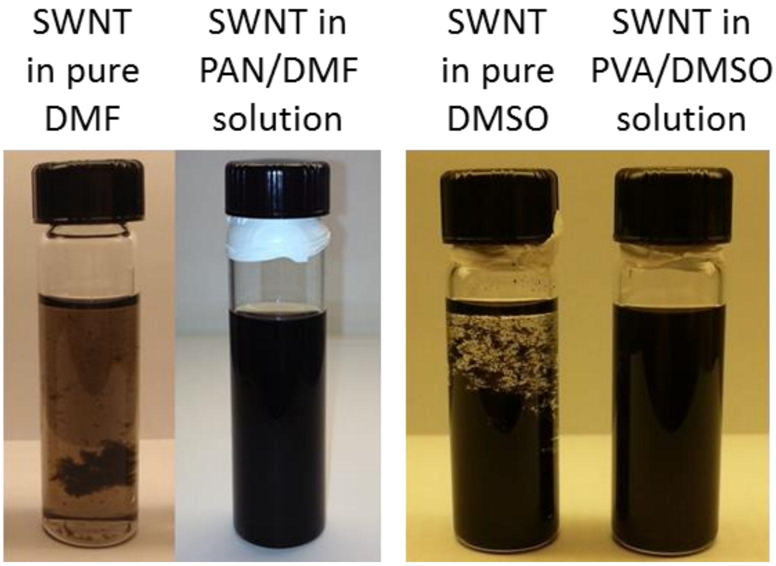

Figure 3.1. *Observations of (a) SWNT/DMF solution and PAN/SWNT/DMF solution, and (b) SWNT/DMSO solution and PVA/SWNT/DMSO solution, left unperturbed for 12 hrs.*

Characterizing the length distribution of SWNT dispersed in polymer solution is quite challenging by electron microscopy. Since the tube or bundles are coated or covered by polymer on the substrate, very rarely can the entire bundle be observed clearly under the microscope. The bundles and tubes overlap making it difficult to following it end-to-end, and many images must be obtained to achieve statistically relevant information. For this reason, not enough data points can be obtained for analysis of the SWNT length distribution. However, the SEM investigation does enable the observation of various polymer coating morphologies on the SWNT (Figures 3.2a to 3.2e).

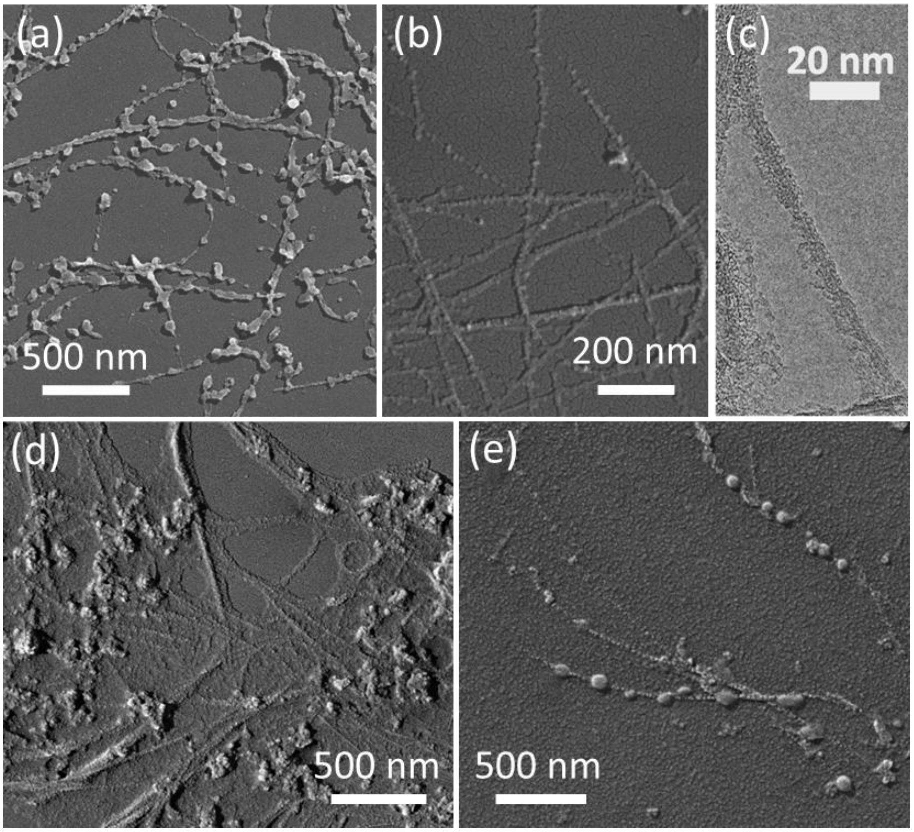

Figure 3.2. *(a) and (b) SEM images of SWNT dispersion in dilute PAN/DMF solutions. (c) TEM image showing PAN coating layer formed around SWNT. (d) and (e) SEM images of SWNT dispersion in dilute PVA/DMSO solutions.*

It is believed that during the exfoliation-reaggregation process driven dynamically by sonication, while the bundles are being exfoliated, the polymer chains wrap around them due to polymer-SWNT interactions. This increases the energy barrier during the exfoliated tubes to rebundle. Polymer wrapping on the SWNT also enable the formation of coatings on the tubes, which prevents the debundled SWNT to reaggregate into 2D-crystalline arrangement. Figures 3.2a to 3.2e are SEM and TEM images of dried polymer/CNT solutions, which reveal the polymer-SWNT coating at nano-scale. PAN or PVA coatings with differing morphologies can be clearly observed in the vicinity of nanotubes or bundles. These include random wrapping of PVA polymer around SWNT (Figure 3.2d), PAN '*blobs*' (Figure 3.2a) and PVA '*blobs*' (Figure 3.2e) on SWNT bundles, the initial nucleation of PAN '*kebabs*' on SWNT '*shish*' (Figure 3.2b), and the tubular interphase coating along the nanotube (Figure 3.2c). These polymer coatings prevent reaggregation and enable the tubes to stay suspended in solution.

Controlled Growth of Interphase PAN Structure on SWNT

Further refining the processing approaches, the methods for forming tubular, *kebab* and *blob* coating structures are summarized in Figure 3.3 and Table 3.1. Each solution was prepared in three major steps: (1) sonication (to improve polymer-SWNT dispersion), (2) post-processing shearing (to induce fibrillar crystal nucleation), and (3) cooling (to induce polymer crystallization). The sonication bath temperature was controlled within the range of 55 to 90 °C. In Figure 3.3, samples in process (a) were the only ones subjected to a post-processing (shearing) step; in process (b), the original sonicated solution was diluted to 20-fold with solvent at temperature (T_o) before cooling to room temperature (22 °C); in process (c) samples were diluted to 20 times the original volume with (22 °C) solvent, then allowed to equilibrate at ~20 °C. The results in this section show how these procedures lead to the growth of specific polymer interfacial morphologies in the presence of SWNT.

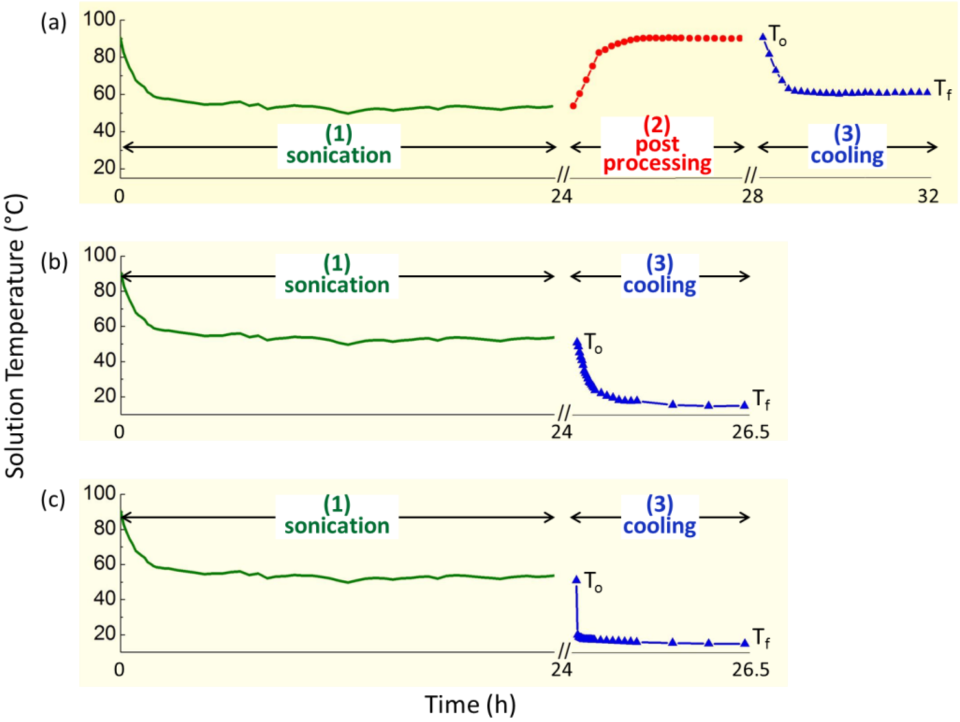

Figure 3.3. Graphical representation of the solution temperature change as a function of processing time for the polymer/SWNT solutions. All solution processing stages (1) sonication (2) post processing and (3) cooling were temperature controlled.^{6}

As processing parameters are well controlled, the resulting interfacial morphologies are tailored to specific types (Figure 3.4). By comparing these PAN interphase morphologies, it was found that semi-dilute PAN/SWNT solutions slow cooled under shear force (Figure 3.3a) resulted in the formation of extended-chain crystals at the PAN-SWNT interphase (Figure 3.4a). Slow cooled dilute PAN/SWNT solutions in quiescent state (Figure 3.3b) led to the formation of hybrid PAN-SWNT *shish-kebab* structures (Figure 3.4b). This is the first observation of *shish-kebab* structures in the PAN polymer system. In addition, quiescent dilute PAN/SWNT solutions subjected to rapid cooling (quenching) (Figure 3.3c) resulted in the formation of PAN/DMF ‘*blobs*’ on the SWNT bundles (Figure 3.4c).

Table 3.1. *Solution processing and crystallization conditions used to grow the various interphase structures of PAN on SWNT.*[6]

Solution Batches (→) ***Processing Parameters (↓)***			S-a$_1$	S-a$_2$	S-b	S-c
Concentration of SWNT (mg L^{-1})			250	20	20	20
Concentration of PAN	(mg L^{-1})		250	20	20	20
	(wt%)		25	2	2	2
PAN/SWNT Solution Processing Stages	*(1) Sonication Conditions*		time: 24 h bath temperature range: 55 to 90 °C			
	(2) Post Processing (i.e. Shearing)		4 h stirring at 90 °C		none	none
	(3) Cooling	*Initial (T_o) (°C)*	90	90	~55	~55
		Final (T_f) (°C)	60	60	20	20
		Cooling Rate (°C/min)	**4**	**4**	**2**	**29**
Degree of Undercooling ($\Delta T = T_o - T_f$) (°C)			30	30	70	70

Inherently it is more difficult for helical polymers to turn into planar zigzag conformations. The observation of interfacial crystalline PAN coated on SWNT in this work shows the evidence that PAN (typically with helical conformation) can form both extended-chain (tubular coating) and folded-chain (*kebabs*) crystalline structures nucleated by SWNT, under appropriate crystallization conditions. This is confirmed by WAXD results for these samples (Figures 3.4a$_3$ and 3.4b$_3$). For the uniform tubular coating of PAN around the SWNT bundles (Figure 3.4a$_2$), the WAXD 2θ versus intensity profile shows PAN *(200), (110), (310), (120),* and *(420)* peaks in addition to two broad peaks associated with the carbonaceous species in the SWNT sample (i.e., *(002)* graphite peak, and *(100)* carbon peak at ~26° and ~42°, respectively (Figure 3.4a$_3$). Indexing for PAN was determined assuming an orthorhombic PAN unit cell with lattice parameters of *a = 1.06 nm, b = 0.58 nm, and c = 0.51 nm.*[4-5] It should be noted that for these PAN/SWNT samples with tubular coating the major PAN WAXD peak exhibits a distinct shoulder due to the existence of a *(200)/(110)* doublet, which is indicative of high crystalline perfection. Observations using electron microscopy show that in dilute solutions PAN *kebabs* preferentially form under quiescent and slow cooling (i.e., no shear during cooling) conditions (Figure 3.3b). WAXD 2θ versus intensity curves show PAN *(200)* and *(310)* peaks (Figure 3.4b$_3$). As compared to the tubular coated PAN/SWNT (Figure 3.4a$_3$), for the *kebabs sample, (200)/(110)* appear as one major peak, and this may be due to slightly lower crystalline perfection for the PAN *kebabs*. Details about crystalline peak position, *d*-spacing, indexing for crystal planes and crystal size corresponding to the WAXD spectra in Figure 3.4 are listed in Table 3.2.

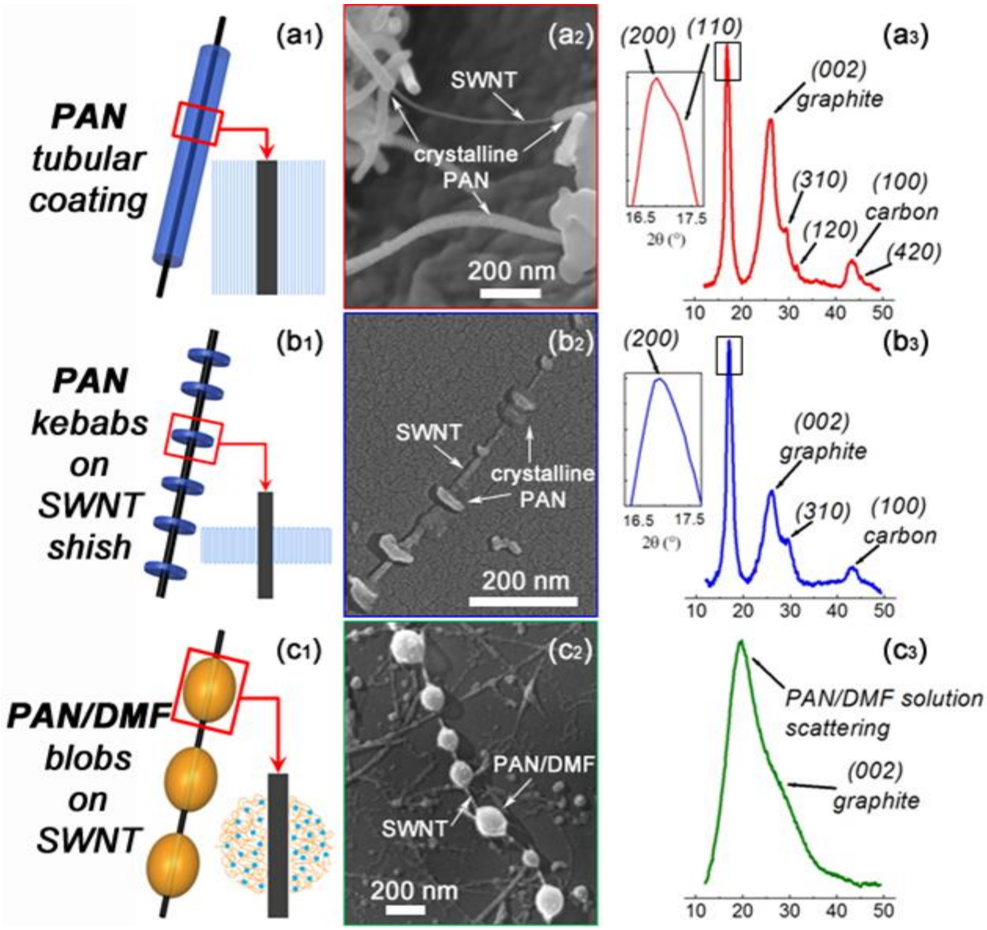

Figure 3.4. *Various PAN Interphase Coating Morphologies on CT SWNT. Schematic (a_1, b_1, c_1), scanning electron micrographs (a_2, b_2, c_2), and wide-angle X-ray diffraction (a_3, b_3, c_3) of PAN tubular coating, PAN kebabs and solvent-rich PAN blobs coating structures on SWNT, respectively.*[6]

Table 3.2. *Wide-angle X-ray PAN (hkl) indexing, d-spacing, and crystal size information for each PAN/SWNT sample. Information for the two carbon peaks observed are also listed.*[6]

		WAXD Crystal Plane						
		(200)	*(110)*	*(310)*	*(120)*	*(420)*	*(002)* (graphite)	*(100)* (carbon)
(S-a) Tubular PAN Coating	2θ (°)	16.7	17.3	29.3	31.7	45.5	26.2	43.2
	d-spacing (nm)	0.531	0.512	0.304	0.282	0.199	0.340	0.209
	crystal size (nm)	7.2	4.5	1.8	9.6	5.2	3.1	3.3
(S-b) Kebab PAN Coating	2θ (°)	16.9	—	29.4	—	—	26.0	42.8
	d-spacing (nm)	0.526	—	0.303	—	—	0.343	0.211
	crystal size (nm)	5.8	—	2.1	—	—	2.7	3.0
(S-c) Irregular PAN Coating	2θ (°)	16.7	—	28	—	—	25.8	42.5
	d-spacing (nm)	0.531	—	0.318	—	—	0.346	0.213
	crystal size (nm)	5.4	—	2.5	—	—	2.9	2.5
As-received SWNT	2θ (°)	—	—	—	—	—	26.2	43.1
	d-spacing (nm)	—	—	—	—	—	0.340	0.210
	crystal size (nm)	—	—	—	—	—	2.9	3.4

The aforementioned procedure was also successfully applied to produce PVA tubular coatings as well. HR-TEM analysis was performed on the tubular coating to verify the presence of extended-chain PAN and PVA, respectively. Figures 3.5a to 3.5d show examples of this microscopy analysis of the PAN/SWNT system, where two PAN coated SWNT bundles were imaged. Based on a comparison of Figures 3.5a and 3.5b, it is clear that before and after electron beam exposure the PAN polymer coating is severely damaged due to irradiation. Lattice images for the PAN polymer is observed at an average spacing of ~0.52 nm (Figures 3.5c and 3.5d) confirming that the tubular coating indeed consists of extended-chain polymer. The uniform tubular coating with an average thickness on the order of ~43 nm was observed on SWNT bundles (~10 nm in diameter). The average coating thickness (based on 60 measurements) of PAN on the SWNT was determine to be ~16.8 nm by SEM and ~5 to 12 nm by TEM. The difference in coating thickness may be due to the presence of metallic coating (see experimental section) on the samples for SEM imaging. Based on the WAXD 2θ versus intensity profile, the crystal size perpendicular to the *(200)* plane (along the PAN chain-axis) is ~7.2 nm, and this is consistent with TEM observations (Figures 3.5c_2 and 3.5d_2). The WAXD results along with the HR-TEM observations suggest that the tubular coating is almost entirely crystalline. Figure 3.5e exhibits the crystalline PVA coating on SWNT bundles and the inset is the magnified image at a specific focal plane to reveal the lattice spacing. It showed the inter-distance (*d*-spacing) is in average of 0.25 nm, which corresponds to the *d*-spacing in *(010)* plane, parallel to the *b*-axis in a PVA crystal unit cell.

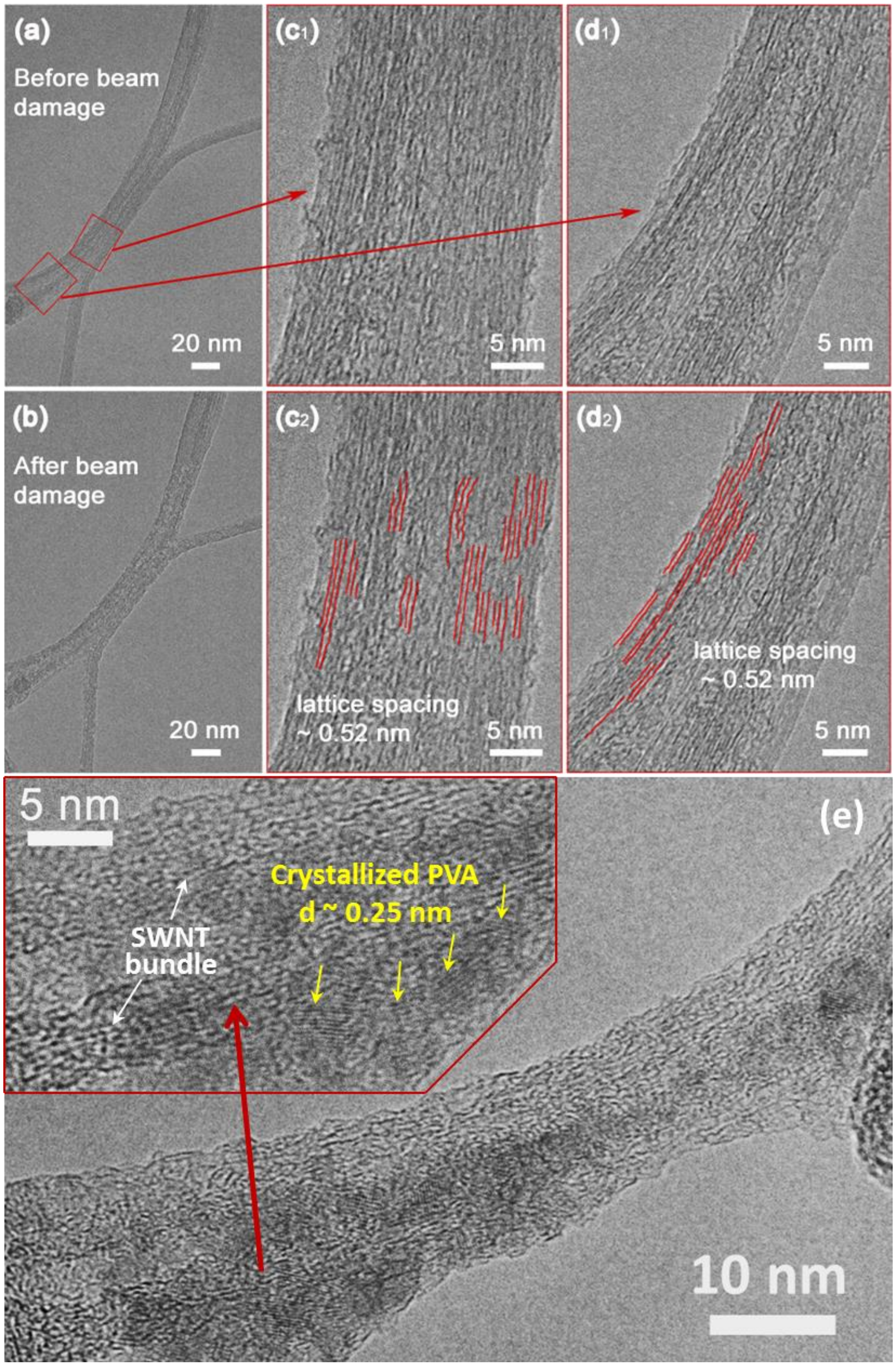

Figure 3.5. *High-resolution transmission electron micrographs of tubular coated PAN/SWNT samples.*[6] *(a) Shows the samples at the onset of electron beam exposure and (b) shows the samples after ~5 minutes of beam exposure. (c_1) and (d_1) show two areas of the PAN/SWNT sample. (c_2) and (d_2) provide the schematic of highlighted lattices of PAN crystalline interphase. (e) HR-TEM image of a PVA-coated SWNT bundle and the inset of a zoomed-in region of the crystalline interfacial PVA coating.*[6]

Conclusions

This work provides insight toward non-chemical SWNT dispersion routes and control of the interfacial morphology formation by means of epitaxial crystallization. Control over the interfacial structure also indicates that the overall structural make-up of the nano-composite is influenced by crystallization processes, where specific interfacial morphology formations in polymer/CNT composites dictate the macroscopic performance. In addition, for the same polymer system, completely different interphase morphologies were induced using slight changes in the crystallization procedures. This work brings to light the ability to control structural registry from the nano- to macro-scale in nano-composites as well as the specificity of the processing conditions for this to occur. The formation of polymer interfacial structure in polymer/nanotube composites is a key factor toward improving stress transfer between the polymer matrix and CNT fillers.

SECTION IV: OBJECTIVE 4

Objective 4: Characterize the processed polymer/nano-carbon fibers in a manner, which will allow correlations between stress, transfer from the nano-inclusion to the polymer matrix as it relates to the interfacial structure.

***Relationship to Objective 1: Understanding the influence of the nano-carbon with polymer interfacial morphology on stress transfer and mechanical properties of the composite material.*

A. PVA/CNC FIBERS (LOW LOADING)

Study 1: Lubrication Effect and Fiber Property

This study investigates the ability of the nano-carbons to influence the polymer morphology in at the interfacial region to form areas of self-reinforcement.

Experimental Section

Materials

As-produced, nano-chips (i.e. flattened FWNT with aspect ratio ~1, consisting of six to eight walls) stack to form nano-fibers. Carbon nano-chip fibers (CNCF) were purchased from Catalytic Materials LLC Inc. (width ~100 nm, average length ~1000 nm, purity > 99 wt%, density ~2.2 $g \cdot cm^{-3}$, and surface area ~120 $m^2 \cdot g^{-1}$). Mowiol 56-98 PVA (M_w ~105,600 $g \cdot mol^{-1}$) was obtained from Kuraray America Inc. Dimethyl sulfoxide (DMSO) was purchased from Fisher Scientific (CAS# 67-68-5, lot# 092053). All the materials were used as-received without further modification.

Preparation of Control PVA and Composite Tapes

The PVA solution was made by dissolving 30.8 g PVA into 200 ml DMSO at ~90 °C. For the composite solution, 6.6 g of PVA was first dissolved into 100 ml DMSO, then 154 mg of CNCF was added into the polymer solution and sonicated (Fisher F530 bath sonicator, 43 kHz, 150 W) for 24 hrs until optically homogeneous dispersions were formed.

Subsequently, 24.2 g of PVA and an additional 100 ml DMSO was added to the PVA/CNCF/DMSO dispersion. The additional PVA was dissolved at ~90 °C, and the entire solution was stirred for 24 hrs to obtain an optically homogenous spinning dope. The overall solid concentration of the CNCF in the dope was 0.5 wt%. Both the control PVA and PVA/CNCF composite tapes were spun using dry-jet wet spinning. The solutions were extruded using a syringe pump (Nexus 6000, manufactured by Chemyx Inc.) through a slit die (0.125 inches by 50 µm) at a rate of 4 $\mathrm{ml \cdot min^{-1}}$. The as-spun tapes passed through a methanol coagulation bath maintained at room temperature (25 °C) and were collected on take-up rollers (rate ~10 $\mathrm{m \cdot min^{-1}}$). The tapes were further soaked in methanol for additional two days before being dried and drawn on rectangular hot plate (10 inches by 1 inch) for five stages from 100 to 180 °C at a step-size of 20 °C.

Characterizations

The fracture surfaces of the control PVA tapes and PVA/CNCF tapes drawn up to 180 °C were observed using a field-emission high-resolution scanning electron microscope (SEM) (Zeiss Surpa 25, accelerating voltage 5 kV). Transmission electron microscopy (TEM) was performed on a JEOL 2010 microscope operated at 200 kV, and the samples were deposited on holey carbon coated 200 mesh copper grid (Electron Microscopy Sciences Lot#110622). Wide-angle and small-angle X-ray diffraction/scattering was performed using a S-MAX 3000 +007 HFM WAXS/SAXS system operated at 1.2 kW with a beam focal size of 70 µm, equipped with a 200 mm multi-wire 2D detector, manufactured by Rigaku Americas. Tensile tests were conducted using dynamic mechanical analyzer (DMA) (RSA-G2 series, manufactured by TA instruments Inc.) with the gauge gap of 20 mm and the extension rate of 0.1 $\mathrm{mm \cdot min^{-1}}$. The number of samples tested ranged from 5-10. Thermal tests were performed using a differential scanning calorimeter (DSC) (Q200, manufactured by TA Instruments Inc). A heating rate of 10 $\mathrm{°C \cdot min^{-1}}$ was used under air flow from ~40 °C to 300 °C. Thermogravimetric analysis (TGA) (Q50, manufactured by TA Instruments Inc.) was also conducted with a heating rate of 20 $\mathrm{°C \cdot min^{-1}}$ under air flow from ~25 °C to 900 °C.

Results and Discussions

The extraordinary structural properties of graphene and carbon nanotube materials motivate the development of practical methods for their use in fabricating continuous, strong, and tough composite fibers. Polyvinyl alcohol (PVA)/carbon nano-chip fiber (CNCF) composite tapes with 0.5 wt% loading show that Young's modulus, tensile strength, and toughness are increased by 585%, 653%, and 20%, respectively as compared to the control (PVA) tapes. Nano-chips exfoliated from the CNCF during processing, lubricate polymer chain alignment and orientation during drawing, where composite tapes could be drawn to higher draw ratios compared to the control tapes. As a result, the Herman's orientation factor (*f*) increased from 0.5 (control tape) to 0.8 (composite tape). Theoretical analysis shows 16 vol.% of the composite tapes consists of fully oriented PVA chains, which contributes to its exceptional mechanical performance.

Morphology and Structure

The fracture surfaces of the control PVA tapes and PVA/CNCF tapes drawn up to 180 °C were observed using SEM and shown in Figure 4.1.1a and 4.1.1b. Figure 4.1.1c shows the SEM image for the as-received CNCF. The CNCF resemble flat wrinkled or kinked fibers, which consists of nano-chips stacked perpendicular to the CNCF axis (Figure 4.1.1d). It is believed that during processing the CNCF are shortened and distorted due to the exfoliation of the nano-chips (flattened nanotubes) from the CNCF (Figure 4.1.1e and Figure 4.1.1g). SEM of the sonicated CNCF (Figure 4.1.1f) shows that they are indeed shorter as compared to the as-received powder. Based on TEM analysis (Figure 4.1.1g) it is observed that the sliding of nano-chips platelets from the CNCF occurs during sonication.

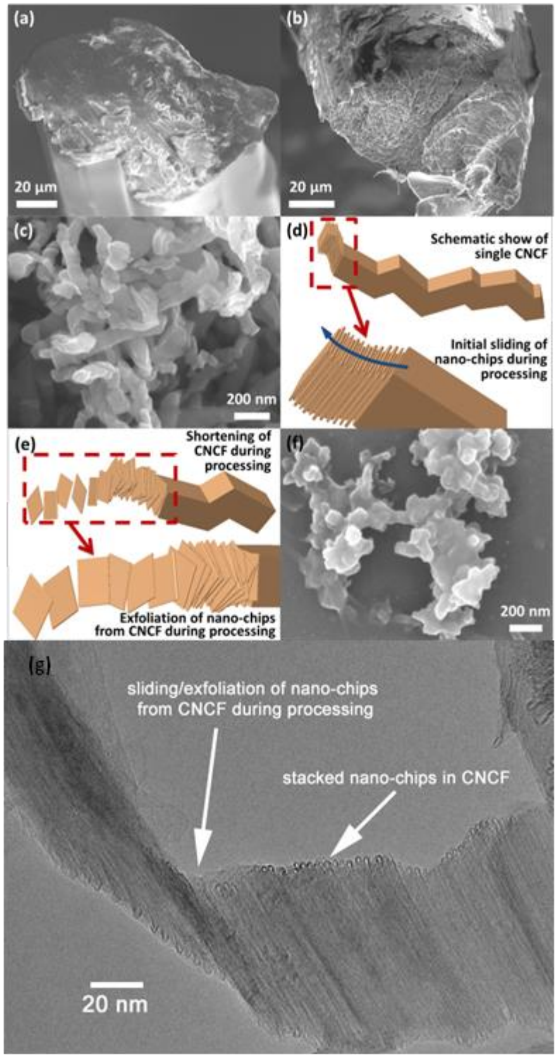

Figure 4.1.1. *SEM images of fracture surfaces for the (a) PVA and (b) PVA/CNCF tapes. (c) SEM of the as-received CNCF powder. Schematics of CNCF showing (d) the stacking of the nano-chips along the CNCF axis, and (e) the sliding and exfoliation of the nano-chips from the CNCF during processing. (f) SEM of the sonicated PVA/CNCF solution. (g) Transmission electron microscope (TEM) image of sonicated CNCF showing the sliding of the nano-chip platelets from the fiber during processing.*[7]

Wide-angle X-ray diffraction (WAXD) patterns for the PVA and PVA/CNCF tapes are shown in Figure 4.1.2a and 4.1.2b. Based on these diffraction patterns, it is clear that the orientation of the PVA chains along the tape axis is much higher in the composite than for the control. Herman's orientation factor (*f*) was calculated using Wilchinski's approach.[8-9] For both the control and composite tapes, *f* was found to be 0.5 and 0.8, respectively. During spinning, PVA/CNCF tapes could be drawn to a ratio of 10, while PVA fibers could only be drawn to 6 (Table 4.1.1). It is believed that the exfoliated nano-chips act as a lubricating material within the tape to facilitate polymer chain slippage, extension, and orientation.

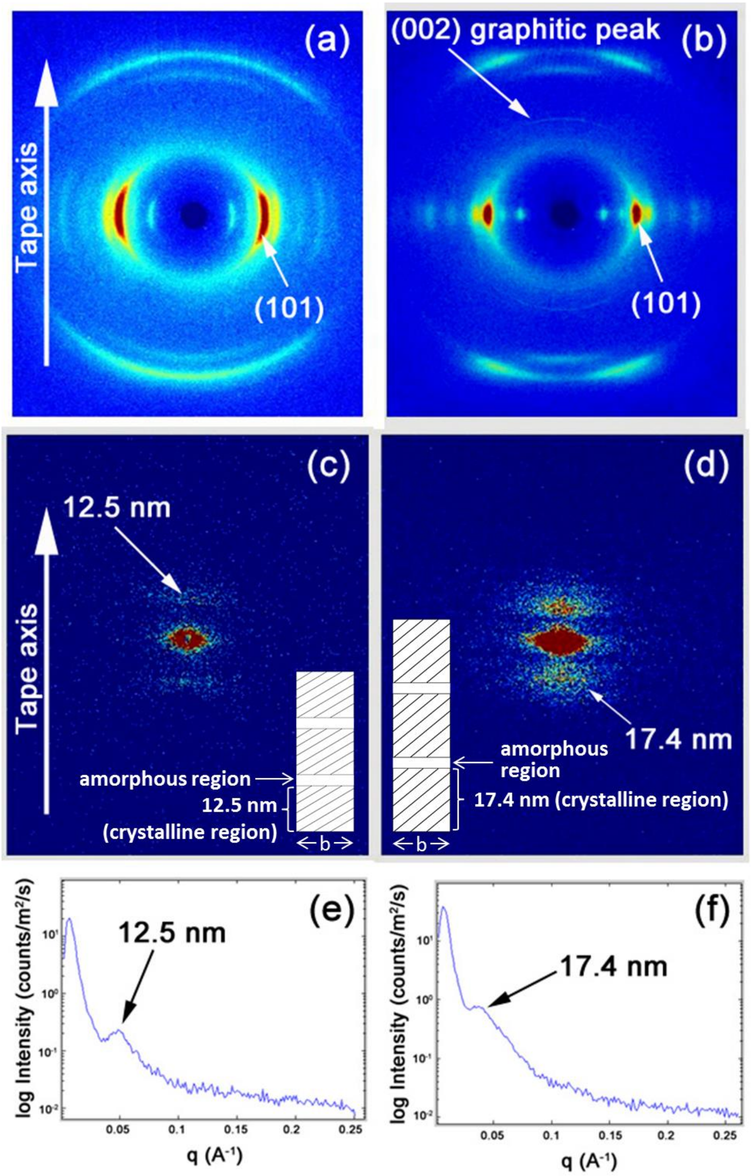

Figure 4.1.2. *WAXD images of (a) PVA, (b) PVA/CNCF tapes. SAXS images of (c) PVA and (d) PVA/CNCF tapes. Intensity versus q, SAXS curves for (e) PVA and (f) PVA/CNCF tapes.*[7]

Table 4.1.1. *Thermal and mechanical properties of PVA and PVA/CNCF tapes.*[7]

Sample	*PVA*	*PVA/CNCF*
ΔH_m, (J·g^{-1})	80.6	80.4
$X_c^{a)}$, (%)	58.2	58.0
$T_m^{b)}$, (°C)	221.8	220.9
$T_g^{c)}$, (°C)	74.9	76.0
$T_d^{d)}$, (°C)	293.8	302.9
Draw ratio	6	10
$E^{e)}$, (GPa)	7.3 ± 1.1	50.0 ± 4.4
$\sigma^{f)}$, (GPa)	0.17 ± 0.03	1.28 ± 0.11
$\varepsilon_{max}^{g)}$, (%)	18.3 ± 2.8	5.3 ± 0.7
Toughness, (J·g^{-1})	16.1 ± 5.0	28.9 ± 7.5

a) Crystallinity degree (X_c) was calculated using ΔH_m (ΔH_c for PVA is 138.6 J·g^{-1} [10]), b) melting temperature, c) glass transition temperature, and d) degradation temperature, e) Young's modulus, f) tensile stress, and g) elongation strain.

Based on small-angle X-ray scattering (SAXS) analysis it was also found that for both tapes a peak is observed along the meridian (Figures 4.1.2c and 4.1.2d). This peak indicates periodic stacks of crystalline lamellae orientated along the tape axis. The long-order spacing was measured to be 12.5 nm for the control tape and 17.4 nm for the composite tape (Figure 4.1.2e and 4.1.2f). In conjunction with higher orientation shown from the WAXD data, the PVA/CNCF tapes clearly display larger periodic stacking of the crystalline lamellae based on SAXS experiments.

Structure-Property Relationship

Overall crystallinity in the materials was measured using DSC and calculated from the enthalpy of melting (ΔH_m) (see Table 4.1.1). The overall crystallinity and melting temperatures are comparable in both composite and control tapes (Table 4.1.1, Figure 4.1.3a). TGA was also performed on the tapes. It was observed that the degradation temperature for the PVA/CNCF composite fiber increased by ~9 °C after the addition of the CNCF (Table 4.1.1, Figure 4.1.3b). This increase may be due to the exfoliation of the nano-chips throughout the polymer matrix, thereby increasing the thermal stability.[11-12]

The mechanical properties for both PVA and PVA/CNCF tapes were measured using a DMA, and these properties are listed in Table 4.1.1. The stress-strain curves are shown in Figure 4.1.3c. Based on these measurements it is found that there is a 585% increase in the modulus and 653% increase in the tensile strength. These results are significantly higher than typical percent increases reported for Young's modulus and tensile strength in polymer-based nano-composite fiber.[13] As mentioned earlier, the CNCF loading is only 0.5 wt%, and based on WAXS data (Figure 4.1.2b) the overall orientation of the nano-chips along the fiber axis is relatively low (i.e. *(002)* peak of the graphitic plane). Therefore, the improvement in modulus and tensile strength is mostly attributed to changes in the polymer morphology as facilitated by the presence of the CNCF.

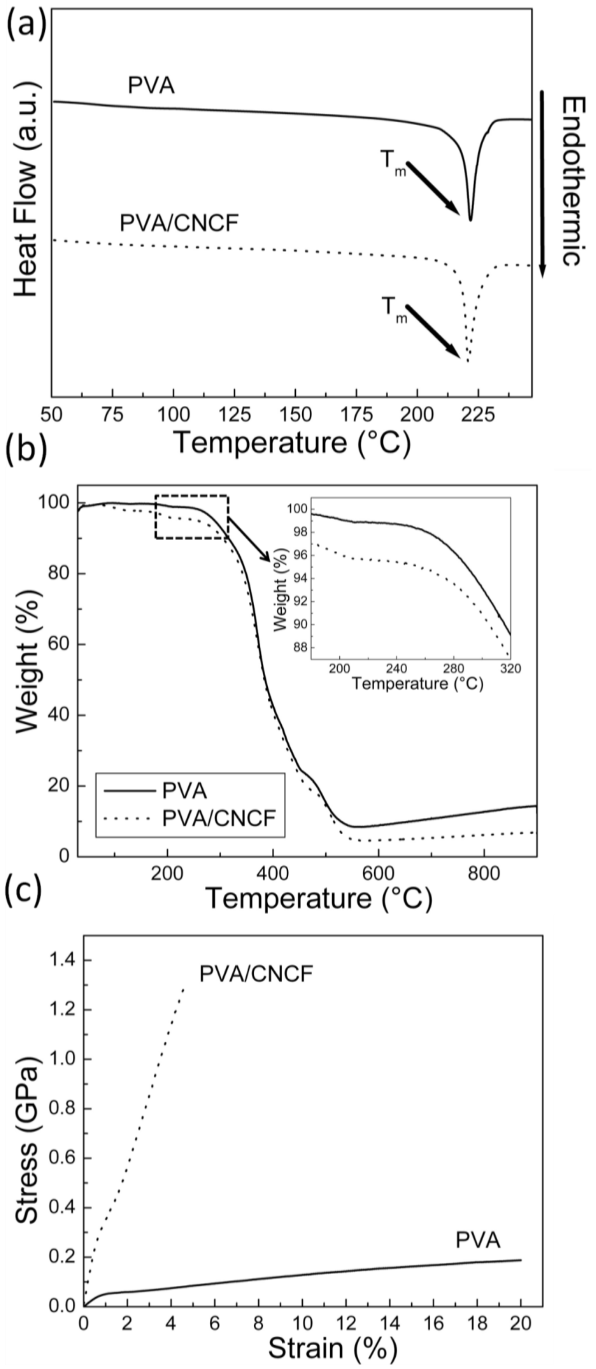

Figure 4.1.3. *(a) DSC of control PVA and PVA/CNCF tapes drawn to 180 °C showing similar melting transition. (b) TGA showing behavior degradation of PVA and PVA/CNCF tapes, and (c) stress-strain curves of the drawn control and composite fibers.*[7]

Based on the rule-of-mixture[14] and the experimental moduli of PVA and various nano-carbon fillers,[15] it is immediately obvious that the modulus contribution of the nano-filler is very low at the volume fraction used, even when the nano-carbon is assumed to be fully oriented along the fiber axis. For this reason, in order to analyze the origin for the large improvement in tensile properties for the PVA versus PVA/CNCF tapes, the rule-of-mixture equation is modified to include a component associated with oriented PVA chains ($V_{m2}E_{m2}$) (Equation 4.1.1). The theoretical modulus used for fully oriented PVA chains in the axial direction is ~255 GPa.[15]

$$E_c = V_f E_f + V_{m1} E_{m1} + V_{m2} E_{m2} \tag{4.1.1}$$

E_{m2}, and V_{m2} are the Young's modulus and the volume fraction of the oriented PVA.

As mentioned earlier, micro-structural analysis of the PVA and PVA/CNCF tapes by SAXS shows the existence of long-order crystalline regions oriented along the tape axis in both materials. The PVA/CNCF tapes show larger crystalline lamellae stacking along the fiber axis which is ~5 nm thicker than the control fibers. The width of the crystal lamellar stack (b) is also determined from the full-width at half maximum (FWHM) for the peak using the Scherrer equation (Equation 4.1.2).[16]

$$b = \frac{\lambda}{\Delta(2\theta)_{0.5}} \tag{4.1.2}$$

λ is the wave-length of the X-ray (0.154 nm), $\Delta(2\theta)_{0.5}$ is the width of the diffraction spot at half peak intensity measured parallel to the equator. This width (b) was determined to be ~15.7 nm for both control and composite tapes. Based on this data, it is determined that the micro-structure of the tapes consists of parallel crystalline stacks of the same width with differing thickness, and this is illustrated in the insets of Figure 4.1.2c and 4.1.2d. Qualitatively it can also be observed from the SAXS patterns (Figure 4.1.2c) that the long-order peak for the control sample shows more diffused scattering as compared to the composite, this may indicate a larger variation of the crystalline stack thickness or the existence of more inter-dispersed amorphous material as compared to the composite. Since the overall orientation for the control tape is much lower than the composite tape (i.e. f = 0.5 (control); f = 0.8 (composite)), these regions of oriented crystalline stacks are assumed to play a large role in the overall increase of the mechanical properties of the tapes.

Orientation of the PVA chains as well as the formation of such large crystalline domains is facilitated by the sliding processes and exfoliation of the nano-chips from the CNCF. The nano-chips lubricate PVA chain slippage and facilitate alignment in the fibers, leading to large well-formed crystalline domains. The presence of these aligned regions greatly contributes to the improvement of the mechanical properties of the composite tape. Based on Equation 4.1.1, it is found that to achieve the experimental composite modulus of 50 GPa the volume percentage of oriented crystalline PVA regions in the fiber is ~16%.

Conclusions

This work brings to light the ability of these unique nano-fillers act as a lubricant to facilitate polymer chain extension. As such, stiffness and strength increase in the composite material are due to the inherent properties of the polymer that occur because of morphological changes. The fractional addition of the nano-filler is also able to improve the thermal stability of the composite. This provides a novel route for producing high-performance composite materials from flexible polymers by only utilizing a small amount of these carbon nano-filler, thereby having a negligible effect on the cost of the composite.

Study 2: Various Loadings and Fiber Property

This study is focused on understanding what level of filler loading (below 1 wt%) is most effective for the development of interphase structures for self-reinforcement.

Experimental Section

Materials

As-produced, carbon nano-chips (CNC) (i.e., flattened FWNT with similar length and width ~100 nm (average aspect ratio ~1), consisting of six to eight walls, and purity >99 wt%) stack to form fibers. CNC were purchased from Catalytic Materials LLC (the stacked fibers have width 100 nm and average length ranging from 1000 to 10,000 nm, density ~2.2 $g \cdot cm^{-3}$, and surface area ~120 $m^2 \cdot g^{-1}$). Mowiol 56-98 PVA (M_w ~105,600 $g \cdot mol^{-1}$, degree of hydrolysis 98.4 ± 0.4 mol%, residual acetyl content 1.5 ± 0.4 wt%) was obtained from Kuraray America Inc. Dimethyl sulfoxide (DMSO) was purchased from Sigma-Aldrich Corporation (CAS# 67-68-5, lot# 472301). Methanol was purchased from Fisher Scientific (CAS# 67-56-1, lot# A43420). All the materials were used without further modification.

Fabrication Method

The control PVA spinning dope was made by dissolving 2.4 g of PVA in 30 ml of DMSO at ~100 °C. For the composite solutions first, 1.8 g of PVA was dissolved into 40 ml of DMSO, and used as a sonication medium for 0.6 g of CNC (Fisher F530 bath sonicator, 43 kHz, 150 W) for another 24 hrs. To remove large aggregates, the dispersed mixtures were centrifuged (Thermo Scientific Sorvall Legend Micro 21 micro-centrifuge, rate up to 15 kRPM) at a rate of 14 kRPM in a time range of 20 to 120 min. To obtain the final spinning dopes additional PVA and DMSO were added to the supernatant of the centrifuged PVA/CNC/DMSO dispersions. The final solid PVA concentration in the dopes was 8 wt%. The final solid concentration of CNC to PVA was 0.125, 0.25, 0.5, and 1 wt% in the composite solutions.

A flow-assisted gel-spinning apparatus was used to spin both the control and the composite fibers. A reservoir was used to supply and recycle the coagulant solvent of methanol, which was also pumped through a glass tube (inner diameter 3 mm and length 3 m) to create a laminar flow field for fiber spinning. The coagulant was maintained at room temperature (25 °C) during spinning. A syringe pump (Nexus 6000, manufactured by Chemyx) was used to control the injection rate for the dope (~0.5 $ml \cdot min^{-1}$). The fibers were extruded through a blunt tip needle (22-gauge with inner diameter 0.413 mm). The as-spun fibers were then collected on a take-up roller at a rate of ~20.5 $m \cdot min^{-1}$.

As-spun fibers were subsequently post-processed by hot-drawing procedures. The drawing procedure was conducted on rectangular hot plate (10 inches by 1 inch) at three stages corresponding to 100 °C (Stage-I), 160 °C (Stage-II), and 200 °C (Stage-III). To avoid oxidation and degradation, roller speeds greater than 5 $\text{m}\cdot\text{min}^{-1}$ were used. Considering the effect of moisture absorption on PVA-based materials, all fibers were kept in a desiccator before characterization.

Sample Characterization

Tensile tests were conducted using a dynamic mechanical analyzer (RSA-G2 series, manufactured by TA Instruments) with a gauge gap of 20 cm and extension rate of 0.05 $\text{mm}\cdot\text{min}^{-1}$. 15 fibers were tested for each fiber batch. Average diameter (d) of the fibers was calculated using the weight method (Equation 4.2.1). Samples consisting of 60 filaments at 5 cm length (l) were weighed to get the mass (m) of the material. The density (ρ) of all samples were determined using the crystallinity (ρ_c) and amorphous (ρ_a) PVA density of 1.345 and 1.269 $\text{g}\cdot\text{cm}^{-3}$ and also the CNC density of 2.2 $\text{g}\cdot\text{cm}^{-3}$ respectively [17]. Fiber crystallinity was measured by Wide-angle X-ray. The average ρ for the fibers was ~1.31 $\text{g}\cdot\text{cm}^{-3}$.

$$m = \rho \cdot \frac{\pi d^2}{4} \cdot l \tag{4.2.1}$$

Dynamic mechanical tests were also carried out using RSA-G2 in tension mode within the temperature range of –80 °C to 230 °C at a step-size of 3 $°\text{C}\cdot\text{min}^{-1}$. Frequency was fixed to 1 Hz. To ensure that the fibers remained only elastically deformed, the maximum tension was set at 0.2% (0.04 mm displacement for 20 mm gauge length), and tension control was used to ensure that the static force always exceeded the dynamic force by 20%. The storage, (E'), and the loss, (E''), dynamic moduli as well as dampening parameter, ($\tan\delta$), were monitored during this temperature sweep test. Bundles consisting of 30 filaments were used for each test. Three dynamic tests were performed for each sample set.

For differential scanning calorimetry (DSC) measurements, fiber samples were heated from 25 °C to 250 °C at a heating rate of 3 $°\text{C}\cdot\text{min}^{-1}$ in nitrogen (DSC Q200, manufactured by TA Instruments) to make sure the Stage-II and Stage-III fibers were free of moisture influences before any other characterization. Wide-angle X-ray diffraction (WAXD) was performed using a Rigaku RAPID II curved detector X-ray diffraction (XRD) system equipped with a 3 kW sealed tube source (voltage 40 kV and current 30 mA). XRD curve fitting and analysis was performed using software's PDXL 2 (version 2.0.3.0) and 2DP (version 1.0.3.4) to obtain azimuthal integration data as well as peak widths (i.e., full-width at half maximum (FWHM)). Instrumental effects were corrected by subtracting a background scattering curve from the measured data.

Small-angle X-ray scattering (SAXS) were performed using a SMAX3000 system equipped with high-brilliance 007HF source with CuK_α radiation (operation voltage 40 kV and current 30 mA, 147 kW), equipped with a 200 nm multi-wire two-dimensional detector (manufactured by Rigaku Americas Corp.). The spot size of the primary X-ray beam at the sample position is approximately 0.2 mm in diameter. The sample-to-detector distance is 1525 mm. At this distance the effective scattering vector (*q*) range is 0.03 to 0.27 Å^{-1}. SAXS patterns were analyzed using the Rigaku GUI software to obtain *q* versus intensity (*I(q)*) curves. The one-dimensional scattering intensity distribution profiles along the fiber axis were derived from the two-dimensional SAXS patterns.

A field-emission high-resolution scanning electron microscope (SEM) (Zeiss Surpa 25, accelerating voltage 5 kV) was used to image both PVA/CNC/DMSO dispersions and fractured fiber surfaces. All samples were sputtered coated with a thin chromium layer (15-20 nm) using a Gatan high resolution ion beam coater for image analysis.

IR spectra were obtained by using a Thermo Scientific Nicolet iS10 Fourier transform infrared (FT-IR) spectrometer. Spectra of 32 scans were collected with wavenumber resolution of 4 cm^{-1} between 500 and 4000 cm^{-1}. A fiber bundle (50 filaments) was used for FTIR measurements. A background correction was performed for each specimen spectrum. The collected spectra were subjected to constant base-line subtraction and normalized to 1456 cm^{-1} peak[18-19] for further analysis. Nicolet iS10 FTIR spectrometer OMNIC software was used to analyze the obtained data.

Results and Discussions

The effect of filler concentration on understanding processing-structure-property relationships in polymer composites with low nano-carbon (nC) loadings (<1 wt%) have been investigated. The nano-carbons used in this work are layered carbon nano-chips (CNC) that exhibit platelet morphology, where each chip layers have the ability to slide with respect to each other. This sliding effect is able to induce microstructural changes in the polymer matrix in the composite. Analysis of the filled polyvinyl alcohol (PVA) fibers demonstrates that the presence of the nC influences the organization and formation of crystalline and amorphous polymer lamellae stacking in the fibers, leading to variation in grain structure in the composite fibers. An increase in grains per unit volume and higher degree of chain orientation along the fiber axis was observed for composite fibers as compared to the control. The presence of the nC filler also leads to the formation of highly ordered self-reinforcing interphase regions in the composite. The presence of the interphase regions are analyzed by both theoretical and experimental methods. It was found that filler distribution throughout the fibers significantly influences the formation of the interphase regions. For these low-loaded composite fibers the formation of interphase increased with filler concentration up to 0.5 wt%. Each of these structural developments contributes specifically to the property variations (i.e., elastic modulus increased by 222%, tensile strength increased by 186% and toughness by 183%) for the composites in comparison to control PVA fibers. In addition, one-dimensional correlation function analysis from SAXS data showed the development in long-spacing with filler concentration increase, as well as corresponding dimensions increasing in both the crystalline and amorphous regions. This work provides a perspective to understand the mechanism of self-reinforcement in composite fibers by tailoring the polymer microstructures.

Morphology and Structure

The aforementioned polymer chain extension facilitated by nC lubrication resulted in the formation of ordered interphase regions, which is a self-reinforcement mechanism. The ability of the CNC to aid the formation of polymer interphase regions for self-reinforcement is further explored in this work. An optimization study pertaining dispersion of the CNC was used here to improve even distribution of the filler particles within the composite fibers. Dispersion of the CNC is one of the most important factors affecting polymer-filler interactions and morphology development. To this end, PVA/CNC dispersions were centrifuged after sonication to remove the larger particles (i.e., agglomerations). These final dispersions were examined using WAXD to determine the degree of exfoliation of the chip stacks (Figure 4.2.1a and 4.2.1b). Due to the inherent nature of the CNC materials (consisting of stacked flattened few-wall nanotubes), each platelet consists of six to eight graphitic layers. Figures 4.2.1c and 4.2.1d also show SEM of the CNC morphology before and after both sonication and centrifugation processes, where the decrease in chip stack length is obvious. A layer of polymer coating was also observed as the CNC were dispersed in dilute polymer solutions.

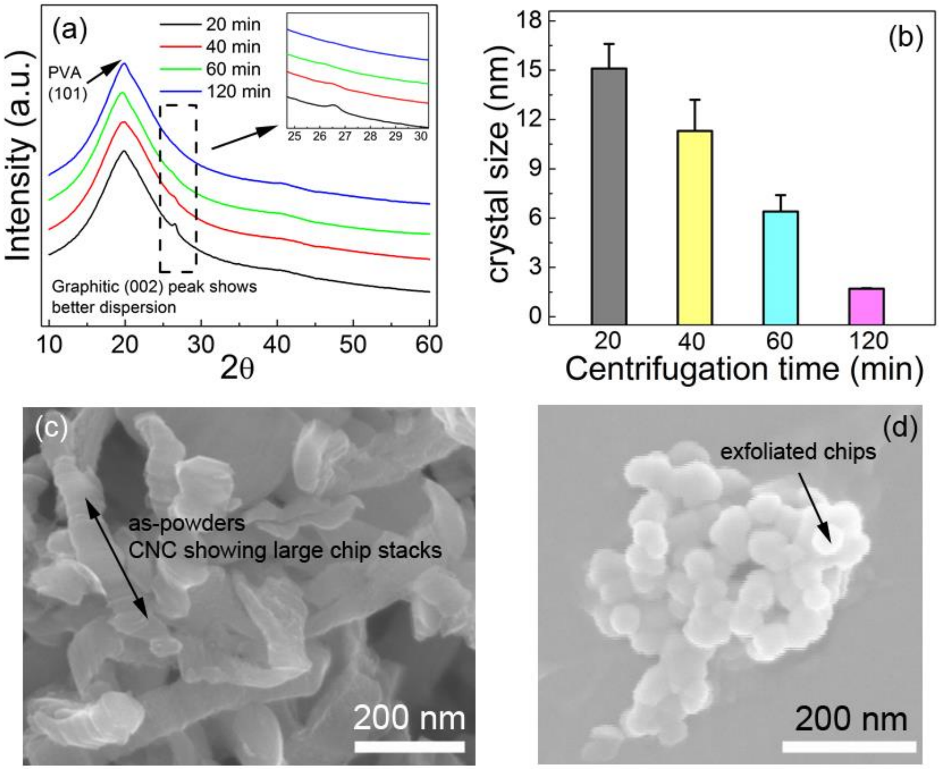

Figure 4.2.1. *Analysis of PVA/CNC dispersion and exfoliation processes using combined sonication and centrifugation by WAXD showing (a) the (002) peak at $2\theta \sim 26°$ diminishing as a function of increasing centrifugation time, and (b) measurements of the graphitic layer thickness (i.e., crystal size) with increasing centrifugation time. SEM images comparing the change in CNC stack length (c) before and (d) after dispersion.*[20]

WAXD results (Figure 4.2.1b) show that CNC treated at 120 minutes are exfoliated to individual chips, while at 60 minutes these fillers consist of an average three to four chip stacks. Therefore, dispersion at 60 minutes centrifugation was used for all composite dope preparations. The use of a dilute polymer solution for dispersion is necessary to induce PVA crystallization at the near interface of nC. This polymer layer also prevents the migration of filler particles into aggregates during solution processing which increases compatibility with the matrix polymer. A flow assisted gel-spinning method is used to fabricate the fibers. To make full use of the lubrication effect, the fibers are extruded into a flowing coagulation bath. This triggers polymer chain alignment at the onset of fiber formation. Baseline studies show that using this flow approach over traditional gel-spinning show improvements in control fiber properties by more than 400% for both modulus and strength, and 200% for toughness[21].

To improve the orientation, post-spinning hot-drawing procedures are used to improve alignment of the polymer chains, increase the degree of crystallinity, as well as amplify crystalline perfection. During the hot-drawing process it is important to increase the drawing temperature and tension force to stretch the fibers. For PVA, alignment of the chains can be prevented or hindered by inter-chain and intra-chain hydrogen bonding.[17] Therefore, drawing is performed in multiple stages at progressively higher temperatures to reduce/interrupt hydrogen bonding and facilitate chain alignment. In this work, a three-stage hot-stage drawing procedure is used, and the draw ratios and fiber diameters are listed in Table 4.2.1. It was observed that that the draw ratio improved from the control to composite fibers with increasing filler loading up to 0.5 wt%. However, a sharp decrease in drawabiltiy is found for the composites with 1 wt% loading, and this is associated with the non-uniformity of the filler distribution as well as the presence of aggregates throughout the fiber.

Table 4.2.1. *Draw ratios (DR) and diameters (d) for as-spun, Stage-I (100 °C), Stage-II (160 °C), and Stage-III (200 °C) drawn fibers.*[20]

Sample (wt%)	**As-spun**	**Hot-stage Drawing Process**						
	$d_{as\text{-}spun}$ **(μm)**	**DR$_{100}$**	d_{100} **(μm)**	**DR$_{160}$**	d_{160} **(μm)**	**DR$_{200}$**	d_{200} **(μm)**	**DR$_{Total}$**
0	*31.1*	6.0	*11.8*	1.4	*10.0*	1.2	*9.8*	**10.1**
0.125	*42.1*	4.2	*19.3*	1.8	*14.4*	1.6	*12.1*	**12.1**
0.25	*36.1*	7.2	*18.1*	1.4	*12.9*	1.4	*9.6*	**14.1**
0.5	*32.2*	6.4	*11.7*	1.4	*9.9*	1.6	*8.5*	**14.3**
1	*46.9*	5.0	*27.2*	1.4	*23.0*	1.4	*15.0*	**9.8**

SEM analysis is used to image the fracture surfaces for all fibers, shown in Figure 4.2.2. It can be clearly seen that all fibers exhibit a fibrillar structure. This type of structure is consistent with what is expected for highly drawn/oriented fibers. The fibrillar structure observed is also consistent with the structural information measured by X-ray scattering analysis in the following discussion.

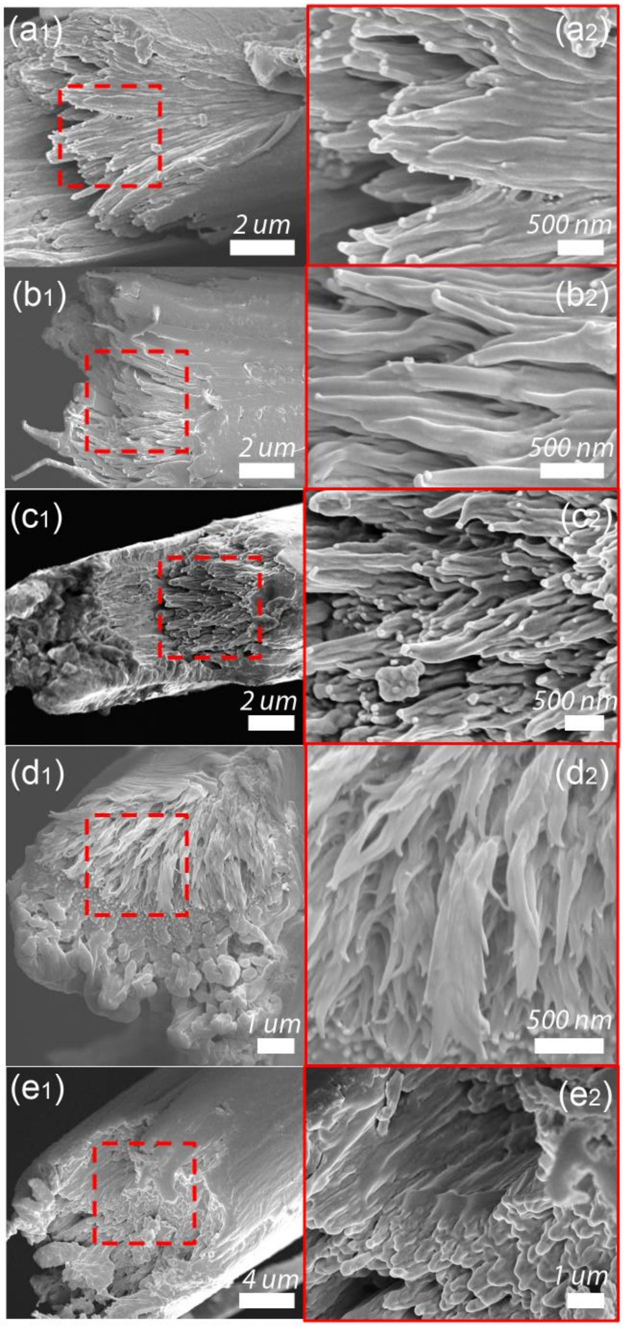

Figure 4.2.2. *Scanning electron micrographs showing the fracture surfaces and fibrillar structure for fully drawn control and composite fibers.*[20]

Figures 4.2.3a to 4.2.3e show the X-ray diffraction pattern of all fibers which exhibit relatively sharp Bragg reflections. These reflections can be indexed with respect to the PVA unit cell.[22] The observation of arcing along the azimuthal direction for the reflections is related to the orientation of the PVA chains along the fiber axis. These reflections narrow as drawing increases and this effect is more pronounced for the composite fibers (Figure 4.2.3). The calculated orientation factor for each sample is listed in Table 4.2.2. At each stage, the orientation factor increases from control to composites.

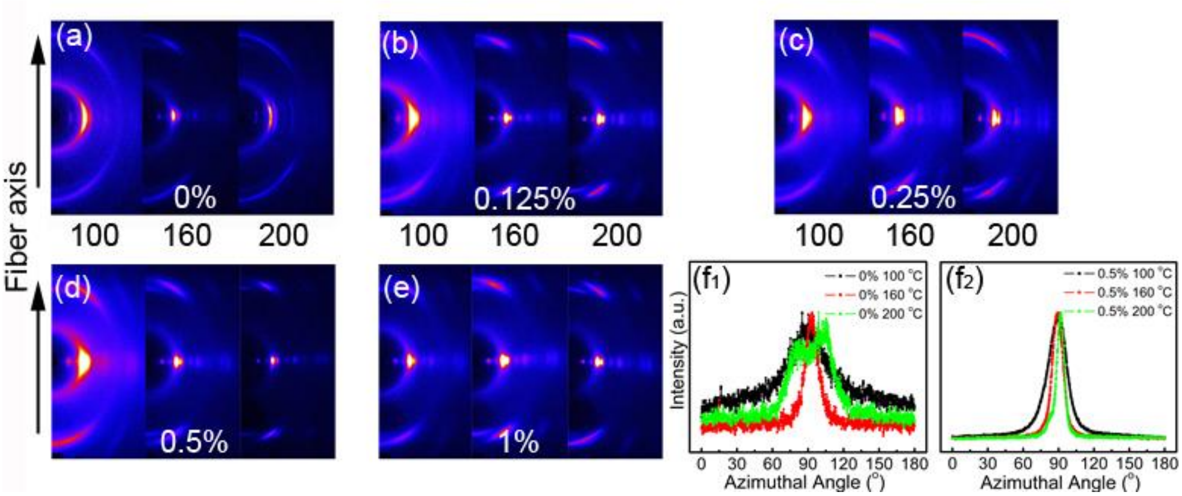

Figure 4.2.3. *(a-e) Wide-angle X-ray diffraction patterns showing the enhancement of polymer orientation as a function of hot drawing stages. Orientation enhancement is also observed with the inclusion of the fillers. Azimuthal curves of the (101) plane reflection for both (f_1) control and (f_2) 0.5 wt% composite fibers at each drawing stage show a narrowing of peak width due to increasing chain orientation.*[20]

Wide-angle X-ray shows that both the polymer crystal size and crystallinity degree are significantly enhanced as hot-drawing proceeds (Table 4.2.3). Crystals perpendicular to the *(101)* and *(111)* show higher values in the composites, especially at Stage-II (160 °C) and Stage-III (200 °C). Control fibers show a decrease in crystallinity from Stage-II to Stage-III, while the composites show an increasing trend. Stage-III drawing occurs nearer to the melting/degradation temperature for PVA.[23] The CNC fillers may provide more thermal stability to the fiber allowing drawability at higher temperatures, while continuing to nucleated PVA crystal growth and seeing an increase of 10% in crystallinity from Stage-II to Stage-III. Comparatively, the control fibers show a decrease in crystallinity (~10%), which may be associated with melting of crystals formed at Stage-II. However, all fibers show that at Stage-III the crystal perfection is increased (both larger crystal size and more crystal planes as shown in Table 4.2.3). This is mostly evidenced by the resolution of the $(10\bar{1})/(101)$ doublet associated with a high degree of chain packing along the fiber axis. The fibers with 1 wt% loadings do not exhibit this feature, and this may be related to the decrease in filler dispersion and/or distribution at higher filler content, which may act to retard crystal growth.

Table 4.2.2. *Orientation calculation parameters and Herman's orientation factor (f) for all fiber samples obtained from WAXD analysis.*[20]

Sample (wt%)	$\langle\cos^2\theta_{(101)}\rangle$	$\langle\cos^2\theta_{(200)}\rangle$	$\langle\cos^2\theta_{(b\text{-}axis)}\rangle$	$^a f_c$
Stage-I 100 °C				
0	0.1479	0.2401	0.6559	0.48
0.125	0.1060	0.2157	0.7014	0.60
0.25	0.1136	0.2110	0.7217	0.58
0.5	0.0777	0.2055	0.7453	0.67
1	0.0769	0.1886	0.7877	0.68
Stage-II 160 °C				
0	0.0751	0.1798	0.7949	0.69
0.125	0.0469	0.1671	0.8229	0.76
0.25	0.0697	0.1714	0.8074	0.71
0.5	0.0538	0.1719	0.8305	0.75
1	0.0571	0.1539	0.8351	0.75
Stage-III 200 °C				
0	0.0951	0.1908	0.7598	0.63
0.125	0.0554	0.1323	0.8489	0.77
0.25	0.0732	0.1505	0.8132	0.72
0.5	0.0568	0.1367	0.8446	0.77
1	0.0560	0.1284	0.8500	0.78

[a] f_c, Herman's orientation factor estimated according to Wilchinsky equation [24].

Table 4.2.3. *Crystallinity and crystal size values for all the fiber samples as a function of drawing stage.*[20]

CNC loadings (wt%)	Crystal Size (nm)					$\chi_{crystallinity}$ (%)
	(100)	$(10\bar{1})$	(101)	(200)	(111)	
Stage-I 100 °C						
0	3.8	−	*4.9*	3.8	*3.6*	50
0.125	3.2	−	*4.7*	2.7	*3.5*	52
0.25	3.5	−	*4.7*	3.7	*4.9*	34
0.5	2.5	−	*4.3*	3.1	*4.6*	48
1	3.6	−	*4.8*	4.1	*3.6*	56
Stage-II 160 °C						
0	4.4	−	*5.7*	2.9	*4.1*	64
0.125	4.1	−	*5.7*	4.2	*6.4*	52
0.25	5.3	−	*5.5*	3.2	*4.6*	44
0.5	4.5	−	*5.9*	4.8	*6.3*	39
1	3.3	−	*5.8*	3.1	*5.7*	48
Stage-III 200 °C						
0	8.6	7.2	*6.2*	7.0	*7.3*	55
0.125	6.2	6.8	*5.2*	5.1	*9.1*	56
0.25	7.4	5.8	*7.5*	5.6	*8.4*	54
0.5	6.6	6.6	*7.6*	6.1	*9.2*	51
1	6.4	−	*7.2*	7.0	*9.0*	60

Figure 4.2.4a shows the representative 2D-SAXS patterns for the fibers at each drawing stage. The two-point lobe pattern is indicative of lamellae structure formations whose

surface are perpendicular to the fiber axis and/or uncorrelated stacking in adjacent fibrils.[25] The equatorial streak originates from the development of fibrillar structures parallel to the fiber axis. This streak becomes sharper with drawing and suggests the formation of well-defined microstructural fibrils with increasing alignment. The SEM analysis shown also confirms this pronounced fibrillar structure in the fibers. The one-dimensional intensity-scattering vector profiles (*I(q)* vs *q* curves) are provided in Figure 4.2.4b. Bar plots in Figure 4.2.4c shows the increasing of the lamellar stack height (L_L) as a function of drawing. The fully drawn composite fibers (200 °C) exhibit a L_L increase up to 16.4 nm as compared to the control fiber of 14.8 nm.

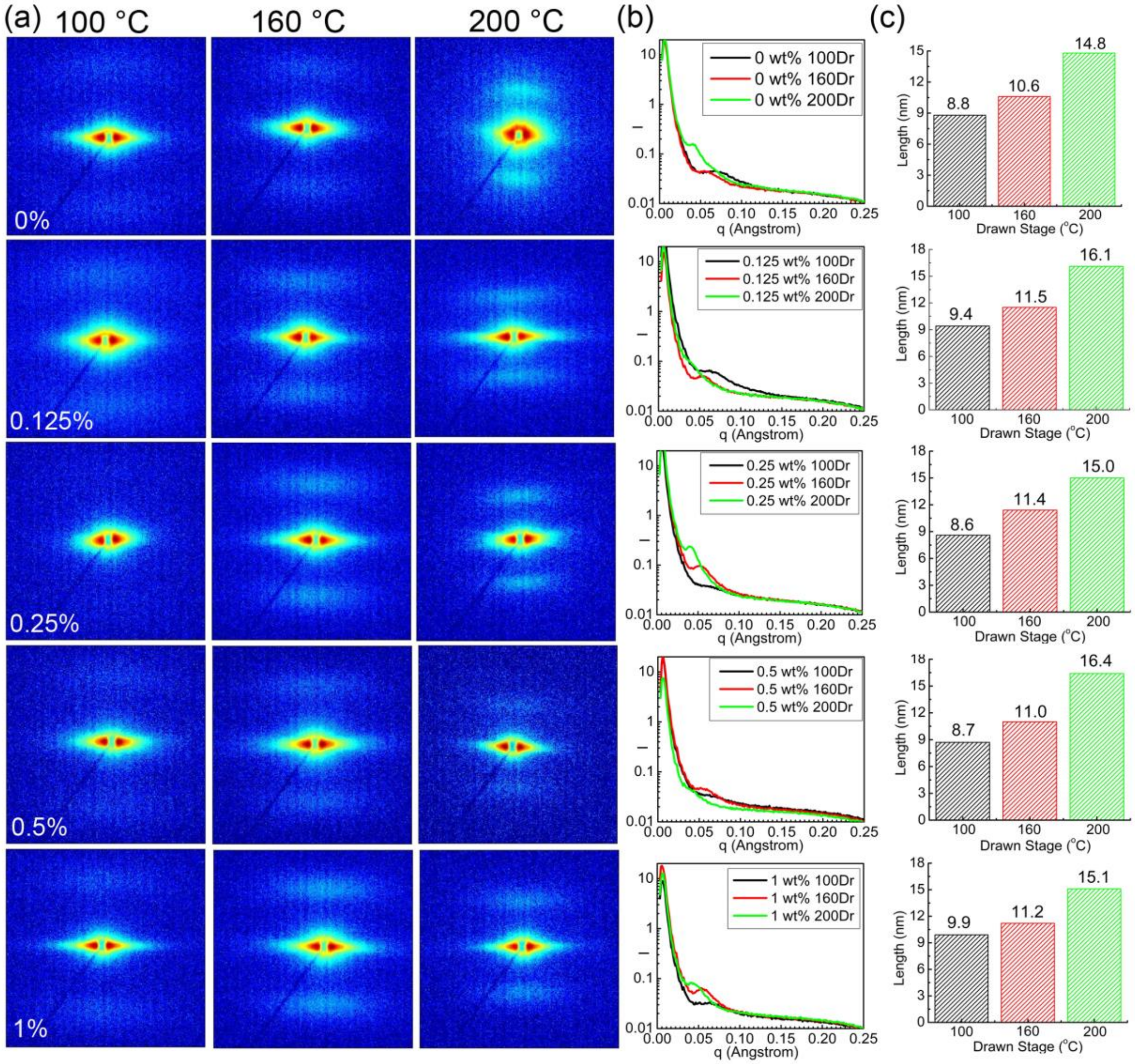

Figure 4.2.4. *(a) Small-angle X-ray scattering patterns shows the development of the long-order lamellar spacing as a function of drawing. (b) Plots for the I(q) vs. q scattering profiles as a function of drawing at various loading samples. (c) Bar plots showing the increase of the lamellar stack height (L_L) as a function of both fiber drawing and the CNC concentrations.*[20]

Structure-Property Relationship

The mechanical properties based on static tensile tests for both PVA and PVA/CNC fibers at drawing Stage-II and III (i.e., 160 and 200 °C) are listed in Table 4.2.4. By examining the property variations for the fibers, an increasing trend is observed for both elastic modulus and tensile strength when comparing the control fibers with the composites up to 0.5 wt% loading. The 1 wt% composite fibers are not consistent with the increasing trend of tensile properties as compared to the other samples. It was also observed that the DMA results for the 1 wt% fibers show a large discrepancy in the storage modulus values (E') as compared to the static tests (Table 4.2.4), and this indicates a lack of uniformity in the overall fiber morphology. One of the major contributions to this issue may be the difficulty of controlling the filler dispersion in the fiber as loading increases. The property improvement of the 1 wt% fibers is much improved when compared to the control samples. However, in comparison to the composite fibers this is not consistently the case. Therefore filler dispersion and/or distribution non-uniformity are expected to play the dominant role in this property trend.

Table 4.2.4. *Listing of the average mechanical properties measured from both static tensile tests and dynamic mechanical analysis for all fibers drawn at stages II and III (160 and 200 °C).*[20]

Sample (wt%)	**[a] E (GPa)**	**[b] σ (GPa)**	**[c] ε (%)**	**Toughness ($J \cdot g^{-1}$)**	**[d] E′ @ -80 °C (GPa)**	**[d] E′ @ 25 °C (GPa)**
Stage-II 160 °C						
0	21.33 ± 4.34	1.00 ± 0.21	8.55 ± 2.26	33.99 ± 9.97	36.79 ± 7.99	12.98 ± 8.45
0.125	33.30 ± 4.63	1.20 ± 0.25	4.85 ± 1.03	29.13 ± 5.66	65.50 ± 1.04	29.05 ± 1.42
0.25	42.65 ± 10.87	1.33 ± 0.23	14.61 ± 4.50	94.36 ± 18.60	66.01 ± 2.18	25.56 ± 1.22
0.5	53.53 ± 4.77	1.73 ± 0.24	5.40 ± 0.77	42.88 ± 6.14	115.00 ± 0.86	53.14 ± 10.14
1	14.53 ± 2.07	0.61 ± 0.04	11.13 ± 7.58	16.27 ± 1.77	42.85 ± 1.43	17.24 ± 0.43
Stage-III 200 °C						
0	27.20 ± 3.48	1.18 ± 0.35	6.88 ± 2.33	40.11 ± 6.10	68.62 ± 7.98	21.21 ± 9.98
0.125	39.51 ± 8.32	1.52 ± 0.24	5.24 ± 0.80	31.40 ± 8.51	86.96 ± 5.85	41.55 ± 3.64
0.25	47.61 ± 7.57	1.42 ± 0.18	5.45 ± 1.20	32.64 ± 5.91	104.59 ± 9.27	40.18 ± 18.96
0.5	60.45 ± 5.95	2.20 ± 0.27	7.46 ± 3.97	73.43 ± 21.28	126.17 ± 7.46	61.43 ± 2.08
1	57.96 ± 4.91	1.61 ± 0.12	4.31 ± 0.20	27.17 ± 2.36	89.91 ± 7.53	37.80 ± 9.28

[a] elastic modulus, [b] tensile strength, and [c] elongation-to-break are measured from static tensile tests; [d] storage modulus based on dynamic mechanical tests.

Since the nC can affect polymer chain arrangement due to interactions between both components,[6, 21, 28] these interfacial interactions lead to the formation of an ordered interphase region. The presence of this interphase region is known to contribute greatly to the mechanical performance of the composite. Initially, the rule-of-mixture equations was modified to include mechanical contributions from the filler, bulk-polymer as well as interphase regions in the composite (Equation 4.2.2).[29]

$$E_c = V_f E_f + V_{m1} E_{m1} + V_{m2} E_{m2} \qquad (4.2.2)$$

E and *V* correspond to the modulus and volume fraction from each region. The subscripts *f*, m_1, and m_2 correspond to the filler, bulk-matrix, and interphase regions, respectively. From original modulus values (Figure 4.2.5a) it is found that the interphase contribution in terms of the volume fraction percentage increases with filler content and is highest at 0.5 wt% (Figures 4.2.5b and 4.2.5c). The modulus value for the interphase region is based on the assumption that the interphase polymer consists of highly ordered (i.e., crystalline and/or constrained state) and perfectly aligned chains.

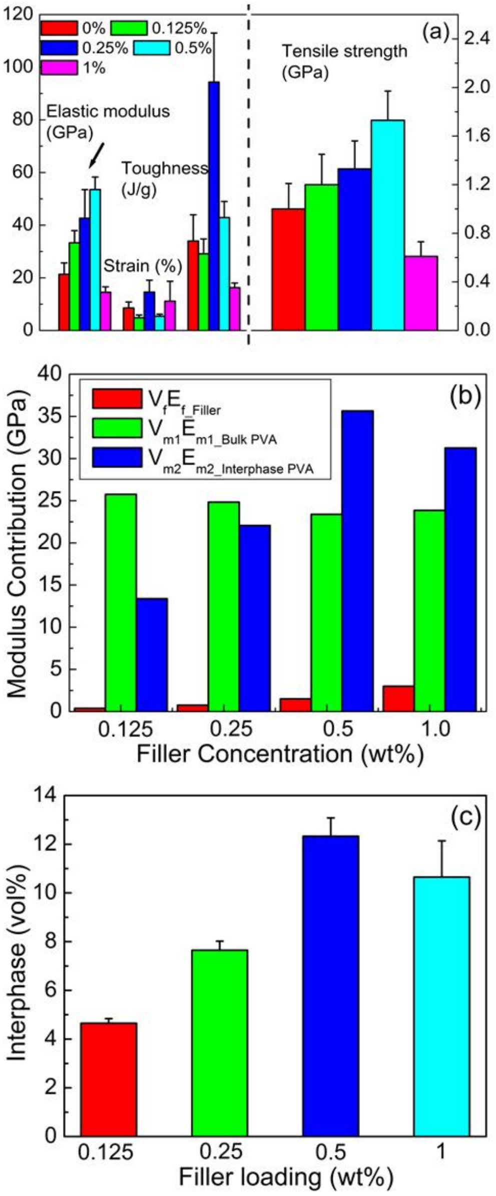

Figure 4.2.5. *Bar plots comparing all fully drawn fibers (Stage-III) show (a) the general mechanical performance (i.e., elastic modulus, tensile strength, tensile strain, toughness) with respect to filler loading, (b) the filler, bulk-polymer, and interphase polymer contributions to the overall composite modulus based on rule-of-mixture analysis, and (c) the predicted theoretical volume fraction percentage of the interphase polymer in the PVA/CNC fibers.*[20]

The DMA of the fibers in this work provides information regarding the viscoelastic properties of the polymer matrix as a function of temperature, specifically for the glass and other secondary transitions associated with chain movement, molecular relaxations, and their relationship to the interactions between the matrix and nano-fillers. Here the confined polymer regions are considered to make up the interphase. Figures 4.2.7a_1 and 4.2.7a_2 show the storage modulus (E′) for both the control and composite fibers with various CNC concentrations. The PVA/CNC fiber with 0.5 wt% loading shows the highest E′ values at Stages II and III. The E′ values are consistent up to 0.5 wt% with the static tensile tests (Table 4.2.4 and Figure 4.2.6). As mentioned, the 1 wt% composite showed the largest discrepancy for room temperature (25 °C) modulus comparing tensile test and dynamic analysis, and this is attributed to the fiber non-uniformity. The static tensile tests use single filaments, while dynamic test requires fiber bundles for analysis. For this reason, the sampling size for the dynamic measurements is much larger (i.e., 200 versus 20 filaments). Therefore the consistency presence/absence between data collected in both measurements does reveal the level of fiber uniformity.

Both loss modulus (E'') and $\tan\delta$ curves show similar transition peaks (Figures 4.2.7b and 4.2.7c), and the values of $\tan\delta$ are listed in Table 4.2.6. For all samples, there are four transition regions associated with molecular motion and subsequent changes in modulus values (i) -25 to 0 °C, (ii) 45 to 60 °C, (iii) 80 to 100 °C, and (iv) above 100 °C. In general, transitions related to region-(i) are related to small molecular motion of side groups or residual solvent molecules, regions-(ii) and (iii) are associated with motion in the amorphous areas of the samples, and region-(iv) corresponds to movement in the crystalline portions of the samples. At temperatures greater than 220 °C no further transitions are identified as the samples enter the flow/melt region.[30] The observed $\tan\delta$ peaks involve cooperative segmental motion of the polymer chain in both amorphous and crystalline regions. Due to polymer-filler interactions, the presence of the rigid bodies will reduce polymer chain mobility by restricting both side-group rotations as well as global back-bone motions. This behavior becomes evident through observance of both upshifts in the transition temperatures and reduction of $\tan\delta$ peak amplitude in the composite samples as compared to the control fibers (Figure 4.2.6 and Table 4.2.5).[30]

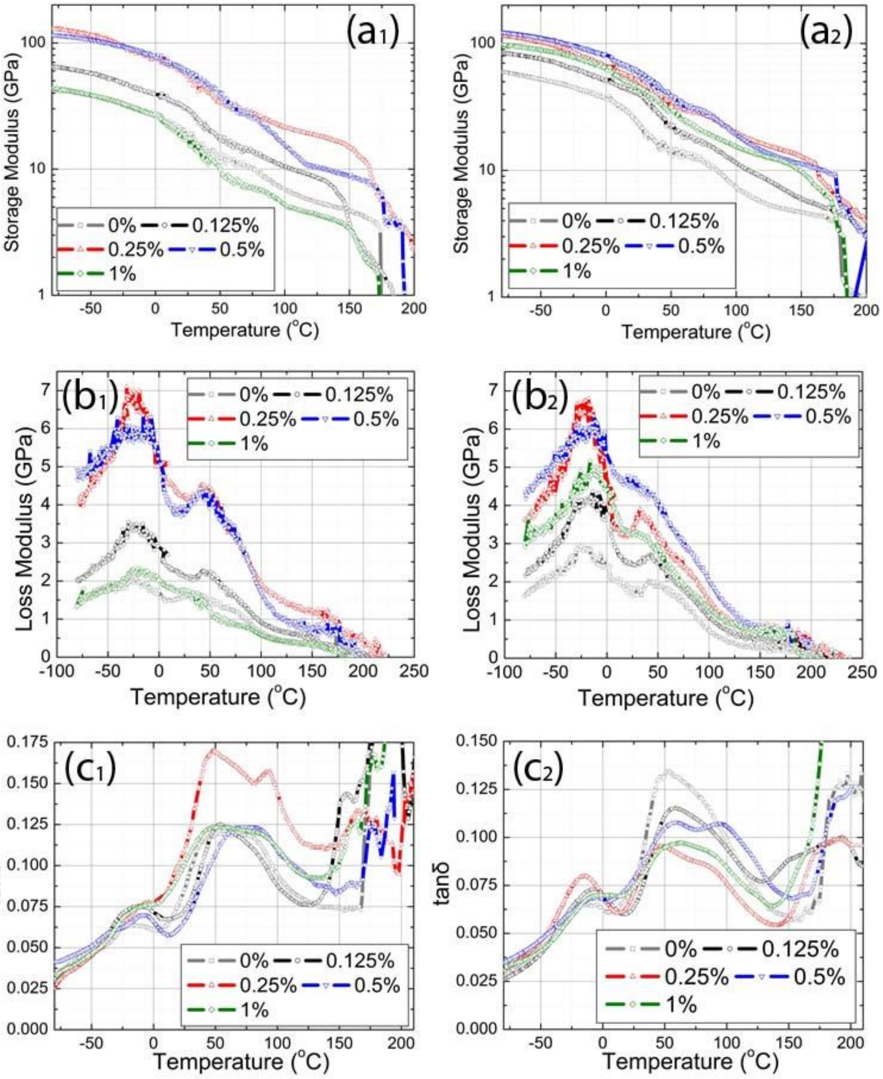

Figure 4.2.6. *DMA of the control and composite PVA/CNC fibers drawn up to Stage-II (160 °C) (a1, b1, and c1) and Stage-III (200 °C) (a2, b2, and c2) showing, (a_1 and a_2) dynamic storage modulus, E', (b_1 and b_2) loss modulus, E'', and (c_1 and c_2) the tangent of mechanical loss angle δ (tan δ) behavior as a function of temperature.*[20]

Table 4.2.5. *List of the transition temperatures and tan δ obtained from dynamic mechanical analysis obtained dampening parameter (tan δ) for all PVA and PVA/CNC fibers drawn at Stage-II and Stage-III.*[20]

Sample (wt%)	**T - β_a * (°C)**	**T - α_{a1} † (°C)**	**T - α_{a2} † (°C)**	**T - α_c ‡ (°C)**	**T - β_c ‡ (°C)**	**T_m (°C)**	***Tan δ***
Stage-II 160 °C							
0	-17.80 ± 5.17	45.29 ± 0.40	81.28 ± 4.00	108.89 ± 10.18	134.17 ± 4.31	172.41 ± 12.14	0.13 ± 0.02
0.125	-9.90 ± 3.09	55.93 ± 5.27	80.31 ± 2.93	155.57 ± 6.38	174.80 ± 3.35	196.74 ± 7.99	0.12 ± 0.01
0.25	-8.73 ± 4.67	53.04 ± 5.59	87.61 ± 5.52	162.57 ± 6.38	176.79 ± 4.48	215.72 ± 6.71	0.17 ± 0.01
0.5	-13.20 ± 6.36	61.71 ± 4.79	85.40 ± 2.55	159.22 ± 0.47	172.80 ± 5.66	196.97 ± 1.22	0.14 ± 0.00
1	-11.64 ± 2.81	45.70 ± 4.06	91.87 ± 1.71	159.37 ± 0.72	172.24 ± 11.73	179.73 ± 8.65	0.12 ± 0.00
Stage-III 200 °C							
0	-23.65 ± 7.22	52.84 ± 7.04	62.51 ± 15.51	160.47 ± 4.70	169.39 ± 3.18	182.50 ± 3.17	0.14 ± 0.02
0.125	-8.73 ± 4.93	58.25 ± 3.30	88.19 ± 2.52	152.33 ± 6.04	182.12 ± 4.54	214.12 ± 9.83	0.11 ± 0.02
0.25	-18.30 ± 5.27	53.17 ± 8.32	89.71 ± 2.49	166.73 ± 6.04	184.04 ± 4.20	217.55 ± 5.15	0.10 ± 0.02
0.5	-12.81 ± 4.44	59.03 ± 4.83	98.09 ± 2.91	167.61 ± 4.95	179.51 ± 5.40	192.42 ± 9.33	0.12 ± 0.01
1	-5.81 ± 3.05	57.71 ± 2.91	81.93 ± 7.64	158.93 ± 2.78	173.45 ± 2.57	182.35 ± 3.63	0.10 ± 0.01

* *β_a transitions refers to small molecules' relaxations (i.e., side groups and/or solvent molecules),* † *α_{a1} and α_{a2} transitions refer to the glass transition regions for either poly(vinyl acetate) or polyvinyl alcohol.* ‡ *α_c and β_c transition temperatures refer to the crystalline region transitions in PVA. All transition temperatures were measured from tan δ curves. T_m means initial melting point for the polymer-based materials extracted at the point of drastic drop of storage modulus. Tan δ values were taken from the glass transition peaks at their maximum to quantitatively evaluate about the interactions between polymer matrix and nano-fillers.*

Conclusions

The results reported in this study indicate that low loadings of nano-filler can cause drastic improvements in the mechanical properties of composite fibers well beyond theoretical predictions. This property increase has a close relationship with the processing techniques used as well as the resultant matrix microstructural features. The precise description of key factors that dominate the nanocomposites reinforcement mechanism requires a thorough understanding of filler dispersion on local scale, polymer chain and/or nano-filler morphology, and interactions between filler and polymer. Here, a facile and reproducible processing strategy allows us to obtain well-dispersed nanocomposites, from which SEM was applied to examine the CNCs dispersion within PVA matrix and showed an even distribution with an interfacial polymer coating. The CNC volume fraction and the composites' mechanical properties have shown an incremental relationship. For the CNC volume fractions lower than 0.5 wt%, the CNC homogeneously disperse within the matrix and initiate the polymer interphase growth confirmed. The interphase volume fraction and their presence have been examined by dynamic and static tensile property analysis. A deeper analysis of the fiber microstructure by scattering has showed more highly aligned polymer chains, perfectly formed fibrillar structures, and longer lamellar spacing in the composites as compared to the control fibers. This study provides a deeper understanding of the role of nanofillers in polymer matrix.

B. POLYMER/SWNT FIBERS (HIGH LOADING)

Study 3: Interphase Formation and Fiber Property

This study shows two key findings. (1) The use of processing modifications to ensure interphase formation in the final composite fiber. (2) The role of the interphase structure toward mechanical enhancement.

Experimental Section

Materials

PVA (molecular weight 325,000 g mol^{-1}, Mowiol 235) was obtained from Kuraray America Incorporation. SWNT (purity > 90 wt%, ash < 1.5 wt%) was obtained from Cheaptubes Incorporation. Dimethyl sulfoxide (DMSO) was purchased from Sigma-Aldrich and used as-received.

Solution Preparation

SWNT was dispersed in DMSO solvent (at a concentration of 21 mg of SWNT mL^{-1} of DMSO) using a bath sonicator (FS30 manufactured by Fisher Scientific) for a period of 48 h. After sonication, the PVA powder and additional DMSO solvent were added into the dispersion to achieve a final PVA concentration of 5 wt% in DMSO and SWNT concentration of 10 wt% with respect to solid content of PVA in the solution. The mixture was subsequently heated and homogenized (T10 ULTRA-TURRAX manufactured by IKA) for 20 h in order to further disperse SWNT and completely dissolve all PVA. Two different solution batches were prepared by using separate heat treatments during homogenization: (i) the first batch of solution (S-A) was homogenized under a constant hot plate temperature of 120 °C; and (ii) the second batch of solution (S-

B) was homogenized using a hot plate temperature 160 °C for the first 2 h and subsequently cooled down to 120 °C. The change in temperature used for the S-B solution induced PVA crystallization during homogenization.

The nanotube dispersions were studied by electron microscopy in order to determine the length distribution of the SWNT after sonication. Diluted droplets of the dispersions were dried on silicon and imaged by scanning electron microscopy. Images were analyzed using the software package Image J (version 1.44o). It was found that after 48 h of bath sonication the SWNT length varied considerably. The average SWNT length distribution based on more than 100 measurements of distinct tubes was 1.5 ± 1.1 μm. This experimental length value is used in conjunction with the theoretical analysis of the mechanical properties for the PVA/SWNT composite fibers produced in this work.

Fiber Fabrication

Rotation of a cylindrical stir-bar in a flat bottom flask (gap size between the cylinder and flask was 10 mm) was used to create shear-flow. The rotation speed of the stir-bar ranged from 50 RPM to 100 RPM. A methanol spinning bath was used and maintained at 5-8 °C for the purpose of gelation. By using a glass syringe (Thermo Scientific HPLC 100 μL), the PVA/SWNT solutions were injected at a speed of 10 $\mu L\ s^{-1}$ through a 22-gauge blunt tip needle into the cold methanol subjected to shear flow. The as-spun fibers were further immersed in cold methanol for 1 h before being drawn on the hot plate. Two hot-drawing stages were used at temperatures of 90 °C and 160 °C, respectively. The drawn fibers were subsequently cut into specimens for tensile tests. The spun fibers from the S-A and S-B solutions are referred to as F-A and F-B fibers, respectively. The specific gel-spinning and hot-drawing parameters used for the F-A and F-B composite fibers are listed in Table 4.3.1.

Table 4.3.1. *Processing parameters for PVA control and PVA/SWNT fibers.*[31]

Fabrication Parameters/ Drawing conditions			**F-A**	**F-B**	**Control Fibers**
Sonication	Time [h]		48	48	--
	Temperature [°C]		50	50	--
Homogenization	Time [h]		20	20	PVA was dissolved by mechanically stirring on 120 °C hot plate
	Hot Plate Temperature [°C]		T_o: 120 T_f: 120	T_o: 160 (first 2h) T_f: 120 (after 2h)	
Shear-Flow Spinning	Needle Gauge/diameter [mm]		22/0.394	22/0.394	22/0.394
	Gelation Temperature [°C]		5 - 8	5 – 8	5 - 8
	Syringe Push Speed [$\mu L\ s^{-1}$]		10	10	10
	Take-up Speed [RPM]		50	50	50
Hot Drawing Process	As-spun Draw Ratio		1.3	1.3	1.3
	Coagulation Time [h]		1	1	1
	Drawing Temperatures [°C]	1st stage	90	90	90
		2nd stage	160	160	160
	Draw Ratio	1st stage	5.0	4.6	9.0
		2nd stage	2.2	2.1	1.7

Sample Characterization

Scanning electron microscopy (SEM) was performed on Supra-25 (operating voltage 5 kV, manufactured by Zeiss). SEM samples were placed on carbon tape and sputter coated with platinum for imaging. Tensile tests were performed using a dynamic mechanical analyzer G2-RSA model (manufactured by TA Instruments) using gauge length of 10 mm and strain rate of 0.05 mm s^{-1}. Wide-angle X-ray diffraction (WAXD) patterns were obtained on multi-filament bundles using Rigaku MicroMax-002 Microfocus X-ray Generator (operating voltage at 45 kV, current at 0.66 mA, CuKα, $\lambda = 0.1541$ nm) manufactured by Rigaku Americas Corporation.

Results and Discussions

Poly(vinyl alcohol) (PVA)/ single-wall carbon nanotubes (SWNT) composite fibers with SWNT loading of 10 wt% were fabricated using a steady shear-flow gel-spinning method. The resultant PVA/SWNT fibers demonstrate excellent tensile strength, modulus, and toughness of 4.9 GPa, 128 GPa, and 202 J g^{-1}, respectively for continuously spun fibers. Templated interfacial crystallization of PVA in the vicinity of SWNT was controlled by tailoring the degree of undercooling of PVA during the composite solution preparation. Wide-angle X-ray diffraction (WAXD) data shows that the templated crystallization behavior of the PVA at the SWNT interfacial region is new. PVA/SWNT fibers which exhibit interfacial structure show a predominant crystallization plane of *(001)* as compared to the *(101)* plane seen in PVA/SWNT fibers which do not exhibit distinct interfacial structure. The new *(001)* crystallization plane is consistent with more adjacent PVA chain locations and shorter hydrogen bonding distance between chains. This demonstrates that the PVA interfacial region around SWNT has denser crystalline chain-packing.

Morphology and Structure

SEM micrographs of the fractured ends of the F-A and F-B composite fibers are shown in Figure 4.3.1. For F-A fibers (Figures 4.3.1a and 4.3.1b), no interfacial coating of PVA is observed around the SWNT bundles on the fractured surface. In contrast, very distinct interfacial crystallization of PVA was observed for F-B fibers (Figure 4.3.1d). The average thickness (*b)* of the interfacial coating is measured and calculated to be ~8.2 nm.

WAXD data for both the F-A and F-B composite fibers is shown in Figure 4.3.2a. Interestingly, compared to the F-A fibers WAXD pattern, the main crystallization plane of the F-B fibers shifted from the most common *(101)* plane at $2\theta = 19.3°$ (i.e. main crystallization plane for the F-A fibers and typically for PVA) to *(001)* plane at $2\theta = 16.7°$ (Figure 4.3.2a). This change of the predominant crystallization plane has never been reported before. The calculated crystal sizes of the predominant crystallization planes for the F-A and F-B fibers are 4.48 nm *(101)* and 8.18 nm *(001)*, respectively. Noticeably, the crystal size on *(001)* plane for F-B fibers is very similar to the average thickness of the interfacial coating (~8.2 nm) measured from the SEM image (Figure 4.3.1d). This indicates that the F-B fibers consists of mostly interphase polymer where the *(001)* crystallization plane is predominant, where the change in crystallization for the interphase PVA is templated by the SWNT.

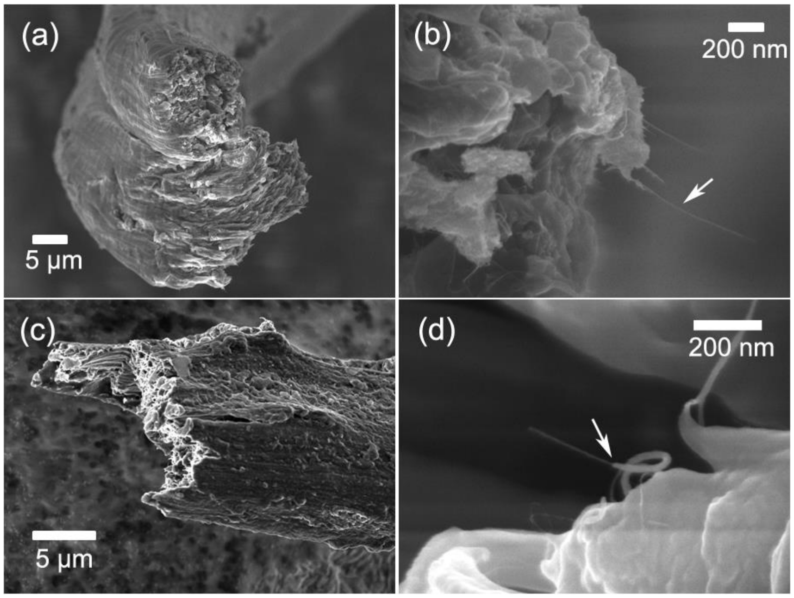

Figure 4.3.1. *Scanning electron microscopy (SEM) images of fiber fracture surfaces for (a) the F-A fiber and (b) high-magnification of F-A fiber showing no evidence of interphase PVA structure around SWNT (see arrow), (c) the F-B fiber and (d) high-magnification of the F-b fiber showing distinct PVA interphase structure around the SWNT (see arrows).*[31]

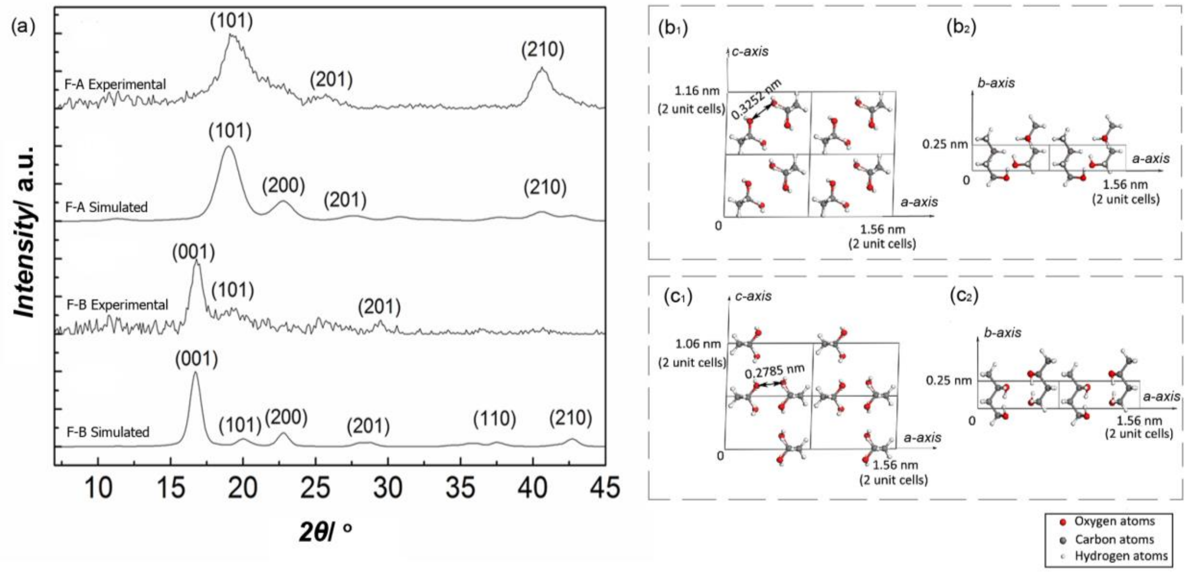

Figure 4.3.2. *(a) Wide-angle X-ray diffraction (WAXD) data for the F-A fibers shows a major crystallization refection for the (101) plane, followed by the simulated WAXD pattern for the proposed PVA unit cell arrangement with major (101) reflection. The experimental WAXD pattern of F-B fibers shows a major crystallization reflection for the (001) plane, followed by the simulated WAXD pattern for the proposed PVA unit cell arrangement with major (001) reflection. Crystal structure comparison of the F-A and F-B fibers: (b_1) unit cell arrangement for the F-A fibers (i.e. Bunn unit cell) in a-c projection, and (b_2) in a-b projection. The closest O-O distance was measured to be 0.3252 nm. (c_1) Unit cell structure for the F-B fibers constructed using the simulated WAXD pattern results in a-c projection (c_2) in a-b projection. The closest O-O distance was measured to be 0.2785 nm.*[31]

Structure-Property Relationship

The mechanical properties of control, F-A and F-B fibers are listed in Table 4.3.2. Compared to the control fibers, the Young's modulus of F-A and F-B fibers shows an increase of 67% and 446%, respectively. Comparatively, the tensile strength of the F-A and F-B fibers also increases by 125% and 308%, respectively. The toughness of the F-A and F-B fibers increases by 82% and 208%, respectively. The highest tensile strength for the F-B fiber (4.9 GPa) is greater than some commercially available polymer high-performance fibers, such as the PVA fibers produced for concrete reinforcement (0.88 GPa) and Kevlar (3.6 GPa). The highest toughness from F-B fibers (202 J g^{-1}) is greater than that of Kevlar (33 J g^{-1}) and spider dragline silk (165 J g^{-1}).[32] Figure 4.3.3a shows the typical strain-stress curves for the control and composite fibers (F-A and F-B). The stress-strain curves show that at the same value of elongation at break (~11%), the F-A fibers show intermediate improvement of mechanical performance as compared to the control fiber. In addition, the F-B fibers with the interfacial crystallization of PVA have even a greater improvement in Young's modulus and tensile strength as compared to the F-A fibers. Figure 2b shows a comparison of the Young's modulus and tensile strength distribution of the control, F-A and F-B fibers versus some of the commercially available fibers as well as various other PVA/SWNT fibers.[26, 33-34] It can be clearly seen that the F-B fibers produce in this work combine both high modulus and high tensile strength, and this is most likely due to the presence of interphase PVA structure which contribute to better stress-transfer between the SWNT and the matrix.

Table 4.3.2. *Mechanical properties of PVA control and PVA/SWNT composite fibers.*[31]

	Control Fibers	**F-A Fibers**	**F-B Fibers**
Effective fiber diameter*) [μm]	22	9.2	9.9
Tensile modulus [GPa]	21.8 ± 3.0	36.3 ± 1.3	119.1 ± 8.6
Elongation-to-break [%]	11.4 ± 1.7	10.7 ± 0.7	9.7 ± 1.1
Tensile Strength [GPa]	1.2 ± 0.3	2.5 ± 0.1	4.4 ± 0.5
Toughness [J g^{-1}]	55.8 ± 12.3	101.4 ± 11.4	171.6 ± 30.4
Effective modulus of SWNT [GPa]	---	201.5[a)] – 1042.1[b)]	1539.8[a)] –8574.4[b)]
Effective modulus of SWNT with polymer interphase contribution	---	---	577.1[a)] –2967.6[b)]
Effective tensile strength of SWNT [GPa]	---	16.9[a)] – 88.1[b)]	47.1[a)]–253.0[b)]

**) Effective fiber diameter D was calculated using the weight method, which is given by* $D = 2\sqrt{w_c / (\rho_c \cdot l_c \cdot \pi)}$

The density of the composite fiber ρ_c *was calculated by* $\rho_c = \rho_{PVA}(1-w) + \rho_{SWNT}w$, *where* ρ_{PVA} *is 1.345 g* cm^{-3} *for fully crystallized PVA,* ρ_{SWNT} *is 2.1 g* cm^{-3} *provided by manufacture and w is the weight concentration of the SWNT in the composite fibers. The weight* w_c *and length* l_c *are the composite fibers.*

a) Calculated value under SWNT aligned (η_o*=1) condition*

b) Calculated value under SWNT randomly oriented (η_o*=1/5) condition*

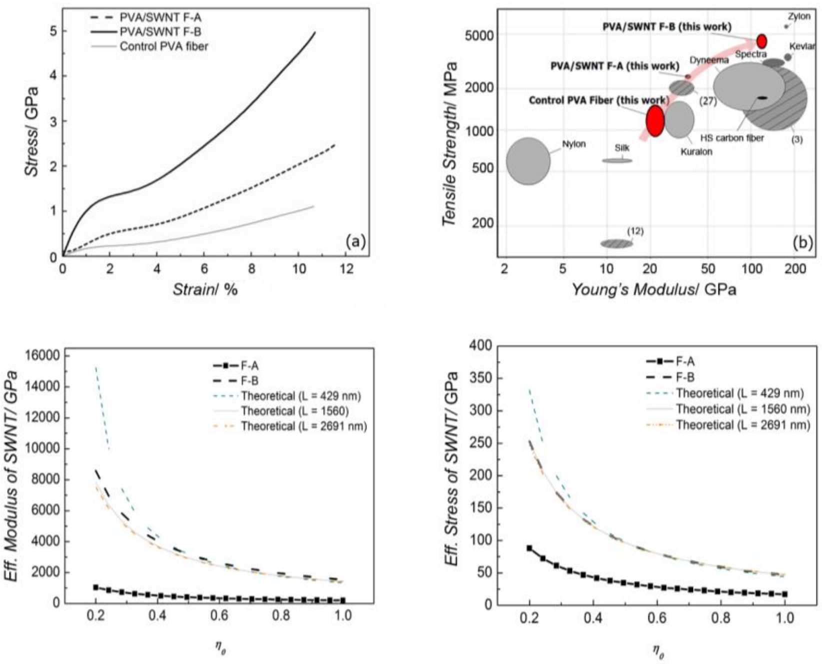

Figure 4.3.3. *(a) Stress-strain curve for PVA/SWNT control and composite fibers. Compared to the control fiber, F-A fiber (no interphase) shows intermediate improvement on both modulus and tensile strength. F-B (interphase present) shows the most mechanical improvement with tensile strength of 4.9 GPa. (b) Comparison of Young's modulus and tensile strength distributions of the control, F-A and F-B fibers in this work versus the same properties of other commercially available high-performance fibers and various PVA/SWNT composite fibers ((i) Vigolo et al., > 60 wt% of SWNT; (ii) Xu et al., 0.3 wt% of SWNT (iii) Young et al., V_{SWNT}: 2 – 31%).*[26, 33-34] *(c) Effective Young's modulus and (d) tensile strength of SWNT for both F-A and F-B fibers as a function of the orientation factor (η_o). Both effective Young's modulus and tensile strength of SWNT gradually approach real values of SWNT as (η_o) increases from 1/5 (randomly distributed) to 1 (perfectly aligned). The SWNT length (L) variation has been taken into account when generating the theoretical curves.*[31]

The SWNT enhancement efficiency was studied by calculating the effective Young's modulus and tensile strength of the SWNT based on the mechanical properties of control, F-A, and F-B fibers. The composite Young's modulus and tensile strength are given by Equations 4.3.1 and 4.3.2, respectively.[35]

$$Y_c = (\eta_0 \eta_1 Y_{SWNT-eff} - Y_{PVA}) V_{SWNT} + Y_{PVA} \tag{4.3.1}$$

$$\sigma_c = (\eta_0 \eta_1 \sigma_{SWNT-eff} - \sigma_{PVA}) V_{SWNT} + \sigma_{PVA} \tag{4.3.2}$$

V_{SWNT} is the volume fraction of SWNT in the composite fiber. $Y_{SWNT\text{-}eff}$, Y_{PVA} and Y_c are the effective Young's modulus of the SWNT, control PVA and composite fiber, respectively. $\sigma_{SWNT\text{-}eff}$, σ_{PVA} and σ_c are the effective tensile strength of SWNT, control PVA and composite fibers, respectively. η_o is the orientation factor which has values of η_o=1 for perfectly aligned fibers and η_o=1/5 for randomly oriented fibers. η_1 is the length efficiency factor described by Equation 4.3.3:[31]

$$\eta_1 = 1 - \frac{Tanh(a \cdot l_{SWNT} / D_{SWNT})}{a \cdot l_{SWNT} / D_{SWNT}} \tag{4.3.3}$$

a is given by Equations 4.3.4 and 4.3.5, respectively:

for Young's modulus calculation:

$$a = \sqrt{\frac{-3Y_{PVA}}{2Y_{SWNT-eff} \ln V_{SWNT}}} \tag{4.3.4}$$

for tensile strength calculation:

$$a = \sqrt{\frac{-3\sigma_{PVA}}{2\sigma_{SWNT-eff} \ln V_{SWNT}}} \tag{4.3.5}$$

D_{SWNT} is taken as the bundle diameter of the SWNT measured from SEM analysis of the fractured composite (10.3 ± 4.4 nm) and l_{SWNT} is the average length of the SWNT after 48 h of sonication and determined to be 1.5 ± 1.1 μm. The average (~1.5 μm) as well as the upper (~2.6 μm) and lower (~0.4 μm) nanotube length distributions are taken into account when determining the effective modulus and strength of the CNT in the composites. The calculated curves for effective $Y_{SWNT\text{-}eff}$ and $\sigma_{SWNT\text{-}eff}$ as a function of η_o are shown in Figures 4.3.2c and 4.3.2d. The theoretical curves are given by calculating Y_c and σ_c values using η_o=1, $Y_{SWNT\ (Experimental)}$ = 1470 GPa, and $\sigma_{SWNT(Experimental)}$ = 52 GPa[36] (experimental values of SWNT bundles) conditions first, and subsequently using Y_c and σ_c values as constants in Equations (2) and (3) to compute the relationship between η_o and $Y_{SWNT\text{-}eff}$ or $\sigma_{SWNT\text{-}eff}$.

According to the calculation, the effective $Y_{SWNT\text{-}eff}$ for the F-B fibers ranges from 1539.8 GPa (η_o = 1) to 8574.4 GPa (η_o = 1/5) and the effective $\sigma_{SWNT\text{-}eff}$ for the F-B fibers range from 47.1 GPa (η_o = 1) to 253.0 GPa (η_o = 1/5). These results suggests that as the orientation factor changes from 1/5 to 1, the calculated values approach the real properties of SWNT (as mentioned), which have been experimentally and theoretically determined.[36-40] Since the fibers are spun under shear-flow and subsequently drawn, the SWNT in the fiber systems will tend to be more aligned than randomly distributed. Therefore, recognizing that a certain degree of disorientation of SWNT will remain in the composite fiber, the minimum effective Young's modulus and tensile strength of the SWNT for F-B fibers are 1539.8 GPa and 47.1 GPa, respectively. By comparing these values with the same analysis for the F-A fibers, the effective $Y_{SWNT\text{-}eff}$ and $\sigma_{SWNT\text{-}eff}$ values of F-B fibers are 664% higher and 179% higher, respectively. This result confirms that by inducing interfacial crystallization of PVA during fiber processing, a stronger PVA/SWNT interphase has been created, and subsequently better load transfer from the PVA matrix to SWNT has been achieved.

Based on this theoretical analysis using Equations 4.3.1 to 4.3.5, the predicted effective modulus value at $\eta_o = 1$ for the SWNT in the F-B is rather high. Typically, both experimental and theoretical SWNT modulus values of 1 TPa or greater are associated with individual single-wall nanotubes as opposed to bundles/ropes. In this work the PVA/SWNT fibers contain SWNT bundles of ~10 nm in diameter, and the predicted and measured modulus values reported for SWNT bundles are usually only a few hundred gigapascals (add refs). For the F-A fibers where there is no interphase present, therefore the bulk-PVA matrix is reinforced by the SWNT bundles. The resultant predicted effective modulus for fully aligned SWNT is ~253 GPa, and this value is within the expected range for nanotube bundles. However, for the F-B fibers the microscopy studies (Figure 4.3.1) show that the micro-structure consists of interphase- and bulk-PVA. For this reason, it is important to understand the influence of this interphase structure on the mechanical performance, and how this may influence the reinforcement efficiency of the SWNT in the composite fiber.

To better understand the crystallization and strengthening mechanism of the F-B fibers with *(001)* crystallization plane, the PVA crystal unit cell models for both the F-A and F-B fibers were built (Figures 4.3.2b and 4.3.2c). The lattice parameters (*a, b, c*) for both the F-A and F-B fibers were calculated from the known indexed peaks present in the WAXD data (Table 4.3.3). The F-A fibers with main crystallization plane *(101)* was built based on the typical PVA unit cell proposed by Bunn,[41] which has a monoclinic lattice system with two PVA chains $P2_1/m$ symmetrically located in diagonal positions. However, since Bunn's structure only describes the unit cell with *(101)* crystallization plane, a new unit cell structure is proposed to better describe the F-B fibers with major crystallization plane of *(001)*. In this hypothetical unit cell, each PVA chain was first rotated respect to the CH group center until the plane where carbon backbone lies was parallel to *(001)* plane. Then the two chains were separated along c-axis to reach the final positions, where one chain located at *(001)* plane and the other chain located at the *a-b* plane. Figures 4.3.2b and 4.3.2c show the comparison of the PVA unit cells of both composite fibers in *a-c* projection and *a-b* projection. WAXD pattern simulation was performed using the unit cell structures (Figure 4.3.2a). The simulated patterns for the proposed unit cell structure for the F-B fiber shows a distinct *(001)* peak at $2\theta = 16.7°$ and a shallow *(101)* peak at $2\theta = 18.9°$, which is in agreement with the real WAXD data. *(101)* and *(201)* peaks are slightly shifted in the simulated pattern due to the perfection of the PVA crystal in the model.

Table 4.3.3. *Lattice parameters, crystal sizes and minimum hydrogen bond distances for F-A and F-B fibers with their predominant crystal planes.*[31]

		F-A Fiber (Predominant (101) crystal plane)	**F-B Fiber (Predominant (001) crystal plane)**
Lattice Parameters	a [nm]	0.781	0.781
	b [nm]	0.252	0.252
	c [nm]	0.581	0.530
	β	91°42’	91° 42’
Crystal Size [nm]		4.48	8.18
Hydrogen Bond Distance [nm]		0.3087*)	0.2785*)

***)** *The closest hydrogen bonding distances were measured from the crystal structures of the F-A and F-B fibers. The distance value calibration was done by the simulation software.*

The strengthening mechanism for both the F-A and F-B fiber crystal structures with respect to the predominant planes was studied by examining the O-H···O hydrogen bonding between the two PVA chains. As illustrated in Figure 4.3.4, the O-O distance is composed of the length of the hydroxyl bond (OH group) and the length of the H···O non-bounded potential. It has been shown that the van der Waals radius for O is around 0.14 nm, which means any oxygen atoms that are closer to around 0.28 nm can experience repulsion.[42] More precisely, the strongest O-H···O bonding can be found at O-O distance of 0.273 nm by bond valence calculation. Therefore, a O-O distance reduction from 0.3252 nm in F-A fiber crystal structures on the *(101)* plane, to 0.2785 nm in F-B fiber crystal structures on the *(001)* plane that measured from the models indicates that as the crystallization plane changed from *(101)* to *(001)* the polymer chains become more adjacent to each other and as a result experience stronger inter-chain hydrogen bonding. This strong interaction between polymer chains introduces more chain resistance upon stretching and may also result in the greater mechanical improvement as observed for the F-B fibers.

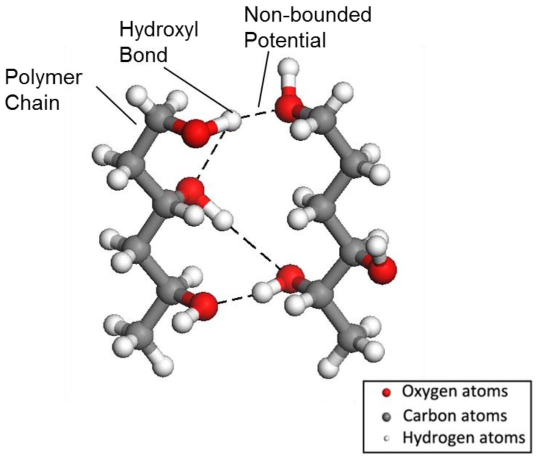

Figure 4.3.4. *Schematic of O-H···O hydrogen bond formation between two polymer molecules. The total hydrogen bond distance is composed of length of the hydroxyl bond and the H···O interaction distance determined by the non-bounded potential.*[31]

A schematic illustrating the PVA chain morphology in the vicinity of SWNT for both the F-A fiber (no interphase) and F-B fiber (interphase present) is shown in Figure 4.3.5. Without the interfacial crystallization presents (Figure 4.3.5a), voids may exists between the matrix interface at the surface of the SWNT. This may be due to the polymer semi-crystalline morphology which consists of both unevenly distributed folded-chain crystals and amorphous chains. The presence of voids will decrease the contact area between PVA chains and SWNT, lower the stress transfer efficiency from polymer matrix to the SWNT dramatically, and result failure due to delamination at the bulk polymer-SWNT interface (Figure 4.3.1b).

On the other hand, when interfacial crystallization is present (Figure 4.3.5b), the interphase regions consisting of the compact PVA crystal structure (based on the WAXD data) provides closer and more complete contacts with SWNT that may allow for more efficient stress transfer. The presence of voids is most likely between the highly crystalline interphase and the semi-crystalline bulk polymer interface. However, the transition from PVA crystalline interphase regions to semi-crystalline PVA regions may be more natural (i.e. PVA chain in both regions can interlock with each other) as compared to the transition from SWNT surface to the polymer chains due to the different energy states of PVA and SWNT. Therefore, the voids for the latter case may be smaller than the former case, and result in fiber failure between the crystalline-interphase and bulk-polymer interface (Figure 4.3.1d).

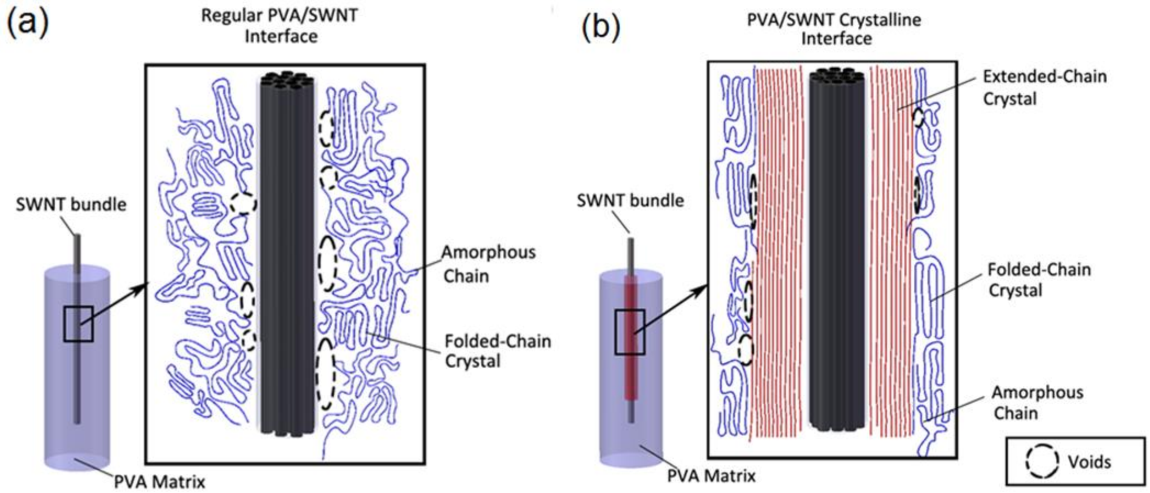

Figure 4.3.5. *Schematic depicting the interfacial structure in a (a) PVA/SWNT fiber displaying no interphase structure (F-A fibers), where voids may be present between the SWNT surface and semi-crystalline polymer matrix; and (b) PVA/SWNT fiber displaying interphase structure (F-B fibers), where void presence is reduced between the SWNT surface and interphase polymer due to PVA crystalline interface.*[31]

Based on the X-ray and SEM evidence, it is clear that in addition to presence of bulk-PVA the interphase-PVA is also predominant throughout the F-B fiber. To determine the effect of this templated polymer structure on the mechanical properties in the composite, additional theoretical analysis for the modulus of the F-B PVA/CNT fiber is performed. The theoretical contribution of the interphase-PVA is determined using Equation 4.3.6.

$$Y_c = V_{PVA} Y_{PVA} + V_{interphase} Y_{interphase} \tag{4.3.6}$$

$V_{interphase}$ is the volume fraction of the PVA interphase in the vicinity of the SWNT. Y_{PVA} and $Y_{interphase}$ are the Young's modulus of the PVA control fibers (i.e. bulk-PVA) and fully crystalline (i.e. interphase-PVA), respectively. The volume fraction of the interphase-PVA is calculated using the crystal size obtained from WAXD and SEM data assuming the each SWNT bundle is uniformly coated by interphase-PVA, and was determined to be ~38.32%. $Y_{interphase}$ was taken to be 255 GPa, and this value is based on experimental X-ray analysis for fully crystalline PVA along the axial direction.[43] X-ray analysis in this work confirms that the interphase-PVA is fully crystalline and oriented in the fiber. To determine the contribution of the interphase-PVA, the SWNT bundle is considered to be a void (Figure 4.3.6a). Therefore, the modulus contribution of the interphase-PVA is calculated to be ~97.7 GPa. Using this calculation, the overall composite modulus is estimated to be ~113.6 GPa. This is below the real composite average modulus of ~119 GPa. For this reason, it is determined that in addition to role of the SWNT as a template for PVA interphase crystallization, the CNT also plays a role in reinforcing the PVA in the composite.

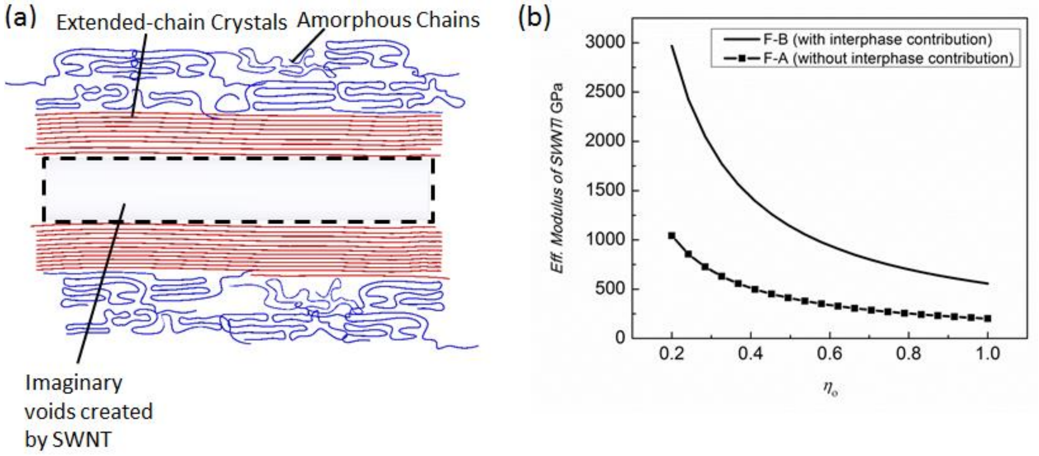

Figure 4.3.6. *(a) Schematic of the effective modulus analysis of the polymer interphase in F-B fibers when considering the location of the SWNT bundle as a void (i.e. only taking the polymer bulk matrix and interphase region into account for the composite formation). Compared to the experimental value (119.1 GPa), the combined effective modulus (102.0 GPa) from both bulk matrix and interphase region suggests that the SWNT in the composite fiber also contribute to the overall modulus. After taking interphase into account, the new effective modulus from SWNT in F-B fibers as a function of orientation factor (η_o) is shown in (b). Compared to F-A fibers, the effective modulus of SWNT is still significantly higher.*[31]

A more accurate prediction of the effective modulus reinforcement of the SWNT bundle in the F-B composite is calculated using Equation 4.3.7:

$$Y_c = (\eta_0 \eta_1 Y_{SWNT-eff\,2} - Y_{PVA} - Y_{interphase}) V_{SWNT} + V_{PVA} Y_{PVA} + V_{interphase} Y_{interphase} \tag{4.3.7}$$

$Y_{SWNT\text{-}eff2}$ is the new effective Young's modulus of the SWNT after taking the interphase-PVA contribution into account. Based on this analysis, the effective modulus for the SWNT ranges from 2293.1 GPa to 434.1 GPa for randomly ($\eta_o = 1/5$) to fully aligned ($\eta_o = 1$) tubes, respectively (Figure 4.3.6b). It should be noted that by including the interphase contribution the approximation for the modulus of the SWNT is more in line with other measured values for SWNT bundles.[44-45] It should also be noted that the effective modulus of the SWNT in the F-B fiber is still significantly higher than what was observed for the F-A fibers (no interphase) (i.e. 434.1 GPa as compared to 201.5 GPa at $\eta_o = 1$).

Figure 4.3.6c shows the effective modulus contributions from each component present in the control, F-A, and F-B fibers. It is clear that the presence of the SWNT templated interphase-PVA significantly affects the fiber properties, and results in an increase of stress transfer from the matrix to the filler. Although experimental analysis for the mechanical contribution from the polymer interphase is currently being pursued to fully examine the PVA/SWNT interfacial strengthening mechanism, the mechanical testing results, crystal structure analysis, theoretical analysis, and morphology visualization all suggest that the formation of a polymer interphase in the vicinity of SWNT plays a very important role in the improvement of the composite fiber mechanical properties.

Conclusions

PVA/SWNT composite fibers with 10 wt% loading were produced with a unique combination of high-performance properties (tensile strength up to 4.9 GPa, modulus of 128 GPa, and toughness of 202 J g^{-1}) by controlling polymer crystallization during gel-spinning under shear-flow. As a result, a new mechanism for PVA crystallization *(001)* crystallization plane is observed of the interphase polymer. A PVA unit cell is proposed for the predominant *(001)* crystallization plane based on both real and simulated WAXD data. The hypothetical unit cell suggests a closer distance and stronger hydrogen bonding between two adjacent PVA chains, which may also contribute to the improvement of the fiber performance. The calculation of the effective Young's modulus, tensile strength is much larger for the PVA/SWNT fibers which exhibit interphase structure. Creation of the polymer interphase region is a key component for improving stress-transfer, where this clearly observed in the F-B fibers as compared to the F-A (no interphase) fibers.

Study 4: The Relationship of CNT Dispersion Quality and Composite Fiber Property

This study uses computational and experimental approaches to show a fundamental relationship between the composite fiber properties and the dispersion/distribution of the CNT filler.

Experimental Section

Materials

PAN-co-MAA (molecular weight 513,000 $g \cdot mol^{-1}$) was obtained from Japan Exlan Company. SWNT (purity > 90 wt%, ash < 1.5 wt%) was obtained from Cheaptubes Inc., N,N-Dimethylacetamide (DMAc) was purchased from Sigma-Aldrich and used as-received.

Solution Preparation

SWNT was dispersed in a pre-dissolved PAN/DMAc solution (25.5 mg of PAN ml^{-1} of DMAc, 1:1 weight ratio of SWNT and PAN) using a bath sonicator (FS30 manufactured by Fisher Scientific) for 48 hours. After sonication, additional PAN powder and DMAc solvent were added into the dispersion to achieve a final PAN concentration of 7 wt% in DMAc and SWNT concentration of 10 wt% with respect to solid content of PAN in the solution. The mixture was subsequently homogenized (T10 ULTRA-TURRAX manufactured by IKA) under a constant solution temperature of 90 °C for the first two hours and subsequently cooled down to 60 °C, and further mixed until the PAN/SWNT dope appeared optically homogeneous for spinning.

Fiber Preparation

A laminar flow in a glass tube was created using a metering pump (Q3, FMI Fluid Metering, Inc.) connected to a cold methanol source (5 to 8 °C). The flow-rate was accurately controlled by adjusting the speed of the metering pump which ranged from 0 to 2000 ml/min. A pump speed of 200 ml/min was used for all spinning processes used in this work. The PAN/SWNT solution was injected at a speed of 0.30 mL/min through a 22-gauge blunt tip needle into the center of the cold methanol flow. The as-spun fibers were collected and further coagulated in methanol for an additional ~12 hours before being hot-drawn. Two hot-drawing stages were used at temperatures of 90 and 160 °C, respectively. The drawn fibers were subsequently cut into specimens for characterization. The fiber spinning parameters are summarized in Table 4.4.1.

Table 4.4.1. *Processing parameters for the spinning and hot-drawing of the PAN control and PAN/SWNT composite fibers using the shear-flow gel-spinning process.*[46]

Fabrication Parameters/ Drawing conditions			*PAN Control Fibers*	*PAN/SWNT Composite Fibers*
Sonication	Time (h)		--	48
	Temperature (°C)		--	50
Homogenization	Time (h)		PAN was dissolved by mechanically stirring on 100 °C hot plate	20
	Hot Plate Temperature (°C)			T_o: 170 (first 2h) T_f: 100 (after 2h)
Shear-Flow Spinning	Needle Gauge/diameter (mm)		22/0.394	22/0.394
	Gelation Temperature (°C)		5 - 8	5 - 8
	Solution Injection Speed (ml/min)		0.30	0.30
	Pump Speed (ml/min)		200	200
	Fiber Take-up Speed (m/min)		1.35	1.35
Hot Drawing Process	As-spun Draw Ratio		2.6	2.6
	Coagulation Time (h)		12	12
	Drawing Temperatures (°C)	1st stage	90	90
		2nd stage	160	160
	Draw Ratio	1st stage	9	7
		2nd stage	4	4

Sample Characterization

Thermogravimetric analysis (TGA) was performed on TGA-Q50 (manufactured by TA Instruments). Scanning electron microscopy (SEM) was performed on Supra-25 (operating voltage 5 kV, manufactured by Zeiss). Tensile tests were performed on a dynamic mechanical analyzer G2-RSA model (manufactured by TA Instruments) using gauge length of 15 mm and strain rate of 0.07 $mm\cdot s^{-1}$. Wide-angle X-ray diffraction (WAXD) patterns were collected on multi-filament bundles using a Rigaku RAPID II (operating voltage at 40 kV, current at 30 mA, CuKα, $\lambda = 0.1541$ nm) equipped with curved detector manufactured by Rigaku Americas Corporation.

Computational Method

Full atomistic MD simulations were performed using the software package LAMMPS (http://lammps.sandia.gov/).[47] The consistent valence force field (CVFF)[48] was used to describe the system potential energy for both polymer and SWNT. While more accurate potentials are available for the modeling of both polymers and carbon-carbon interactions (e.g., ReaxFF,[49] AIREBO,[50-51] or LCBOPII[52]), the CVFF potential is adequate to capture polymer-nanotube interactions under equilibrium conditions via a classical Lennard-Jones interaction. The CVFF potential has also been shown to accurately reflect the conformation of short polymer chains.[53-54] Three polymer chains were used for each simulation case and each consisted of 50 monomers with atactic stereo configurational arrangement. The SWNT samples used in the experimental work had an average diameter of 1-2 nm. For this reason, for simulation studies SWNT with three different diameters 1 nm, 1.5 nm, and 2 nm were built in the model to represent the lower bound, average value, and upper bound of the real tube diameter used. All tubes with different diameters had the same length of 12.3 nm and armchair chirality, or (7, 7), (11, 11) and (15, 15) corresponding to diameters of 1 nm, 1.5 nm, and 2 nm, respectively.

SWNT bundles were constructed by arranging individual adjacent tubes into bundle form. The bundle geometry is optimized by using steepest descent minimization functions with cutoff distance of 0.8 nm for the carbon-carbon Lennard-Jones interaction. Four variations of SWNT bundles are considered in the analysis: a larger bundle of diameter 8.9 nm (consisting of 19 tubes with 1.5 nm tubes) and three small bundles of diameter 3.7 nm (five - 1 nm tubes), 5.2 nm (four - 1.5 nm tubes), and 5.7 nm (four - 2 nm tubes). As the aim of this study is the understanding of the baseline PAN-SWNT energetic interactions, no solvent molecules were used in any simulations. All simulations were performed using the constant volume and temperature canonical ensemble (NVT), with periodic boundary conditions. The equations of motions were integrated using velocity verlet algorithm with an integration time step of 1 fs, and the temperature was controlled by a Nose-Hoover thermostat. All systems were equilibrated at 300 K (using a damping constant of 2.0) for 2 ns to stabilize the interactions, confirmed by energy convergence. For analysis, polymer-SWNT interaction energies were extracted indirectly from the simulation data and CVFF potential, where interaction energy equaled the total system energy subtracted by the energies from SWNT and polymer separately. It should be noted that the reported energy curves were the average values of three runs for each simulation scenario.

Results and Discussions

A combination of computational and experimental methods were implemented to understand and confirm that conformational changes of a polymer (specifically polyacrylonitrile (PAN)) vary with the dispersion quality and confinement between single-wall carbon nanotubes (SWNT) in the composite fibers. A shear-flow gel-spinning approach was utilized to produce PAN-based composite fibers with high concentration (i.e., loading of 10 wt%) of SWNT. SWNT dispersion qualities ranging from low to high were identified in the fibers, and its effects on the structural morphologies and mechanical properties of the composites were examined. These results show that as the SWNT dispersion quality in terms of distribution in the fiber and exfoliation increases, PAN conformations were confined into the extended-chain form. Full atomistic computational results show that the surface interaction energy between isolated PAN and SWNT was not preferred, leading to self-agglomeration of PAN. However, confinement of the polymer chains by between SWNT bundles or individual tubes (i.e., molecular crowding) resulted in large increases in the PAN-SWNT interaction energy. In other words, the crowding of polymer chains by the SWNT at high concentrations can promote extended-chain conformational development during fiber spinning. This was also evidenced experimentally by the observance of significantly improved PAN orientation and crystallization in the composite. Ultimately this works provides fundamental insight toward the specific structural changes capable at the polymer/nanotube interface which are important toward improvement of the effective contribution of the SWNT to the mechanical performance of the composite.

Experimental Analysis

This study illustrates one of the fundamental challenges associated with controlling the processing parameters for polymer/SWNT composites to achieve consistent composite properties. Representative stress-strain curves as well as the Young's modulus and tensile strength pertaining to each of the three fiber sample batches (i.e., F-1, F-2, and F-3) of PAN/SWNT composite fibers are shown in Figure 4.4.1. Despite using the same flow gel-spinning procedure to produce all fibers, due to noticeable changes in the SWNT dispersion quality within the fibers, significant differences with regard to their Young's modulus and tensile strength were observed. An increase in the Young's modulus following the ratio of 1:1.4:2.5, as well as an increase in tensile strength according to the ratio of 1:1.9:3.2 were found respectively for the F-1, F-2, and F-3 composite fibers, which improve with the corresponding increase in SWNT dispersion quality.

It is expected that the variations in PAN/SWNT dispersion occurring during preparation of the spinning dope and subsequent fibers are the result of a combination of *(i)* limited polymer-SWNT interactions, *(ii)* undispersed SWNT (i.e., entanglements and agglomerations), as well as *(iii)* the presence of PAN-rich regions. In order to understand the contribution of the structural features toward the differences in the mechanical performances observed for the composites, a thermal charring treatment was performed to remove PAN domains to visualize the arrangement/distribution of the SWNT in the fibers. Based on TGA analysis, the degradation temperature of the as-received SWNT powder was determined to be ~500 °C in air and > 900 °C in nitrogen, while the degradation temperature of the as-received PAN powder was found to be ~200 °C in air and ~250 °C in nitrogen. For this reason, all fibers were heated in a nitrogen environment from 25 to 900 °C at a rate of 5 °C/min to burn out PAN regions. It is recognized that during the thermal treatment some fiber shrinkage and distortion will occur. However, due to the higher thermal stability of the SWNT under the charring conditions, the PAN/SWNT composites retained its fiber-like form, and in general the original SWNT morphology was preserved.

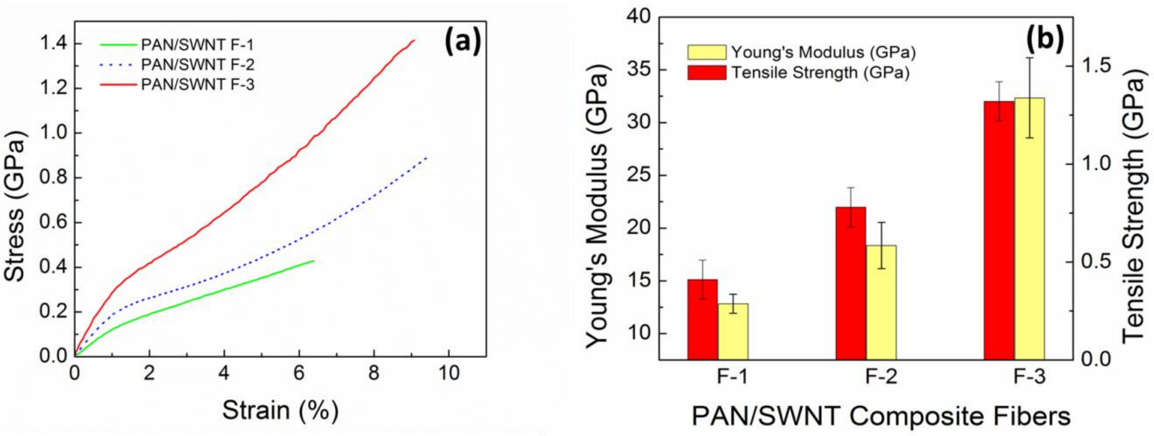

Figure 4.4.1. *(a) Typical stress-strain curves and (b) plot comparing the Young's modulus and tensile strength for all three batches of PAN/SWNT composite fibers produced in this work. Compared to the F-1 composite fibers with the lowest mechanical performance, F-2 exhibits an intermediate improvement, while F-3 shows the highest values for both modulus and strength. These results are consistent with the degree of SWNT dispersion and PAN orientation exhibited by these composite fibers.*[46]

The charred composite fibers were observed by SEM (Figure 4.4.2). After thermal-charring, F-1 fibers (Figure 4.4.2a) exhibited large voids due to the burn-out of PAN-rich regions. This may be indicative of poor interaction between the PAN and SWNT during the dispersion process, resulting in separation of the dope into PAN-rich and SWNT-rich domains. This structure was subsequently translated to the spun F-1 fibers. For F-2 fibers such large voids were not observed as compared to F-1. However, medium sized voids as well as large SWNT aggregations/entanglements (Figure 4.4.2b) were observed. The presence of these SWNT aggregates also suggests poor interaction between PAN and SWNT during dispersion and subsequent fiber formation. As compared to both F-1 and F-2 batches, F-3 fibers (Figure 4.4.2c) exhibited a much more homogenous distribution of the SWNT throughout the composite. There was also no evidence of large void structures arising from polymer-rich regions or SWNT aggregates throughout the fiber. The F-3 morphological features are more consistent with improved PAN-SWNT interaction as compared to F-1 and F-2 fibers.

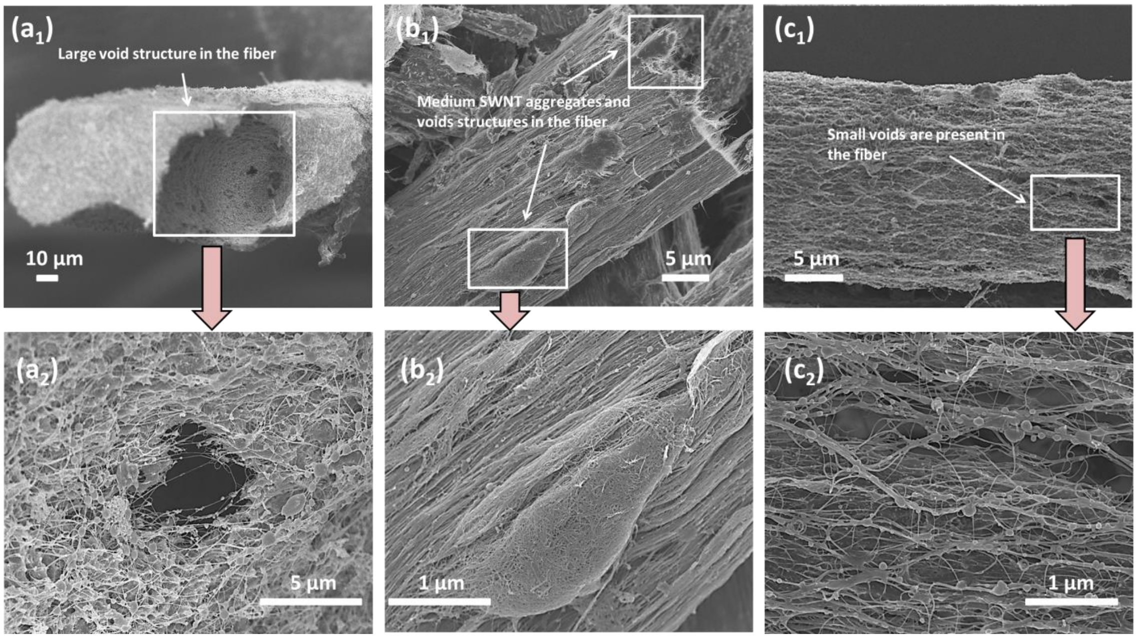

Figure 4.4.2. *Scanning electron microscopy (SEM) images of the PAN/SWNT composites fiber after charring showing the SWNT distributional morphology. (a_1) Cross-section of the F-1 composite fiber showing the presence of large void defects and a magnified image (a_2) shows the presence of more voids at the interior of the fiber. The void structure captured in the charred fibers are due to the burn out of PAN during charring as well as voids that may have been present upon drying out of the solvent during processing of the native fibers. (b_1) Shows the F-2 composite fibers which exhibits both medium-sized voids (i.e., as compared to the F-1 fiber) and SWNT aggregates. At higher magnification (b_2) the highly entangled SWNT agglomerates can be clearly visualized. (c_1) and (c_2) show a more uniform distribution of SWNT and presence of small voids for the F-3 composite fiber.*[46]

Wide-angle X-ray diffraction (WAXD) was used to further study the morphology of the PAN/SWNT fiber batches in terms of the polymer crystal size, crystallinity, and orientation. Figure 4.4.3a to 4.4.3c show the WAXD patterns of the F-1, F-2, and F-3 fibers, respectively. To distinguish PAN peaks from the carbon reflections, a reference WAXD pattern of the pertaining to the as-received SWNT powder is also shown in Figure 4.4.3d. The PAN crystal sizes (L) for the predominant crystallization plane *(110)* were calculated based on Scherrer's approach (Equation 4.4.1) for all the composite fibers.

$$B(2\theta) = \frac{K\lambda}{L\cos(\theta)} \tag{4.4.1}$$

λ is the X-ray wavelength of 0.1541 nm, K is the Scherrer constant taken to be 0.9, θ is the Bragg angle in radians, and B is the full-width at half maximum (FWHM) at the 2θ angle for the *(110)* plane in radians. The average crystal sizes for the *(110)* plane for the F-1, F-2, and F-3 fibers were calculated to be 11.2, 11.5, and 11.8 nm, respectively (Figure 4.4.3e). By fitting both crystalline and amorphous peaks from the WAXD patterns, the crystallinity values for F-1, F-2, and F-3 were determined to be 51.7%, 50.2%, and 53.8%, respectively (Figure 4.4.3e). As the SWNT dispersion quality improves from F-1 to F-3 batches, the polymer crystal size and crystallinity changes only slightly indicating that the SWNT does not have a major influence on the PAN crystal growth process.

The influence of the SWNT dispersion quality on the overall polymer orientation was also studied by calculating the Herman's orientation factor (*f*) from the PAN *(110)* and *(020)* WAXD diffraction planes using Wilchinsky's equation[55] (Equation 4.4.2).

$$\left\langle \cos^2 \theta \right\rangle_{c-axis} = 1 - \frac{\left(1 - 2\sin^2 \rho_2\right)\left\langle \cos^2 \varphi_1 \right\rangle - \left(1 - 2\sin^2 \rho_1\right)\left\langle \cos^2 \varphi_2 \right\rangle}{\sin^2 \rho_1 - \sin^2 \rho_2} \tag{4.4.2}$$

$\left\langle \cos^2 \varphi \right\rangle$ is determined using Equation 4.4.3:

$$\left\langle \cos^2 \varphi \right\rangle_{(hkl)} = \frac{\int_0^{\frac{\pi}{x}} I(\varphi)\cos^2 \varphi \sin \varphi \, d\varphi}{\int_0^{\frac{\pi}{x}} I(\varphi) \sin \varphi \, d\varphi} \tag{4.4.3}$$

The Herman's orientation factor (*f*) for the polymer chains is determined using $\left\langle \cos^2 \theta \right\rangle$ obtained from Wilchinski's approach using Equation 4.4.4:

$$f = \frac{3\left\langle \cos^2 \theta \right\rangle - 1}{2} \tag{4.4.4}$$

The subscripts *1* and *2* correspond to the *(110)* and *(020)* planes, respectively, and ρ_1 and ρ_2 are the angles between the plane normal of these two planes and the *b*-axis. $I(\varphi)$ is the integrated azimuthal intensity for each crystalline peak with respect to the azimuthal angle (φ). The azimuthal scans for both *(110)* and *(020)* planes are plotted in Figures 4.4.3f and 4.4.3g, respectively. Based on the azimuthal curves the FWHM decreases as the orientation factor increases, and is most pronounced for both the *(110)* and *(020)* planes for the F-3 fibers. The parameters and calculated orientation factors for all the composite fibers are listed in Table 4.4.2. As compared to the crystal size and crystallinity, which only exhibit slight changes as the SWNT dispersion quality increased, the improvement in orientation of the polymer chains is much more pronounced. This increase can be contributed to the improvement in homogeneity of SWNT bundle-size, the reduction of the SWNT agglomerations, as well as the increase in PAN-SWNT interactions (i.e., no evidence of PAN-rich regions) within the fibers. All three features may play a role for improving PAN chains alignment and promoting PAN-SWNT interfacial interactions during processing.

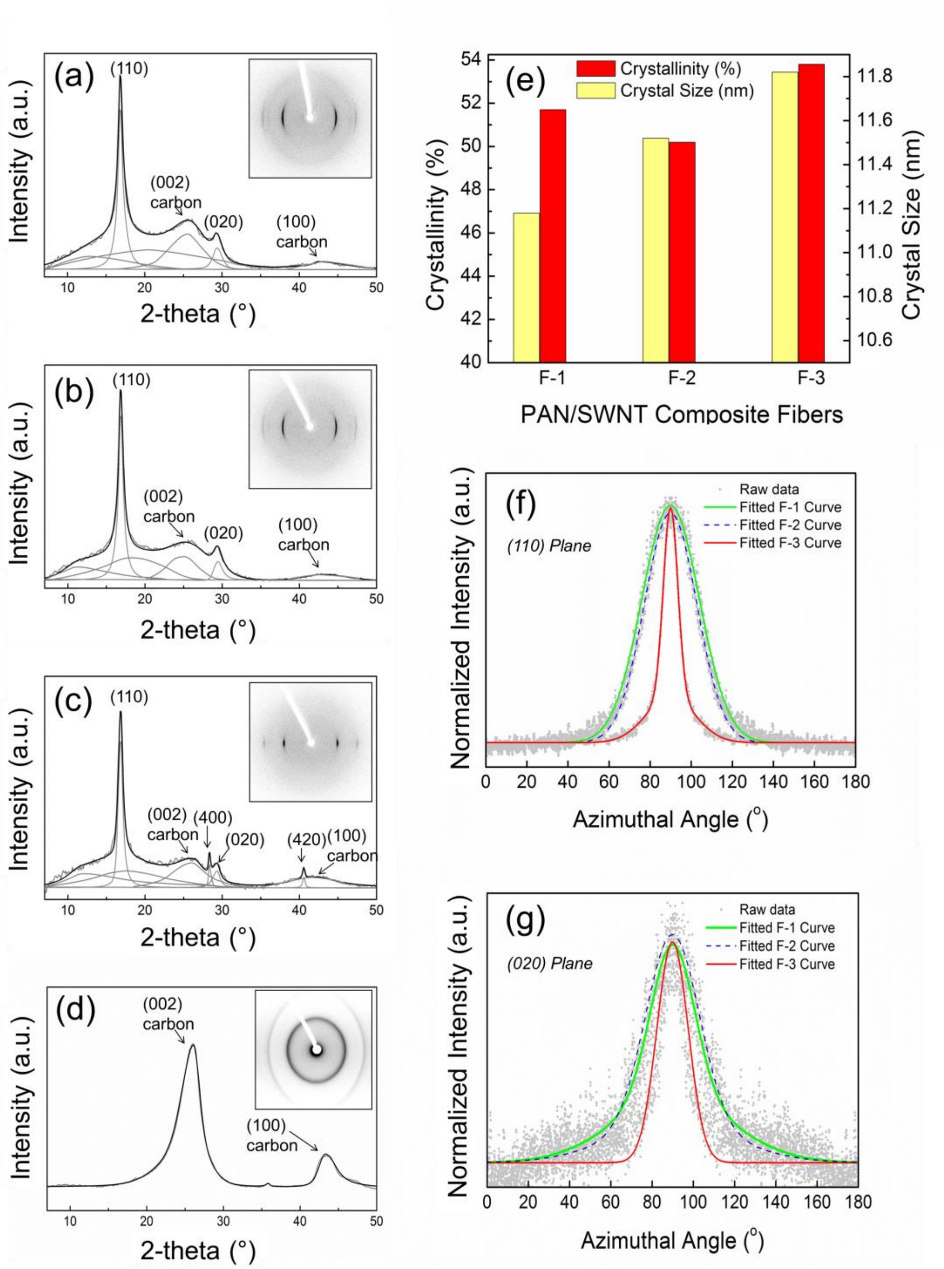

Figure 4.4.3. *Wide-angle X-ray Diffraction (WAXD) patterns for F-1 (a), F-2 (b), F-3 (c) fibers, and (d) SWNT material. (e) The comparison of PAN crystallinities and crystal sizes in F-1, F-2, and F-3 fibers as a function of the SWNT dispersion qualities, respectively. (f) Azimuthal scans and fitted curves for the (110) and (g) (020) diffraction planes from WAXD patterns.*[46]

Table 4.4.2. *Parameters used for calculating the effective Young's modulus and orientation factor (f) of PAN, as well as the effective Young's modulus of contribution of SWNT in all three composite fibers which show a variation in dispersion of the filler.*[46]

		F-1	**F-2**	**F-3**
Parameters for Calculating f_{PAN} and $E_{PAN-eff}$	E_1 (GPa) (Control Fiber Modulus)	22.1	22.1	22.1
	E_2 (GPa) [56]	10	10	10
	v_{12}	0.5	0.5	0.5
	G_{12} (GPa)	1	1	1
	$\left\langle \cos^2 \theta_{110} \right\rangle$	0.06	0.06	0.04
	$\left\langle \cos^4 \theta_{110} \right\rangle$	0.01	0.01	0.01
	ρ_1 (°)	59.1	59.1	59.1
	ρ_2 (°)	0	0	0
	F	**0.75**	**0.77**	**0.79**
	$E_{PAN-eff}$ (GPa)	**7.3**	**7.3**	**8.2**
Parameters for Calculating $E_{SWNT-eff}$	E_c *(GPa)*	12.8 ± 0.9	18.4 ± 2.2	32.4 ± 3.8
	V_f	0.128	0.128	0.128
	$E_{SWNT-eff}$ (GPa)	**50.4**	**94.2**	**197.4**

Based on this structural analysis it can be concluded that the improvement in the mechanical performance of the fiber batches from F-1 to F-3 is related to the improvements of PAN orientation, SWNT orientation, and SWNT dispersion quality. The increase in modulus is related to increase of orientation for filler and polymer, while the increase in strength is due to decrease in defective features such as voids and SWNT aggregations. Although the crystallinity and crystal size exhibits only slight improvement, the global distribution of these regions is more uniform as the filler distribution becomes more homogeneous. It is noted that as the SWNT dispersion quality improves, the PAN-SWNT interaction becomes more pronounced and the SWNT may also act as a template for PAN-alignment. These interactions are further explored using full atomistic computational analysis, but first we assess the composite system theoretically.

Theoretical Analysis

In order to analyze the stiffness contribution from the SWNT in the composites, the theoretical rule-of-mixture treatment was used (Equation 4.4.5) to calculate the effective modulus contribution of the SWNT filler in all composite fibers:

$$E_c = \left(E_{SWNT-eff} - E_{PAN}\right)V_f + E_{PAN-eff} \qquad (4.4.5)$$

V_f is the volume fraction of SWNT in the composite fibers, and $E_{PAN-eff}$ and $E_{SWNT-eff}$ are the effective Young's modulus of the PAN and the SWNT, respectively. As discussed, PAN orientation was assessed by WAXD analysis. This data was used to determine the effective Young's modulus values for PAN ($E_{PAN-eff}$), in each of the fibers (Equation 4.4.6) to be used in conjunction with Equation 4.4.5:[57]

$$\frac{1}{E_{PAN-eff}} = \frac{1}{E_1} + \left(\frac{1}{G_{12}} - \frac{2\nu_{12}}{E_1} - \frac{2}{E_2} \right) \left\langle \cos^2 \theta \right\rangle + \left(\frac{1}{E_1} + \frac{1}{E_2} - \frac{1}{G_{12}} + \frac{2\nu_{12}}{E_1} \right) \left\langle \cos^4 \theta \right\rangle \tag{4.4.6}$$

$\left\langle \cos^2 \theta \right\rangle$ and $\left\langle \cos^4 \theta \right\rangle$ values are determined using Equations 4.4.7 and 4.4.8.

$$\left\langle \cos^2 \theta \right\rangle = \frac{\int_0^{\frac{1}{2}\pi} I(\theta) \cos^2 \theta \sin \theta \, d\theta}{\int_0^{\frac{1}{2}\pi} I(\theta) \sin \theta \, d\theta} \tag{4.4.7}$$

$$\left\langle \cos^4 \theta \right\rangle = \frac{\int_0^{\frac{1}{2}\pi} I(\theta) \cos^4 \theta \sin \theta \, d\theta}{\int_0^{\frac{1}{2}\pi} I(\theta) \sin \theta \, d\theta} \tag{4.4.8}$$

E_1, E_2, G_{12} and v_{12} are the longitudinal modulus, transverse modulus, in-plane shear modulus, and the Poisson's ratio of PAN, respectively. All parameters as well as the calculated $E_{PAN-eff}$ values are listed in Table 4.4.2.

By using the experimentally measured values for the composite fiber modulus (i.e., E_c), the effective contribution of SWNT pertaining to each batch (i.e., F-1, F-2, and F-3) is determined (Table 4.4.2). The effective SWNT moduli values are within the range of the experimentally determined properties for SWNT ropes.[58] This analysis also shows that the effective modulus contribution of the SWNT improves as the dispersion qualities increase. The increase of the effective SWNT contribution is indicative of better stress transfer from the PAN matrix to the tubes. The highest effective contribution of SWNT (~197 GPa) was found in F-3 fibers, which exhibits the most uniform SWNT dispersion, highest PAN orientation, crystal size, and percent crystallinity. This theoretical treatment also supports the notion that PAN-SWNT interactions improve with dispersion quality.

Computational Analysis

Both the experimental and theoretical sections support the evidence that as the SWNT dispersion improves, the composite mechanical properties increase. To complement experimental observations and theoretical predictions, full atomistic computational analysis is implemented to fundamentally explore how very slight changes in SWNT dispersion lead to significant differences in PAN-SWNT interactions, as well as in PAN conformational changes which will contribute to the property improvements. Using full atomistic molecular models allows precise control of the SWNT dispersion, enabling the exploration of minute changes in system conformation, unable to be achieved and/or controlled experimentally. To understand the fundamental issues relating processing approaches to the final fiber structure as well as the ultimate properties, the molecular interactions between the PAN and SWNT are explored at the smallest molecular interfacial scale. To simplify the computational models used here for investigating such interactions the assumption is made that the PAN-SWNT interactions occur in primarily two main combinations (1) individual SWNT to individual PAN chains, and (2) SWNT bundles to PAN chains. Experimentally, these two major polymer-SWNT interactions have been recognized.[59-63] Similarly, some studies have also been performed from a computational viewpoint in order to obtain molecular level information or to study conditions that are not accessible experimentally.[64-69] Here, the computational models are defined by taking both the experimental and theoretical results into consideration in order to assess the best possible representation of the PAN-SWNT molecular interactions observed in the composite fiber.

The PAN-SWNT molecular interactions can vary greatly depending on either simple surface or confined interactions between the polymer chains and the nanotubes. To evaluate these molecular effects, the interaction energy between the PAN chains and SWNT is studied in five scenarios. These scenarios include two *surface variations* (a) PAN chain interactions with and individual SWNT (small diameter) and (b) PAN chain interactions with a SWNT bundle (19 tubes of total 8.9 nm diameter), as well as three *confinement variations* (c) PAN chains confined by SWNT bundles, (d) PAN chains confined by a mixture of SWNT bundles and individual tubes, and (e) PAN chains confined by individual (i.e., exfoliated) SWNT. The confinement variations provide a local evaluation of molecular interactions, which are more likely to occur in a composite material, where the polymer is actually surrounded (i.e., confined) by the SWNT. In order to understand the energetic and conformational changes as a result of PAN-SWNT interactions variation (i.e., different degrees of interactions due to the dispersion development), a series of full atomistic MD simulations were performed to study both the PAN-SWNT and PAN-PAN interaction energies for each of the aforementioned scenarios (Figure 4.4.4).

The two scenarios exploring the basic PAN-SWNT surface interactions are shown in Figure 4.4.4a and 4.4.4b. Three PAN chains are located near the surface of an individual SWNT (case 1, Figure 4.4.4a_1) and a SWNT bundle (case 2, Figure 4.4.4b_1). Both systems were allowed to freely interact at 300 K for 2 ns while the interaction energies were recorded. The final configurations for case 1 and 2 are shown in Figures 4.4.4a_2 and 4.4.4b_2, respectively. The average PAN-SWNT and PAN-PAN interaction energies per PAN monomer after three simulations for each case were also recorded (Figures 4.4.5).

Based on the simulation results analyzing *surface variations*, case 1 (Figures 4.4.4a_1 and 4.4.4a_2), shows that while there is some degree of PAN-SWNT interaction, the PAN-PAN interaction energy was predominant, e.g., polymer self-aggregation is energetically favorable. For this reason, a local PAN rich region is formed near the SWNT surface. Case 2 (Figures 4.4.4b_1 and 4.4.4b_2), exhibits an improvement of the PAN-SWNT interaction and a decrease in PAN-PAN interaction energy. Due to the increase in graphitic surface available, the polymer chains to have more opportunity to interact with the SWNT bundle. It is understood that predominant PAN-PAN interactions throughout the composite fiber system would lower the stress transfer efficiency from the matrix to the SWNT. However, better matrix/filler interaction will lessen PAN inter-chain interactions. These simple surface studies show that, in isolation, the PAN chains prefer polymer-polymer interactions rather than polymer-SWNT interactions. However, increasing the presence of SWNT (and thus the available surface area) in the near vicinity can reduce PAN chains self-interactions by increasing the interfacial polymer-nanotube conformational space. It is also noted that the PAN chains exhibits a coiled conformation on the SWNT surface. These results may provide some insight toward the experimental observation of polymer-rich and SWNT-rich regions forming in the composite during processing, as the inherent PAN-SWNT interaction are relatively weak.

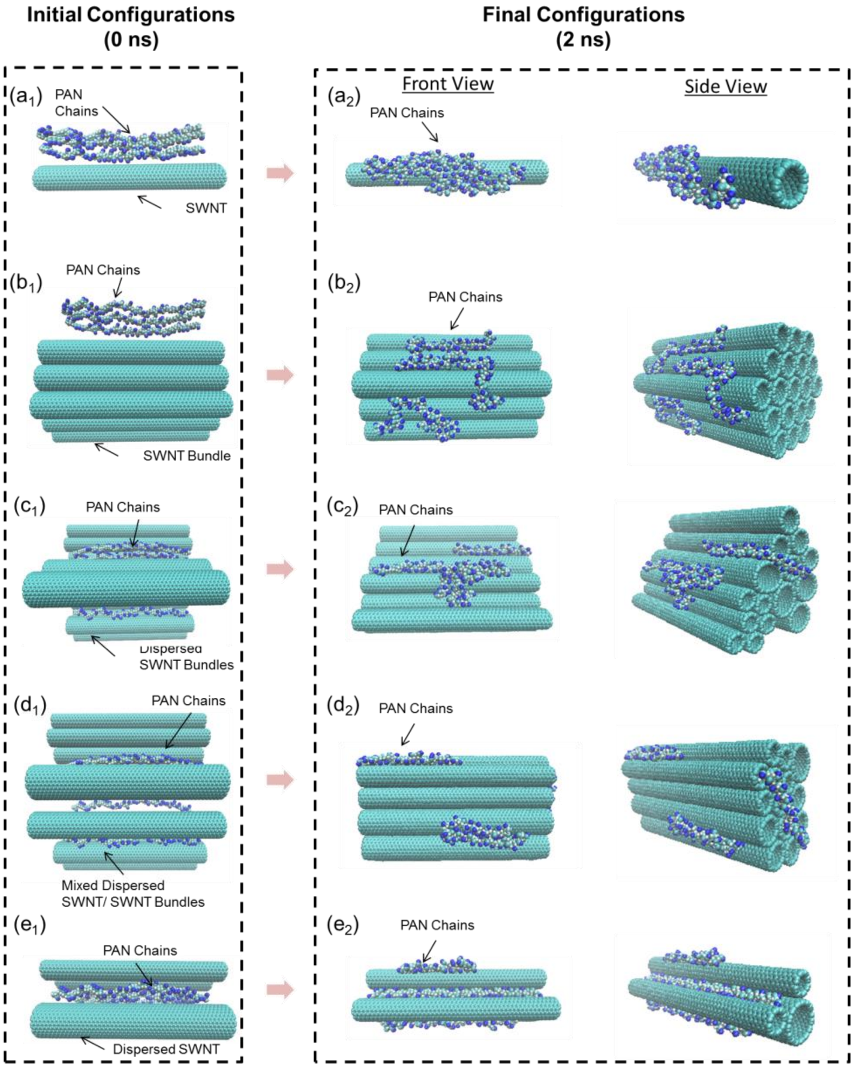

Figure 4.4.4. *(a through e) Molecular dynamics simulation snapshots of PAN/SWNT free interactions under 300 K with initial configurations of: (a_1) case 1: three PAN chains located on one side of a SWNT, (b_1) case 2: three PAN chains located on one side of a SWNT bundle, (c_1) case 3: three PAN chains located inside and outside of the dispersed SWNT bundles with different bundle sizes, (d_1) case 4: three PAN chains located within space of the mixture of SWNT bundles and individual SWNT, and (e_1) case 5: three PAN chains located within space of the dispersed individual SWNT. The final configurations of each case after 2 ns were shown in (a_2), (b_2), (c_2), (d_2) and (e_2), respectively.*[46]

To study the *confinement variations* on the PAN-SWNT interactions, three additional cases with different SWNT dispersion qualities were constructed and analyzed. The differences between these three cases are in relation to the size and distribution as well as dispersion of the SWNT bundles and individual tubes. Three PAN chains are surrounded (i.e., confined) by dispersed SWNT bundles (case 3, Figure 4.4.4c), mixture of dispersed SWNT bundles/tubes (case 4, Figure 4.4.4d), and dispersed individual SWNT (case 5, Figure 4.4.4e), respectively. Similar to the surface studies, all systems were allowed to freely interact at 300 K for 2 ns while the interaction energies were recorded. The final configurations for cases 3 to 5 are shown in Figures 4.4.4c_2, 4.4.4$d_{2,}$ and 4.4.4e_2, respectively. The average PAN-SWNT and PAN-PAN interaction energies per PAN monomer of three simulations for each case are shown and summarized in Figures 4.4.5a, 4.4.5b, and 4.4.5c, respectively. It should be noted that, for all current simulations, no solvent molecules were included in the models. As such, the absolute values of interaction energies may change with the presence and type of solvent. That being said, the trends of the energy changes from case to case should remain qualitatively consistent, since the same solvent effect would be equally imposed throughout all cases.

Both case 3 and 4 exhibit PAN-SWNT and PAN-PAN interaction energy levels similar to case 2 (PAN-SWNT bundle surface interactions). As the dispersion level was increased to full exfoliation of the SWNT tubes for case 5 (Figures 4.4.4e_1 and 4.4.4e_2), the highest PAN-SWNT bonding energy and the lowest PAN-PAN interaction energy was observed (Figure 4.4.5). Simulation snapshots also depict that the PAN chain conformation becomes more extended due to confinement between the SWNT. As the SWNT dispersion becomes more uniform, this conformational confinement effect is more pronounced. Case 5 exhibits fully extended-chain PAN morphology in the vicinity of the SWNT surface (Figure 4.4.4e). As discussed in the introductory section, this extended-chain morphology is considered to be a major factor in maximizing the stress-transfer from a matrix to SWNT and significantly enhances the composite fiber performance. It has also been experimentally confirmed by observing the crystallization behavior of PAN in the dilute SWNT dispersion.[6]

The simulation results suggest that, as SWNT exfoliation and dispersion (i.e., distribution of PAN and SWNT) improve, the PAN molecular conformation and its interaction with the SWNT increased from case 1 to case 5. Therefore, by combining the experimental evidence (i.e., increase in mechanical properties, crystal size, orientation, and crystallinity as the SWNT dispersion quality improved) and the SWNT effective modulus analysis (i.e., SWNT effective modulus increased as the dispersion quality improved) deduced by theoretical analysis, the difference in the mechanical performance from F-1 to F-3 fibers may be explained by the various compositions of different PAN-SWNT interaction levels within composite fibers. Understanding the importance of improving polymer-SWNT interactions for composite performance enhancement has been recognized for some time, this study provides critical and complementary computational and experimental evidence indicating how molecular conformation and confinement evolve and vary with nanotube dispersion and translate to structural features within the material.

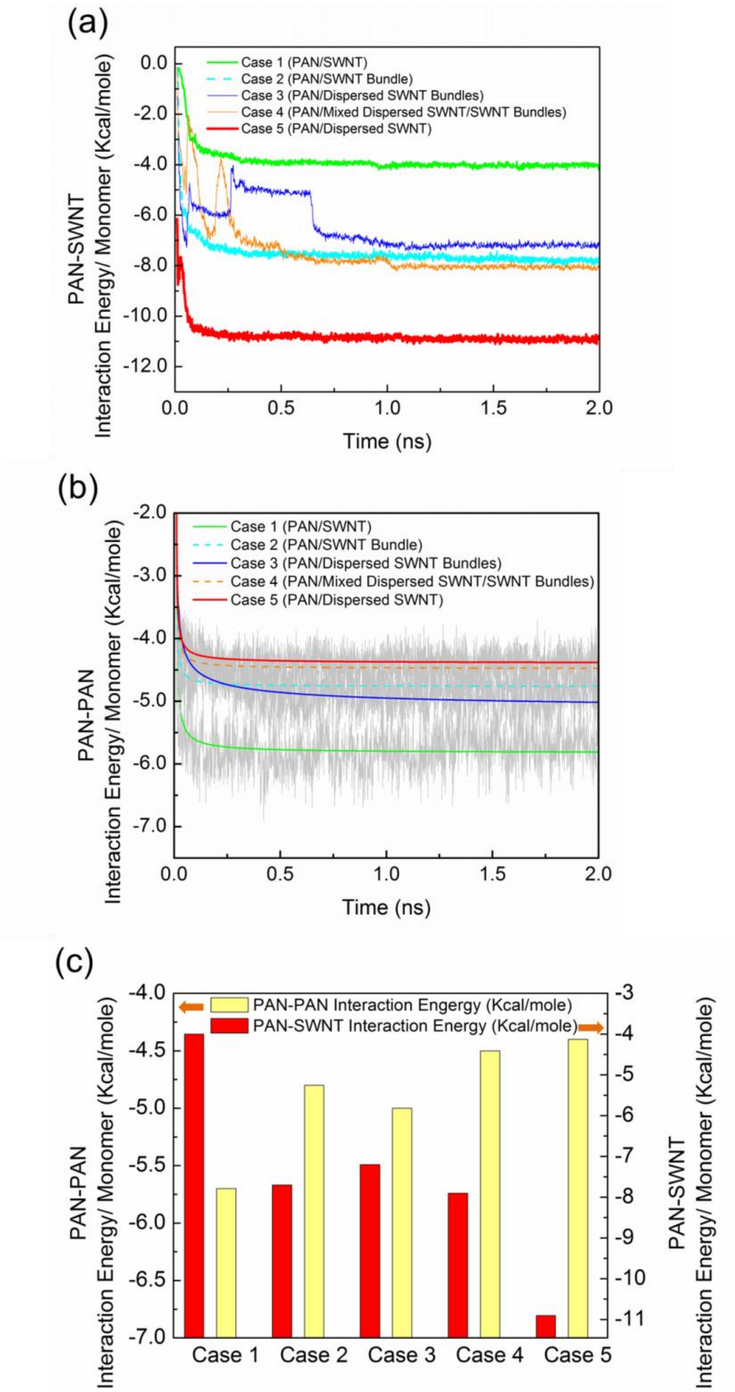

Figure 4.4.5. *(a) PAN-SWNT and (b) fitted PAN-PAN interaction energies for all cases were plotted. (c) A summary bar chart for all interaction energy values, where PAN-PAN interaction energies increase (weaken) and PAN-SWNT interaction energies decrease (strengthen) as the SWNT dispersion quality and distribution increases.*[46]

Conclusions

Three sets of PAN/SWNT composite fibers with high concentration of SWNT (10 wt%) were produced using a flow gel-spinning apparatus. Although following the same fiber-spinning procedure, significant difference in fibers mechanical performances was observed. SEM images of all fibers after thermal-charring process revealed different SWNT dispersion qualities within composite fibers. A Young's modulus ratio of 1:1.4:2.5 and a tensile strength ratio of 1:1.9:3.2 were found for the first (F-1), the second (F-2) and the third (F-3) sets of composite fibers, respectively. WAXD analysis suggested slight increases in PAN crystal size and crystallinity, as well as a significant increase in polymer orientation as SWNT dispersion quality improved. The mechanical contributions from SWNT bundles for all composite fibers were calculated using the rule-of-mixture expression by taking orientation factor into account. The calculated values showed an increase in SWNT contribution as the dispersion quality improved. To provide a molecular perspective, full atomistic MD simulations on various SWNT dispersion conditions showed a positive correlation between PAN-SWNT interaction and the SWNT dispersion quality. Confinement of PAN chains between well-dispersed SWNT results in conformational changes of the polymer leading to extended-chain structures. These results provide insight toward the formation of PAN ordered interphase structures in the nano-composite fiber, as well as the importance of good dispersion of the nano-filler. Such interactions can contribute to the improvement of the fiber mechanical properties maximizing the stress transfer from the matrix to the fillers.

C. FIBRILLAR CRYSTALLIZATION TOWARD INTERPHASE FORMATION IN POLYMER COMPOSITE FIBERS

Study 5: Polyethylene/CNC Fibers

This study looks at using fibrillar crystallization approaches to form composite fibers with interphase structures. The polymer is crystallized under flow in the presence of the nano-carbon. The ability of the nano-carbon to template polymer crystal growth and orientation is examined for its influence on interphase structures.

Experimental Section

Materials

All reagents were used without further purification. Xylenes (Certified ACS) and ultra-high molecular weight polyethylene (UHMWPE) ($\overline{M}_w$ 3,000,000-6,000,000 g/mol) were purchased from Sigma-Aldrich Co. Carbon Nano-chip Fibers (CNCF) (purity >99 wt% C; batch H700) were purchased from Catalytic Materials.

Fabrication of PE/CNCF Fibrillar Crystals

Xylenes were used to both dissolve PE and disperse CNCF. PE was dissolved in xylenes between 130 to 140 ºC at a concentration of 0.02 wt%. CNCF were sonicated in xylenes at a concentration of 1.7 mg/mL in a bath sonicator (Fisher FS30 bath sonicator, frequency 43 kHz, power 50 W) for 24 hrs at ~55 ºC. Fibrillar crystallization was performed in a number of steps. First, the PE/xylene solution was subject to shear flow using an overhead mechanical stirrer (Eurostar power-b IKA® WERKE stirrer). The stir rod is composed of a shaft fitted with a cylindrical stirrer made of Teflon. A shaft rotation speed of 800 RPM was used to dissolve PE in xylenes. Once fully dissolved the solution temperature was reduced to the crystallization temperature of PE around 90 ºC. Before injection of the CNCF, the dispersion was re-sonicated for approximately 5 to 10 min to ensure uniform dispersion. A glass syringe with a 26 gauge blunt tip needle was used to inject 1 mL of SWNT dispersion into the PE solution in order to achieve a 4:1 ratio of PE to CNCF. Fibrillar crystals were collected on the stir bar and removed for subsequent analysis. Drawing of the fibers was performed on a hot plate at 130 ºC with draw ratios ranging from 1.5 to 3.

Sample Characterization

Scanning electron microscopy (SEM) images were taken on either a JOEL 6320 HR-SEM or a Zeiss Supra 25 Field Scanning SEM. Samples were coated with gold/palladium for imaging (operation voltage 5 kV). Wide-Angle X-ray diffraction (WAXD) data was obtained using a Rigaku RAPID II curved detector system with a 3 kW sealed tube source (operating voltage 40 KV, current 30 mA, wavelength 0.1541 nm). WAXD data was analyzed using PDXL software from Rigaku and curve fitting was done in Origin 6.1. Small-Angle X-ray scattering (SAXS) diffraction was performed on a Rigaku MicroMax-007HF system with CuK_{α} radiation (operation voltage 40 kV and current 30 mA). Differential scanning calorimetry (DSC) was performed on a Q200 differential scanning calorimeter (manufactured by TA instruments). The heating rate was 10 ºC/min from room temperature (25 ºC) up to 250 ºC. Mechanical testing of the fibers was done on a RSA-G2 analyzer (TA Instruments). The gauge length was 10 mm and the strain rate was 0.02 mm/s.

Results and Discussions

Polyethylene (PE)/carbon nano-chips fiber (CNCF) fibrillar crystals were grown under shear flow. The fibrillar crystals ranged from 25 to 200 nm in diameter and bundled to form PE/CNCF macro-fibers. Scanning electron microscopy showed that the PE/CNCF macro-fiber exhibits a core (i.e., CNCF-rich) -shell (i.e., PE-rich) structure formed during crystallization. The PE/CNCF fibers were further processed by hot-drawing near the PE melting temperature. Based on small-angle X-ray analysis, it was found that during drawing the presence of CNCF led to continuous extended-chain crystal growth. DSC melting peaks associated with transformation of the orthorhombic to a hexagonal lattice phase in the PE crystal structure (i.e., associated with increased ordering and extension of the polymer chain along the chain axis) was also observed for drawn hybrid PE/CNCF fibrillar crystals. The overall Herman's orientation factor (*f*) for PE alignment in the presence of CNCF was 0.85 as compared to the 0.74 for the control drawn fibers. The orientation of extended-chain (i.e., shish) crystals in the presence of the CNCF as compared to the control fiber also improved from 0.88 to 0.93. This work shows the direct evidence that these nano-carbon fillers can promote extended-chain polymer crystal growth under shear.

Morphology and Structure

PE control and PE/CNCF fibrillar crystals were fabricated under shear flow. Both control and composite resultant fibers consist of bundled fibrillar crystals which exhibit a shish-kebab structure (Figure 4.5.1). The fibrillar crystals range in size from 25 to 200 nm. This shish-kebab (SK) structure has been observed previously for both systems under shear.[70-72] The presence of the SK structure is not obvious on the surface of control PE fibers due to excess polyethylene coating much of the structure (Figure 4.5.1a). This is likely due to the stir bar remaining in the solution for some time following crystallization before the fibers are removed for observation. For PE/CNCF fibers the fibrillar crystal bundles are more apparent even at the fiber surface, therefore the SK morphology can be observed for the unwashed composites (Figure 4.5.1b).

In this study the solid CNCF concentration was ~25 wt% as compared to the PE. In order to achieve dispersion of the CNCF into the fibrillar crystal, the injection speed of the CNCF dispersion was controlled at ~0.25 mL/min and the fillers were injected at the onset of PE crystal formation. It is estimated that the growth rate of the PE crystal formation under shear ranges from 2 to 40 cm/min. Due to the mismatch between the growth rate of the PE crystal and injection rate of the CNCF into the solution only a low concentration of CNCF was incorporated evenly into the fibrillar crystals,[73] while less dispersed CNCF adhered to the surface of the hybrid fibrillar structure. Under these conditions a core-shell structure is observed for the PE/CNCF hybrids (Figure 4.5.1c). The core of the fibrillar structure is PE-rich where the CNCF are well dispersed, while being surrounded by a CNCF-rich region with only a small amount of polymer (Figure 4.5.1d). It was found that the crystallization temperature at which the CNCF are introduced and the CNCF injection rate played a significant role on the overall final structure of the PE/CNCF fibrillar crystal morphology. Based on SEM images, as expected, an increase in overall fibrillar alignment occurs during drawing. For both PE (Figure 4.5.1e) and PE/CNCF (Figure 4.5.1f) fibers the fibrillar bundles visually become much more aligned post hot-drawing. This change in orientation as a function of drawing is further analyzed using WAXD analysis.

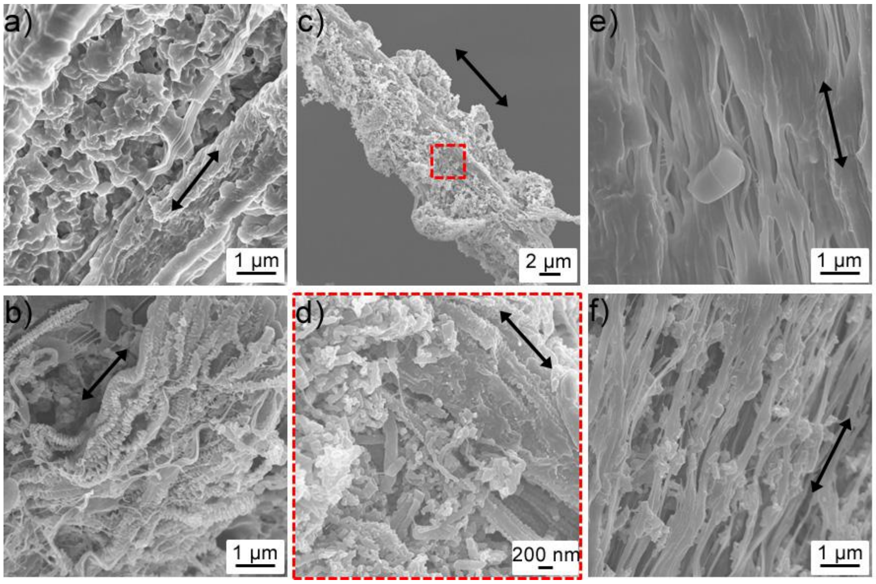

Figure 4.5.1. *Scanning electron microscopy images of the PE and PE/CNCF fibrillar structures: (a) as-spun fibrillar bundle before washing shown complete coating by excess PE, (b) washed fibrils showing shish-kebab morphology, (c) magnified image of unwashed as-spun PE control, (d) drawn PE control, (e) as-spun PE/CNCF, (f) drawn PE/CNCF, (g) low magnification image of as-spun PE/CNCF showing core/shell structure, and (h) high magnification of the boxed region in (g) also showing the core (PE-rich)/shell (CNCF-rich) regions in the hybrid fibrillar structure. Arrows indicate the direction of the fiber axis.*[74]

For the as-spun fibers three major wide-angle X-ray reflections *(110)*, *(200)*, and *(010)* are observed, and each are inherent to the polyethylene orthorhombic (*(110)* and *(200)* reflections) and triclinic (*(110)* reflection) crystal structures (Figure 4.5.2a).[75] For the composite fibers, an additional diffraction ring representing the CNCF layer spacing *(002)* is also observed (Figure 4.5.2b). Wide-angle X-ray patterns show that for both the control and composite fibers as the draw ratio increases from 1.5 to 3 the polymer chain orientation also improves (Figure 4.5.2). The CNCF orientation (i.e., *(002)* peak) does not show any obvious orientation changes owing to its inherent layered platelet structure.[76] PE chain orientation factor values (*f*) with respect to the fiber axis for each fibrillar structure were calculated using both the *(110)* and *(200)* reflection peaks by Wilchinsky's method[77] (Table 4.5.1). An orientation factor of $f = 1$ would represent fully oriented polyethylene fibrils along the fiber axis, while an orientation factor of 0 represents fibrils randomly aligned along the fiber axis. Subsequently, fibrils aligned perpendicular to the fiber axis would have an orientation factor of -0.5. The parameters used for the orientation calculations are also provided in Table 4.5.1, where ρ_{hkl} is the angle between the plane normal and c-axis of the PE unit cell, $\overline{\cos^2 \phi_{hkl}}$ is the orientation of each *(hkl)* plane determined from the X-ray azimuthal data using Wilchinsky's equation, and $\overline{\cos^2 \theta_c}$ is the overall orientation of the polymer chain with respect to the fiber axis used to determine the orientation factor.

Based on these WAXD results, composite fibers show higher degrees of orientation for both as-spun and drawn fibers as compared to the control samples (Table 4.5.1). Composite fibers drawn three times have a maximum overall average orientation value of 0.847, while for the control fibers it is only 0.786 (note: draw ratio for maximum orientation in the control fiber is 2.5 times). Greater orientation for the PE/CNCF hybrid fibrillar structures is attributed to both the sliding effect or lubricating ability of the CNCF[76] and the ability of the nano-carbon to template polymer orientation and alignment.[78-79]

Structure-Property Relationship

Further analysis of the WAXD azimuthal curves for the *(110)* and *(200)* PE peaks indicate that the overall orientation of the polymer chains represent two distinct populations. The raw azimuthal curves for the fibers as a function of draw ratio are shown in Figure 4.5.3. The azimuthal curves are fitted by two curves (Figures 4.5.4a and 4.5.4b). The broader peak represents more disordered PE associated with kebab orientation, while the narrow peak is representative of more ordered chains consistent with shish orientation. As the draw ratio increases the shoulder in the azimuthal curves begins to diminish, which is consistent with the increase in the overall chain orientation. During drawing there is a pullout of PE chains from the kebabs into shish structures as the alignment increases/improves. The hybrid PE/CNCF fibers in general show narrower intensity peaks indicating higher orientation than the control fibers. In addition, the curves for the PE/CNCF fibers show a less pronounced shoulder before drawing indicating that the orientation of the kebabs and shish crystals are more closely related. As mentioned, the calculated average orientation values as well as those associated with the kebab and shish crystal growth are all listed in Table 4.5.1. It was found that regardless of the draw ratio, PE/CNCF fibers always showed a greater overall orientation values as compared to the control fibers (Figure 4.5.4c).

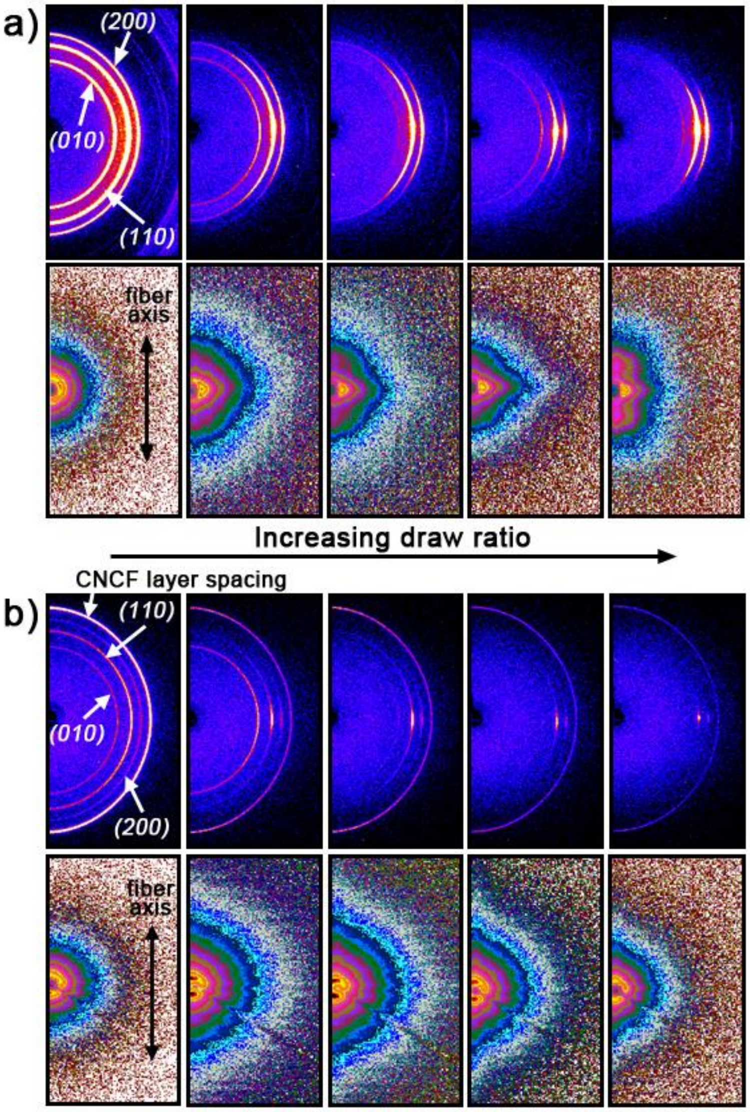

Figure 4.5.2. *Diffraction patterns from both wide-angle X-ray diffraction (upper block) and small-angle X-ray scattering (lower block) for (a) control polyethylene and (b) hybrid polyethylene/CNCF fibrillar structures as a function of draw ratio. The drawing ratios are 0, 1.5, 2, 2.5, and 3 times and increases from moving left to right in each image block.*[74]

Table 4.5.1. *Listing of Wilchinsky's method parameters as well as Herman's orientation values (f) for both control and CNCF composite polyethylene fibers at different draw ratios. f values are also calculated for the shish (i.e., narrow) and kebab (i.e., broad) orientation populations observed in the fibers (see Figures 4.5.4a and 4.5.4b).*[74]

Draw Ratio	**Wilchinsky's method parameters and Herman's orientation values**											
	Polyethylene fiber (ρ_{110} = 56.3°, ρ_{200} = 0°)						**CNCF composite fiber** (ρ_{110} = 56.3°, ρ_{200} = 0°)					
	$\cos^2\varphi_{110,avg}$	$\cos^2\varphi_{200,avg}$	$\cos^2\theta_{c,avg}$	$f_{b,avg}$	$f_{b,kebab}$	$f_{b,shish}$	$\cos^2\varphi_{110,avg}$	$\cos^2\varphi_{200,avg}$	$\cos^2\theta_{c,avg}$	$f_{b,avg}$	$f_{b,kebab}$	$f_{b,shish}$
0	0.193	0.293	0.558	0.337	0.002	0.518	0.172	0.196	0.643	0.465	0.365	0.539
1.5	0.156	0.160	0.685	0.528	0.453	0.820	0.079	0.089	0.837	0.755	0.716	0.885
2	0.130	0.133	0.739	0.608	0.543	0.837	0.065	0.069	0.867	0.801	0.747	0.913
2.5	0.066	0.086	0.857	0.786	0.610	0.913	0.052	0.058	0.892	0.839	0.797	0.936
3	0.082	0.096	0.828	0.742	0.737	0.883	0.050	0.052	0.898	0.847	0.835	0.931

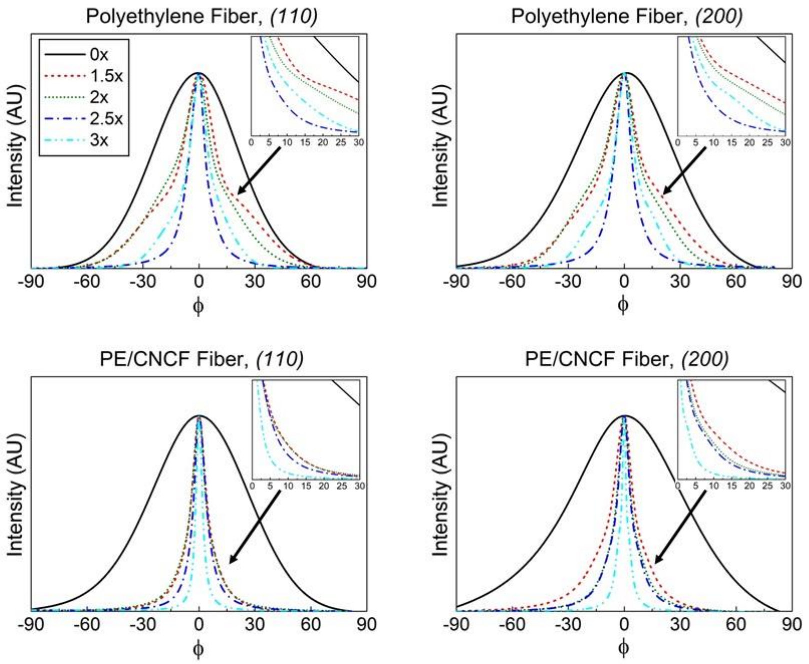

Figure 4.5.3. *Wide-angle X-ray diffraction azimuthal intensity scans of control polyethylene and composite polyethylene/CNCF fibers at each drawing stages (draw ratio: 0, 1.5, 2, 2.5, and 3) for both the predominant (110) and (200) reflections. A distinct shoulder in the azimuthal scans is observed as drawing increases. Each inset shows a magnified view of the azimuthal curves between 0 to 30° where this shoulder can be clearly observed. The fibers exhibit two populations of polymer chain orientation associated with folded and extended-chain crystals.*[74]

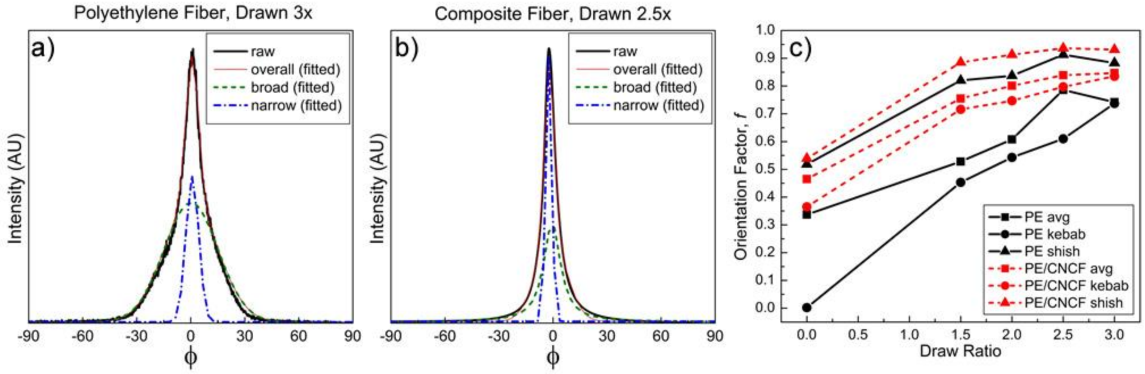

Figure 4.5.4. *Wide-angle X-ray diffraction azimuthal intensity scans for the (110) reflection and their corresponding fitting for both populations of PE orientation (i.e., associated with the shish (i.e., narrow) and kebab (i.e., broad) structures): (a) control PE - drawn 3×, (b) PE/CNCF - drawn 2.5×. (c) Graph showing the change in orientation factor as a function of drawing ratio for both PE and PE/CNCF fibrillar structures. The average orientation factors as well as those associated with the kebab and shish crystal population are also shown. The hybrid PE/CNCF samples always exhibit higher polymer chain ordering.*[74]

In addition to WAXD, SAXS measurements were also used to look at the long-range order and morphological structure of the PE and PE/CNCF fibers. The SAXS patterns for both sets of samples are shown in Figures 4.5.2a and 4.5.2b. It is clear that an equatorial streak consistent with shish crystal growth[80-81] becomes more pronounced as the draw ratio increases for the fibers. Simultaneously a meridional lobe consistent with kebab/lamellar development[80] is also observed. However, this is only obvious in the control fibers. These results show that as the draw ratio increases, more extended-chain crystals are formed. As compared to the control, the hybrid fibers exhibit a much more pronounced equatorial steak indicating a larger population of extended-chain crystals. The control fibers show a well-defined meridional lobe, and the lamellar thickness calculated from SAXS is ~48 nm (Figure 4.5.5). Meridional lobes are less pronounced and more diffused in the PE/CNCF samples. The SAXS peak intensity profiles for both samples show that development of the meridional intensity is more obvious for the control PE as compared to the PE/CNCF fibers (Figure 4.5.5). These weak and undefined meridional lobes associated with the PE/CNCF crystals illustrate that kebab development is very inconsistent in these samples. This may also indicate that the CNCF play a role in disrupting the development regular kebab periodicity during shear crystallization and subsequent drawing. In terms of the control samples, the kebab growth is more uniform. However, the large lamellar thickness and diffused scattering of the meridional lobe suggests a loose kebab structure.

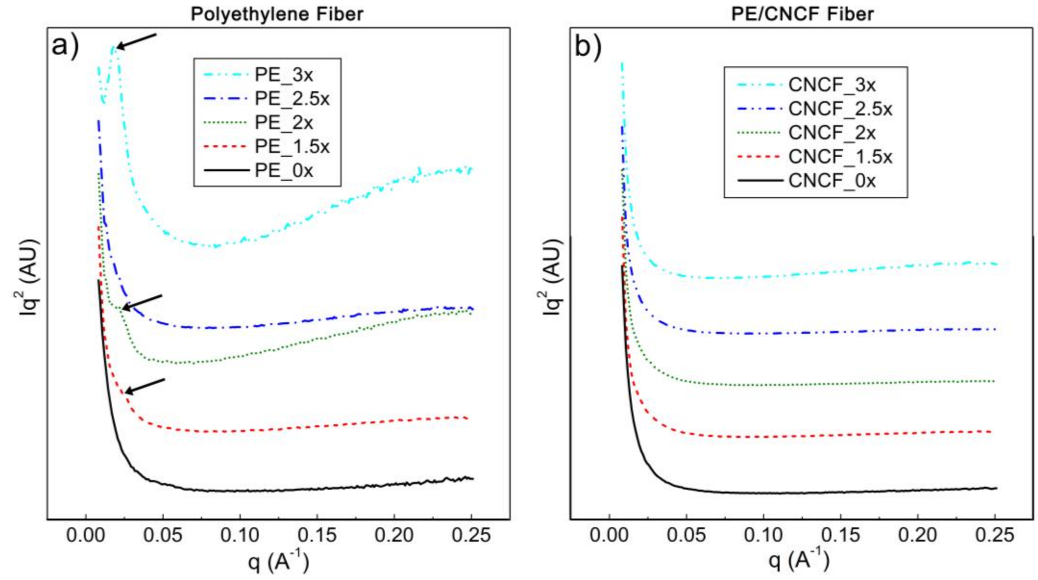

Figure 4.5.5. *Small-angle X-ray scattering intensity profiles for (a) PE and (b) PE/CNCF fibers. Iq^2 as a function of q (* $q = 4\pi/\lambda \sin\theta$*) shows the development of the meridional intensity (kebabs) for the control polyethylene fibrillar crystals. Lamellar thickness of the polyethylene fibrillar crystals with a draw ratio of three is ~48 nm. No distinct meridional lobe is detected for the PE/CNCF samples therefore an average kebab thickness could not be determined. The lack of meridional SAXS reflection in the hybrid samples shows that the kebabs formed are most likely irregular and not periodic.*[74]

To further compare shish versus kebab growth, the Halo method[82] was used to determine the change in SAXS intensity along the equatorial and meridional directions (Figure 4.5.6). Azimuthal scans were taken as a function of φ, for each pattern, and plotted against q (the diffraction vector $q = 4\pi/\lambda \sin\theta$, where λ is the wavelength of the X-ray beam and θ is the Bragg angle at which the scattering peak is observed). The azimuthal intensities for the undrawn samples were used as baseline measurements for the initial existence of the kebab and shish in the as-prepared fibers. The changes in equatorial and meridional intensities were determined by subtracting the SAXS azimuthal intensity profiles of the each sample at increasing draw ratio from the baseline intensity. Based on this analysis, it is shown that up to about a draw ratio of two, the shish and kebab crystals grow at a relatively even rate (Figure 4.5.6). At this point there is a change where the shish growth becomes more dominant in both samples as the draw ratio is further increased to 2.5 times. Upon further drawing, for the control fibers the shish growth reaches a plateau and kebab growth becomes most dominant. This may be related to the self-seeding of PE kebab growth on shish in the SK structure.[83] On the other hand for the PE/CNCF fibers, shish growth continues to be most predominant indicating that the presence of the nano-carbon helps to promote extended-chain formation.

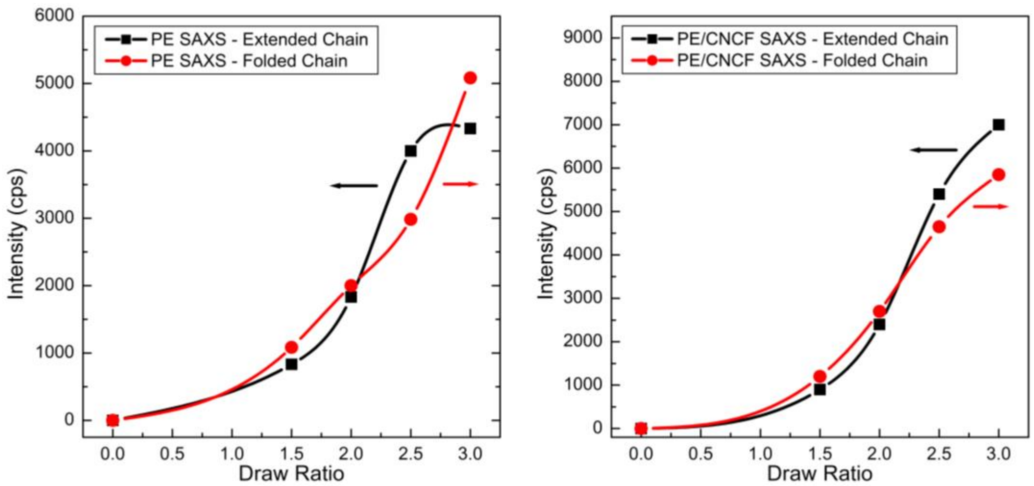

Figure 4.5.6. *Plot of the small-angle scattering intensity along the equatorial (i.e., extended-chain) and meridional (i.e., folded chain) directions as a function of draw ratio for both the control and hybrid PE/CNCF fibers.*[74]

In addition to the orientation calculations, the WAXD data also shows that both PE and PE/CNCF fibers produced are highly crystalline. Both crystallinity of the fibers and crystal size for each *(hkl)* peak were measured. The crystallinity for the fibers is very high (Table 4.5.2) and this is expected since both the control and PE/CNCF fibers are grown using shear crystallization procedures. There is also no significant change in the overall crystallinity as a function of drawing. Polyethylene crystal sizes for both as-spun and drawn control and hybrid fibers are also provided in Table 4.5.2. For both fibers, the crystal size remains similar as the draw ratio increases. The fibers are drawn near the melting temperature at 130 °C, therefore, it is expected that rearrangement of the polymer chains during drawing will cause slight variations in the crystal size. The weaker *(010)* peak which is associated with a PE triclinic phase/modification[73] diminishes as the drawing increases. In this study, to increase the draw ratio the fibers drawn are exposed to the hot plate (at 130 °C) for longer duration times. The presence of the triclinic phase is indicated by the *(010)* peak and is known to disappear around 130 °C.[71] Therefore, the diminishment of this peak becomes more pronounced at higher draw ratio.

Table 4.5.2. *Listing of the crystal size for the major (010), (110), and (200) reflections as well as the crystallinity measured from wide-angle X-ray diffraction. The enthalpy of melting determined from differential scanning calorimetry is also listed for as-spun and drawn control PE and PE/CNCF composite fibers.*[74]

Draw Ratio	**Polyethylene Fiber**					**PE/CNCF Composite Fiber**				
	Crystal Size, L_{hkl} (nm)			Crystallinity (%)	ΔH (J/g)	Crystal Size, L_{hkl} (nm)			Crystallinity (%)	ΔH (J/g)
	(010)$_{triclinic}$	*(110)*	*(200)*			*(010)*$_{triclinic}$	*(110)*	*(200)*		
0	23	19	16	97	87.0	25	22	17	91	54.71
1.5	12	21	18	98	129.1	26	20	17	87	32.25
2	21	21	18	98	209.0	23	20	16	86	57.01
2.5	17	20	17	95	130.3		17	17	88	26.65
3		21	18	96	119.1	17	16	17	87	39.18

Thermal analysis using DSC was also performed on both the PE and PE/CNCF fiber samples. DSC analysis of the as-received PE powders shows a single melting isotherm for the unconstrained crystals. For the PE and PE/CNCF fibers the melting endotherms observed are associated with melting of both the unconstrained and constrained PE fibrillar crystals. It is observed that the overall enthalpy of melting for the PE/CNCF fibers is lower than that of the control fibers (Table 4.5.2). This provides evidence that the interaction between the hybrid PE/CNCF fibrillar crystals results in more confinement of the PE chains due to the presence of the CNCF. As drawing of the PE/CNCF samples increases the degree of fibrillar crystal confinement also increases. For the control PE samples, there are a larger percentage of unconstrained fibrillar crystals. However, there is a noticeable shift in the melting temperature for the unconstrained fibrillar crystals as a function of drawing. This is due to the increase of order in the crystals as evidenced by WAXD and SAXS studies discussed earlier.

For PE/CNCF samples a new peak at ~150 ºC, is also observed post drawing (i.e., draw ratio 2.5 and 3) (Figure 4.5.7), and this is not observed in the control samples. This high order peak is attributed to a transformation of the orthorhombic PE to a hexagonal lattice.[84] This transition is often observed in constrained fibrillar crystal samples.[84] The hexagonal packed crystals are also the most ordered PE crystals and consist of extended-chain PE. The evidence of this peak in the hybrid structures suggests that the presence of CNCF alone is responsible for inducing this most ordered crystal structure growth. Prior work has also shown the ability of these unique nano-carbons to act as lubricating agents to facilitate polymer chain extension.[76] During drawing the CNCF are able to template highly ordered extended-chain PE.

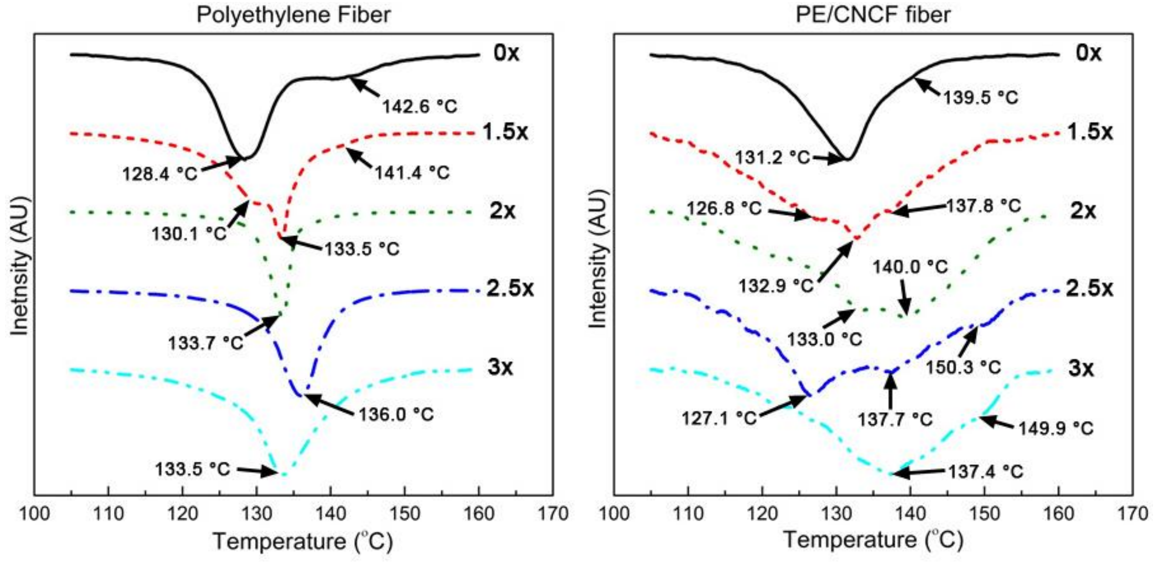

Figure 4.5.7. *Differential scanning calorimetry curves showing the melting transition for both control PE and hybrid PE/CNCF fibers at each draw ratio.*[74]

Some preliminary mechanical analysis shows that the fiber strength improves significantly with increased drawing. After a maximum draw ratio of three, the PE fibrillar structures increased in tensile strength by 231%, while PE/CNCF fibrils increased by 435% as compared to the undrawn samples. A similar trend in the tensile modulus is also observed (i.e., 457% for PE and 1155% for PE/CNCF fibrillar structures). This large increase in strength and modulus further supports the evidence showing an overall increase in orientation for the fibrillar structures during drawing. In addition, the modulus increase for the PE/CNCF hybrid is much more pronounced than that for the PE fibers, and this may be due to the large degree of orientation and population of shish crystals as compared to the drawn control structures. It is also interesting to note that the best mechanical performance occurs in both cases respectively (i.e., PE and PE/CNCF fibers) at a draw ratio of two (Figure 4.5.8). At this draw ratio the SAXS data shows that both kebab and shish crystal growth is very similar (Figure 4.5.6), and may contribute to a more uniform fibrillar morphology and subsequent macro-fiber structure. The decrease in properties of the PE/CNCF fibers (at draw ratio 2) as compared to the control fibers may be due to the presence of non-dispersed CNCF, which act as defects in the fibers.

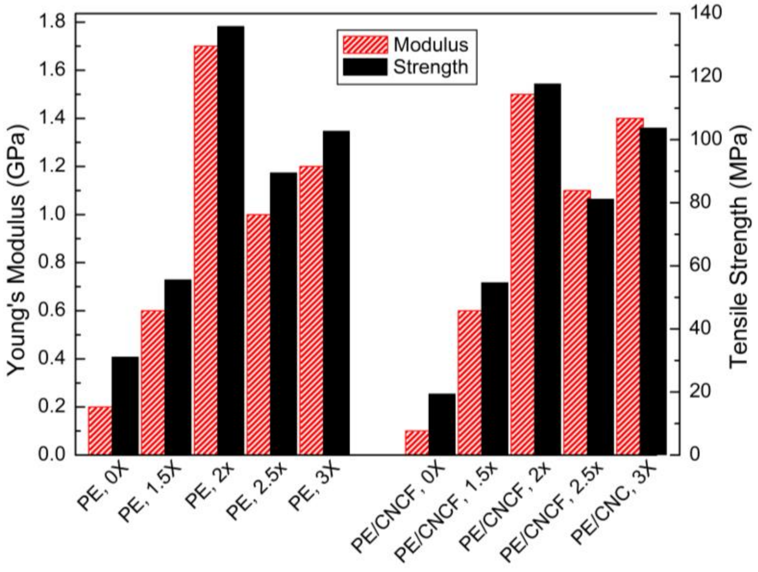

Figure 4.5.8. *Young's modulus (red) and tensile strength (black) of control PE and hybrid PE/CNCF fibers plotted as a function of the draw ratio. The modulus increases by 457% for the control and 1155% for the hybrid at a draw ratio of three. Similarly, tensile strength increases by 231% for the control and 435% for the hybrid at a draw ratio of three.*[74]

The overall mechanical properties for the fibers in this work are fairly low as compared to high-strength composite fibers currently being manufactured today (e.g., Spectra®[85] and Dyneema®[86]), and this may be due to the presence of many voids in the macro-fibers due to the bundling of the fibrillar crystals (Figure 4.5.1). These voids greatly diminish the mechanical properties of the macro-fibers, as both decreased load transfer and imperfections considerably reduce overall fiber strength.

Initial studies on PE shish-kebab crystal growth under shear, has shown that is possible to grow highly ordered (i.e., shish) polymer phases. However, this work shows direct evidence of the ability to use nano-carbons as a template for highly ordered polymer phase formation in hybrid materials. This study also provides the evidence that the rigidity, size, and sliding mechanism of the nano-carbon within the polymer matrix can play a significant role in the formation of a specific type of polymer architecture. These fundamental studies provide insight toward developing processing methods to use nano-carbon fillers as templating materials as well as reinforcements in polymer matrices.

Conclusions

It is important to understand polymer crystallization in order to comprehend and control polymer structures and their resultant properties. In this study PE/CNCF composite fibers were fabricated under shear flow. Subsequent hot drawing took place to further align and orient the polymer chains. The unique interactions between PE and CNCF through crystallization under shear yielded composite fibers with a core/shell structure in which hybrid shish-kebab PE/CNCF crystals were formed. The presence of CNCF was determined through WAXD analysis to increase the orientation of the polymer chains. SAXS analysis also showed extended-chain crystallization was more pronounced in the presence of CNCF. In addition, DSC supported the SAXS evidence of extended-chain crystal structure, and showed that these highly ordered PE crystals are confined by the CNCF. This work adds to the literature which shows the ability for nano-carbons to template extended-chain polymer structures in a composite. These fundamental scientific understandings provide insight in to the underpinnings that affect tailoring specific polymer morphology and properties for various nano-carbon/polymer composite applications.

Study 6: Polyethylene/Boron Nitride Fibers

This study focuses on the fibrillar crystallization of polyethylene in the vicinity of boron nitride (BN) platelets. Due to strong interfacial interactions the polymer is able to induce exfoliation of the BN during stretching. This shows the influence of not only the filler, but the polymer matrix to influence fiber morphology during processing.

Experimental Section

Materials

Hexagonal boron nitride (h-BN) (CAS 10043-11-5, ~1 μm, 98%, $\rho = 2.27$ g/cm^3) was obtained from Sigma-Aldrich. The as-received h-BN was used to form two different boron nitride dispersions which referred as BN-1 and BN-2 in the future. Ethanol (CAS 64-17-5, $M_w = 46.07$ g/mol, ≥99.5%) and xylene (CAS 1330-20-7, $M_w = 106.17$ g/mol, $\rho = 0.86$ g/cm^3) were obtained from Sigma-Aldrich used as-received, Ultrahigh molecular weight polyethylene (UHMWPE) (M_w ~8.7×108 g/mol, $\rho = 0.930$ g/cm^3) was obtained from DSM. For simplicity, from this point PE will be used instead of UHMWPE.

BN-1 dispersions were prepared through sonication of 1500 mg h-BN powder in 50 ml ethanol in (Fisher FS30 bath sonicator, frequency 43 kHz; power, 150 W) for 24 hrs, the dispersion was subsequently centrifuged (Sorvall Legend Micro 21 Microcentrifuge, Ventilated, 120V 60Hz) at 3000 rpm for 90 min. The supernatant (~15 to 40 mg) was finally filtered, collected, and dried in room temperature for 24 h. For composite preparation, the BN-1 powders was added to xylene (0.96 mg/ml) and sonicated for an additional 24 hrs. BN-2 dispersions were prepared by sonication of 48 mg of h-BN powder in 50 ml ethanol (0.96 mg/ml) for 24 hrs. No centrifugation was used. For composite preparation the powders were dried and subsequently added to xylene and sonicated for another 24 hrs.

Fiber Fabrication

Fibers are fabricated using a shear crystallization setup as described in detail elsewhere.[87] The polymer dissolution and crystallization procedure is outlined in Figure 4.6.1a. (i) PE was dissolved in xylenes at concentration of ~0.11 mg/mL using an overhead mechanical stirrer (Eurostar power-b IKA® WERKE stirrer) equipped with a cylindrical stir bar at a speed of 650 RPM and at a temperature of ~140 °C (Figure 4.6.1b). (ii) To fabricate the PE/BN-1 and PE/BN-2 composite fibers, after polymer dissolution, the solution temperature was reduced to ~95 °C and a glass syringe equipped with a 22-gauge blunt tip needle was used to insert 0.8 mL of the freshly sonicated BN-1 or BN-2 dispersions in the polymer solution under shear. This resulted in a fiber consisting of overall boron nitride concentration of 11 wt% to the PE solid content. (iii) Stirring of solution was stopped at ~85 °C for PE/BN-2, ~82 °C for PE/BN-1, and ~78 °C for control PE fibers. This temperature is selected based on the visual cloud-point (Figure 4.6.1b). This cloud-point is shown in Fig. 1c for PE solution at ~78 °C. (iv) After cooling the fibers were collected from the stir bar. Fibers were subsequently hot-drawn at 130 °C.

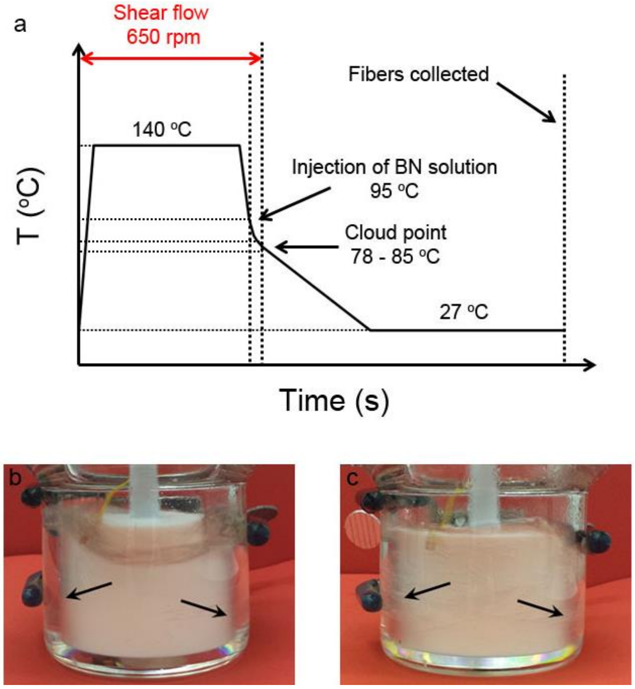

Figure 4.6.1. *(a) Procedure of preparing fibers, (b) solution of PE in xylene at 140 °C and (c) solution of PE at xylene at cloud-point (78 °C) (cloud point selected based on the temperature that solution became cloudy and is not transparent like before). Black arrows added to compare before and after cloud formation.*[88]

Sample Characterization

A Zeiss Supra 25 field emission scanning electron microscope (SEM) (operating voltage, 5 kV) was used for image analysis of the fibers and boron nitride (BN) particles. All samples were sputter coated with gold/palladium before SEM imaging. Wide-angle X-ray diffraction (WAXD) was performed on a Rigaku RAPID II curved detector X-ray diffraction (XRD) system equipped with a 3 kW sealed tube source (voltage, 40 kV; current, 30 mA). WAXD curve fitting and analysis was performed using software's PDXL 2 (version 2.0.3.0) and 2DP (version 1.0.3.4). Small-Angle X-ray scattering (SAXS) was performed on a Rigaku MicroMax-007HF system with CuKα radiation (operation voltage 40 kV and current 30 mA). Tensile tests were conducted using dynamic mechanical analyzer (RSA-G2 series, manufactured by TA instruments) with the gauge length of 10 mm and the extension rate of 0.05 mm/min^{-1}. The number of samples tested ranged from 5 to 8 and the diameter of samples was calculated by weight method using Equation 4.6.1 where *D*, *m*, *l* and ρ are the diameter (mm), mass (mg), length (mm) and density (g/cm^3) of fibers respectively. Density of control PE fiber is density of PE and is equal to 0.930 g/cm^3 and density of composite fibers is 1.293 g/cm^3 and calculated using rule of mixture (Equation 4.6.2) where ρ_{BN}. Raman studies were carried with Jobin Yvon LabRam HR800 at 532 nm excitation wavelength.

$$D = 2\sqrt{m/l\pi\rho} \tag{4.6.1}$$

$$\rho_c = \rho_{BN}\,wt\%_{BN} + \rho_{PE}\,wt\%_{PE} \tag{4.6.2}$$

Results and Discussions

Morphology and Structure

Figures 4.6.2a and 4.6.2b show SEM images of BN-1 and BN-2 particles. The average particles diameter of more than 100 particles was measured to be 241.89 ± 90.92 nm and 329.86 ± 159.41 nm for BN-1 and BN-2 respectively. In general the average diameter of BN-1 particles is smaller than BN-2's and show more uniform diameter size.

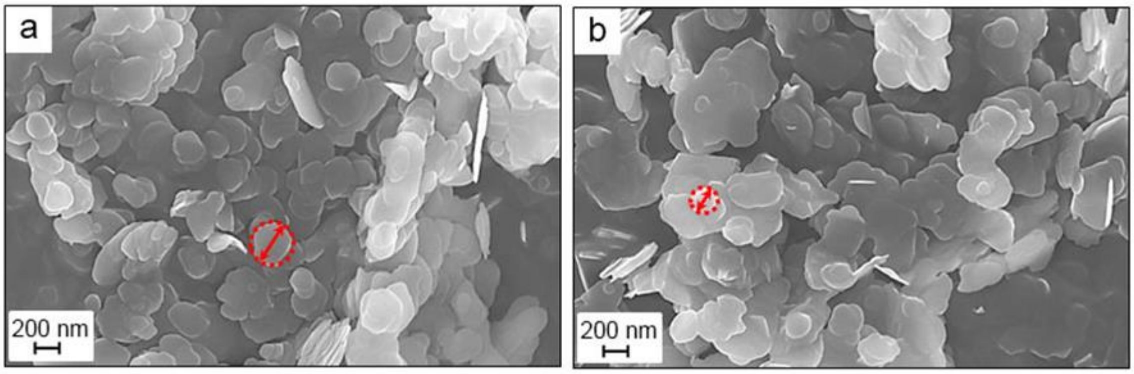

Figure 4.6.2. *SEM images of (a) BN-1 particles with average particles diameter of 241.89 ± 90.92 nm and (b) BN-2 particles with average particles diameter of 329.86 ± 159.41 nm. Red circle and arrow show how the diameter calculated for each particle.*[88]

Figure 4.6.3a shows the WAXD Bragg angle (2θ) versus intensity (I(θ)) curves for BN-1 and BN-2. Sharp diffraction peak occurs at θ = 26.7° and is characteristic of the *(002)* plane of hexagonal boron nitride structure. This plane is associated with the hexagonal boron nitride layer spacing. Figure 4.6.3b shows the Raman spectra of as received h-BN, BN-1, and BN-2 particles using green laser with λ = 532 nm. As-received h-BN and processed BN-1 and BN-2 powders exhibit a characteristic Raman peak at 1368.67 cm^{-1}, 1368.82 cm^{-1} and 1368.42 cm^{-1}, respectively due to E_{2g} phonon mode. E_{2g} is the Raman active mode analogous to G peak in graphene.[89]

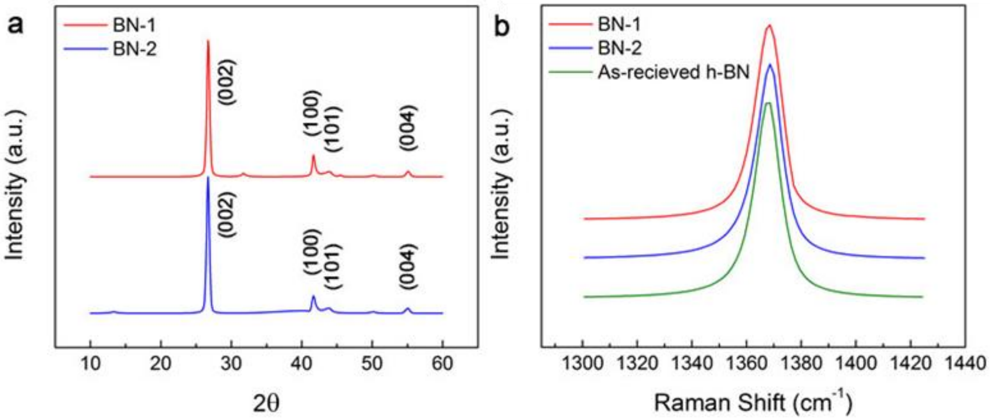

Figure 4.6.3. *(a) WAXD pattern of BN-1 and BN-2 particles and (b) Raman spectra of BN-1, BN-2 and h-BN.*[88]

After preparation of the BN-1 and BN-2 particles, they were incorporated into the composite fibers. Control PE fibers were also processed by shear spinning for comparative studies. All fabricated fibers were collected on the cylindrical stirrer bar. SEM micrographs for all of the control and composite fibers produced in this work are shown in Figure 4.6.4. Figures 4.6.4a_1, 4.6.4b_1 and 4.6.4c_1 show the well-known shish-kebab structure of undrawn PE, PE/BN-1 and PE/BN-2 fibers, respectively. Figures 4.6.4a_2, 4.6.4b_2 and 4.6.4c_2 show the drawn PE, PE/BN-1 and PE/BN-2 fibers, respectively. Long chain polymer molecules like UHMWPE typically crystallize in a folded chain conformation. However under shear crystallization conditions, crystals growth is parallel to the chain direction and leading to the formation of fibrillar type crystals with extended-chain polymer conformation.[90] During shearing according to the coil-stretch theory, longer chains with chain length more than threshold chain length stretch and form a shish structure, (i.e., extended-chain) while the shorter chains aggregate and fold to form a kebab structure.[91-94] Upon hot-drawing of these fibers it was found that the shish-kebab structure converted to an almost completely fibrillar/extended-chain structure due to unfolding of the PE chains.

For the composite fibers, SEM analysis reveals that PE kebabs nucleated and grew on some of the BN particles and they are embedded in the PE matrix. These BN particles are shown by red arrows in Figures 4.6.4b_3 and 4.6.4c_3 for BN-1 and BN-2 particles, respectively. The nucleation and growth of PE kebabs on BN particles enhanced the exfoliation of the BN particles by drawing the composite fibers near melting point (Figures 4.6.4b_2 and 4.6.4c_2). Later WAXD and Raman results show the same manner and indicate the exfoliation of BN particles upon drawing of PE/BN-1 and PE/BN-2 fibers.

As mentioned earlier shearing is stopped at solution temperatures of 78°C, 82°C and 85°C for PE, PE/BN-1 and PE/BN-2 fibers, respectively. These temperatures are selected based on the onset of the visible cloud-point of the solution. It was found that at higher temperatures fiber uniformity in terms of diameter was poor. At the cloud-point temperature the most uniform and continues (> 20 cm) fibers could be formed and collected.

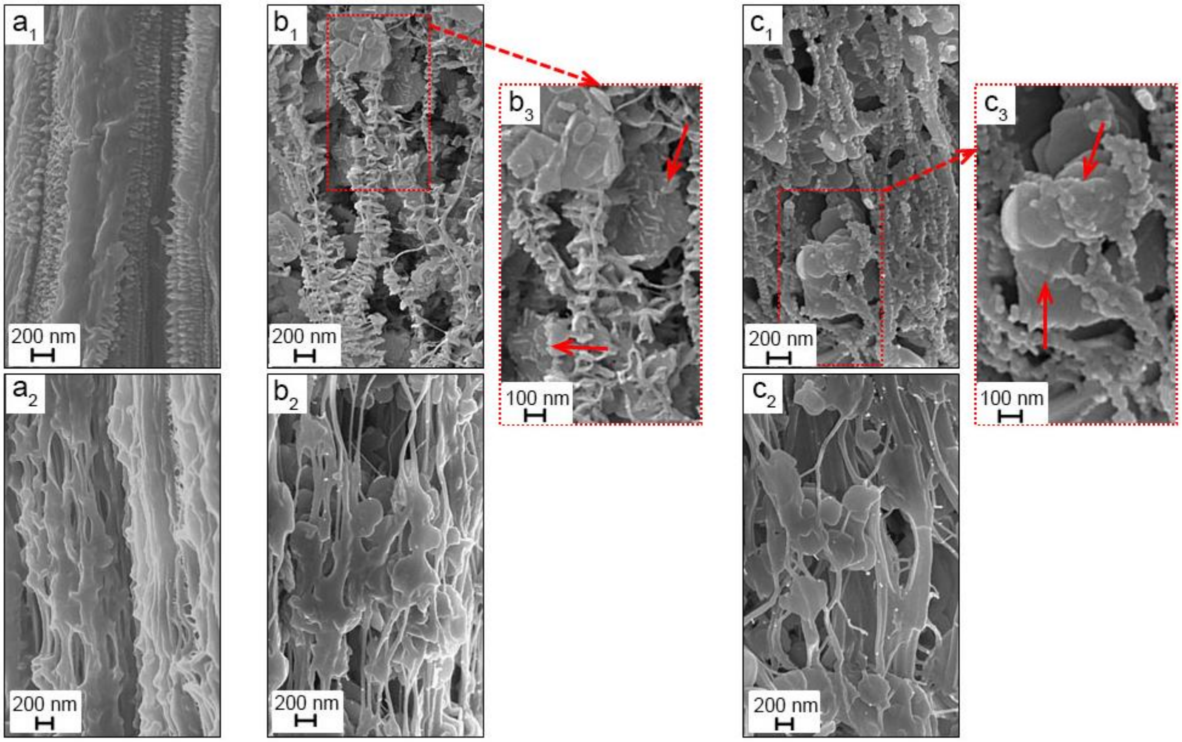

Figure 4.6.4. *SEM images of fabricated fiber. (a_1) shish-kebab structure of undrawn PE fiber, (a_2) fibrillar extended chain (shish) structure of drawn PE fiber, (b_1) shish-kebab structure of undrawn PE/BN-1 fiber, (b_2) fibrillar extended chain structure of PE/BN-1, (b_3) PE kebabs formed on BN-1 particles, (${}_{c1}$) shish-kebab structure of undrawn PE/BN-2 fiber, (c_2) fibrillar extended chain structure of drawn PE/BN-2 fiber, (c_3) PE kebabs formed on BN-2 particles.*[88]

Structure-Property Relationship

Mechanical behavior of the undrawn and drawn fibers of control PE, PE/BN-1 and PE/BN-2 composites are summarized in Table 4.6.1. Young's modulus of undrawn PE fibers increased from 0.27 GPa to 0.55 GPa (204%) and 0.65 GPa (240%) when loaded with BN-1 and BN-2, respectively. Young's modulus of drawn PE fibers increased from 3.01 GPa to 5.67 GPa (188%) and 7.60 GPa (252%) for the PE/BN-1 and PE/BN-2 fibers, respectively. These increases may be related to the better chain orientation observed in the composite fiber in comparison with the control PE fiber. Also diameter distribution of fibers becomes narrower after drawing.

Table 4.6.1. *Mechanical properties of fabricated fibers.*[88]

		E (GPa)	σ (MPa)	ε (%)
Undrawn	PE	0.27±0.2	27.50±10.80	141±94.1
	PE/BN-1	0.55±0.3	102.06±32.84	98±60.5
	PE/BN-2	0.65±0.3	173.75±106.72	57±35.9
Drawn	PE	3.01±0.5	710.5±254.67	39±17.4
	PE/BN-1	5.67±1.3	488.75±148.12	14±3.2
	PE/BN-2	7.60±2.3	605.59±235.34	11±2.6

Comparatively, the tensile strength of undrawn PE fibers increased 371% and 632% with the addition of BN-1 and BN-2, respectively. However, the tensile strength of drawn PE fibers decreased 145% and 117% after loading with BN-1 and BN-2, respectively. It should be noted that the average draw ratio for control fiber was as high as 12, while it only reached 4 for the composite fibers because of breakage. The decrease in tensile strength may be related to the presence of defect sites (i.e., agglomerated boron nitride particles) due to areas of dispersion in the fibers.

WAXD and SAXS pattern of undrawn and drawn PE, PE/BN-1 and PE/BN-2 fibers are shown in Figures 4.6.5a, 4.6.5b and 4.6.5c, respectively. The 2D-WAXD pattern of undrawn PE fiber (Figure 4.6.5a_1) shows the full ring of *(110)* and *(200)* reflections pattern of PE crystals, indicating a random distribution of crystalline lamellae. The 2D-WAXD pattern of undrawn PE/BN-1 and PE/BN-2 fibers (Figures 4.6.5b_1 and 4.6.5c_1, respectively) do not show the full ring of *(110)* and *(200)* reflection pattern of PE crystals, which means PE crystals are not fully random. This can be due to effect of formation of PE on BN particles (shown in SEM images in Figures 4.6.4b_3 and 4.6.4c_3 respectively) in a direction that increases the alignment of undrawn composite fibers. The drawn PE, PE/BN-1 and PE/BN-2 fibers (Figures 4.6.5b_1, 4.6.5b_2 and 4.6.5c_2 respectively) show two equatorial arcs related to *(110)* and *(200)* reflection pattern of PE crystals, characteristic of aligned fiber.

The undrawn and drawn PE/BN-1 and PE/BN-2 fibers (Figures 4.6.5b_1, 4.6.5b_2, 4.6.5c_1 and 4.6.5c_2, respectively) also show equatorial arc related to *(002)* reflection pattern of BN crystals. The BN arcs of drawn PE/BN-1 and PE/BN-2 fibers (Figures 4.6.5b_2 and 4.6.5c_2, respectively) diminished in comparison with undrawn fibers (Figures 4.6.5b_1 and 4.6.5c_1, respectively). Effect of drawing on BN particles is also seen on decrease in the intensity of WAXD profile patterns by drawing in Figures 4.6.5b_3 and 4.6.5c_3, respectively. The diminishing the intensity of WAXD peaks of BN-1 and BN-2 particles show that BN particles exfoliated upon drawing in the composite fibers.

2D-SAXS patterns of undrawn PE, PE/BN-1 and PE/BN-2 fibers are shown in Figures 4.6.5a_4, 4.6.5b_4 and 4.6.5c_4, respectively. A streak along the meridional axis represents kebabs and a streak along the equatorial axis represents shish, since the fiber axis is meridional.[91] 2D-SAXS patterns of drawn PE, PE/BN-1 and PE/BN-2 fibers are shown in Figures 4.6.5a_5, 4.6.5b_5 and 4.6.5c_5, respectively.

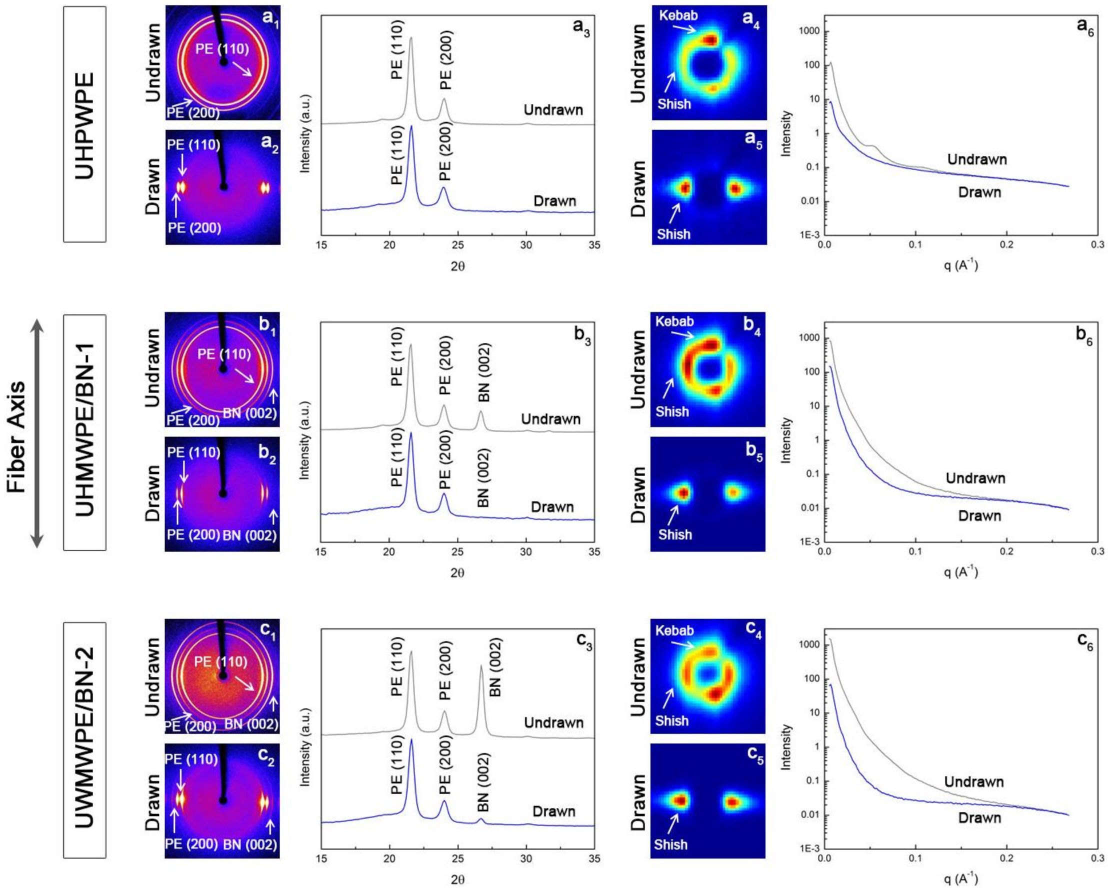

Figure 4.6.5. *(a) WAXD and SAXS pattern of PE: 2D-WAXD pattern of (a_1) undrawn PE, (a_2) drawn PE, WAXD intensity profile of undrawn and drawn PE fiber (a_3), 2D-SAXS pattern of (a_4) undrawn PE, (a_5) drawn PE, SAXS intensity profile of undrawn and drawn PE fiber (a_6), (b) WAXD and SAXS pattern of PE/BN-1: 2D-WAXD pattern of (b_1) undrawn PE/BN-1, (b_2) drawn PE/BN-1, WAXD intensity profile of undrawn and drawn PE/BN-1 fiber (b_3), 2D-SAXS pattern of (b_4) undrawn PE/BN-1, (b_5) drawn PE/BN-1, SAXS intensity profile of undrawn and drawn PE/BN-1 fiber (b_6), (c) WAXD and SAXS pattern of PE/BN-2: 2D-WAXD pattern of (c_1) undrawn PE/BN-2, (c_2) drawn PE/BN-2, WAXD intensity profile of undrawn and drawn PE/BN-2 fiber (c_3), 2D-SAXS pattern of (c_4) undrawn PE/BN-2, (c_5) drawn PE/BN-2 and SAXS intensity profile of undrawn and drawn PE/BN-2 fiber (c_6).*[88]

Raman spectra of all fibers are shown in Figure 4.6.6. PE/BN-1 and PE/BN-2 composite fibers show a BN peak at 1366 cm^{-1}. Upon drawing the intensity of BN peak diminished and show the same manner as seen before for WAXD of composite fibers. BN WAXD peaks are shown in inset of Figure 4.6.6 for comparison. These results confirm that BN particles exfoliated upon drawing for both PE/BN-1 and PE/BN-2 composite fibers.

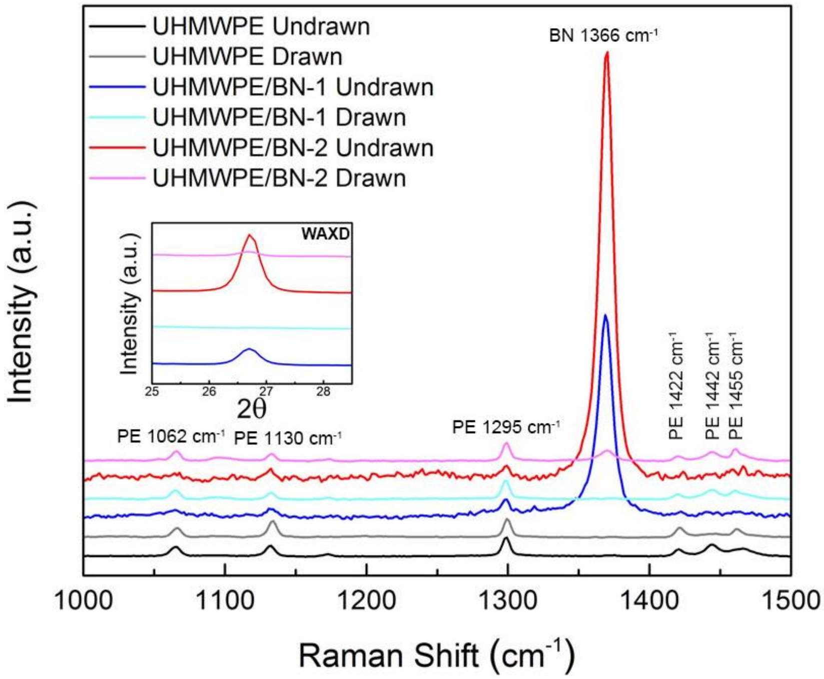

Figure 4.6.6. *Raman spectra of all fibers. Inset: WAXD peaks of BN in composite fibers.*[88]

Herman's orientation factor (*f*) along the fiber axis for all fibers is calculated using Equation 4.6.3 where $\langle \cos^2 \phi_c \rangle$ is defined by Equation 4.6.4 which is according to Wilchinski's approach [95] . ϕ_c is the angle between the fiber direction and the c-axis of orthorhombic PE crystal corresponding to the chain direction. Two planes *(110)* and *(200)* containing the *c*-axis are sufficient for evaluating $\langle \cos^2 \phi_c \rangle$. ρ_a is the angle between the normal of the *(110)* and *a*-axis (56.3°) and ρ_b is the angle between the normal of the *(200)* and b-axis (0°). $\langle \cos^2 \phi_a \rangle$ and $\langle \cos^2 \phi_b \rangle$ calculated using Equation 4.6.5 where ϕ_i can be either ϕ_a or ϕ_b . The term $I(\phi)$ is the diffracted intensity from planes normal to the *a*-axis or the *b*-axis.

$$f = \frac{3\langle \cos^2 \phi_c \rangle - 1}{2} \tag{4.6.3}$$

$$\langle \cos^2 \phi_c \rangle = \frac{(1-2\sin^2 \rho_b)\langle \cos^2 \phi_a \rangle - (1-2\sin^2 \rho_a)\langle \cos^2 \phi_b \rangle}{\sin^2 \rho_a - \sin^2 \rho_b} \tag{4.6.4}$$

$$\langle \cos^2 \phi_i \rangle = \frac{\int_0^{\frac{\pi}{2}} I(\phi)\cos^2 \phi \sin \phi d\phi}{\int_0^{\frac{\pi}{2}} I(\phi)\sin \phi d\phi} \tag{4.6.5}$$

Calculated orientation factors are shown in Table 4.6.2. Undrawn fiber orientation factor increase from 0.56 for PE to 0.68 and 0.69 for PE/BN-1 and PE/BN-2 respectively. Drawn fiber orientation factor of PE is 0.91 and is higher than orientation factor of PE/BN-1 (0.85) and PE/BN-2 (0.87) due to more drawability. These results show that BN particles in undrawn composite fibers act as a template sites by keeping the polymer chain oriented during crystallization and cause the nucleation and growth of shish structure along the fiber axis. Formation of more shish structure for composite fibers was seen as increase in equatorial streak intensity of SAXS pattern for composite fiber in comparison with PE fiber (Figures 4.6.5g and 4.6.5k vs. 4.6.5c). This orientation factors has the same pattern with the values of tensile strength that mentioned earlier.

Conclusions

Based on WAXD and Raman spectroscopy studies of drawn composite fibers it was found that exfoliation of the BN platelets to single layers occured during drawing processes. SEM images illustrate that crystallization of UHMWPE occurs epitaxially on the surface of the BN particles. The polymer-BN interaction was found to contribute exfoliation of BN particles upon drawing. SEM, WAXD, and small angle X-ray scattering studies show that drawing the fibers transitioned the UHMWPE chains from a folded conformation to the extended-chain structure. The force associated with the change in polymer conformation is anticipated to affect the exfoliation mechanism of the platelets.

REFERENCES

1. Hahm, M. G.; Kwon, Y. K.; Busnaina, A.; Jung, Y. J., Structure Controlled Synthesis of Vertically Aligned Carbon Nanotubes Using Thermal Chemical Vapor Deposition Process. *J. Heat Transf.-Trans. ASME* **2011,** *133* (3).
2. Huang, Y. Y.; Ahir, S. V.; Terentjev, E. M., Dispersion rheology of carbon nanotubes in a polymer matrix. *Phys. Rev. B* **2006,** *73* (12), 63-74.
3. Thess, A.; Lee, R.; Nikolaev, P.; Dai, H. J.; Petit, P.; Robert, J.; Xu, C. H.; Lee, Y. H.; Kim, S. G.; Rinzler, A. G.; Colbert, D. T.; Scuseria, G. E.; Tomanek, D.; Fischer, J. E.; Smalley, R. E., Crystalline ropes of metallic carbon nanotubes. *SCIENCE* **1996,** *273* (5274), 483-487.
4. Holland, V. F.; Mitchell, S. B.; Hunter, W. L.; Lindenmeyer, P. H., Crystal structure and morphology of polyacrylonitrile in dilute solution. *Journal of Polymer Science* **1962,** *62* (173), 145-151.
5. Stefani, R.; Chevereton, M.; Garnier, M.; Eyraud, C., Les structures cristallines du polyacrylonitrile. *Academie Des Sciences. Comptes Rendus* **1960,** *251*, 2174.
6. Zhang, Y.; Song, K.; Meng, J.; Minus, M. L., Tailoring Polyacrylonitrile Interfacial Morphological Structure by Crystallization in the Presence of Single-Wall Carbon Nanotubes. *ACS Applied Materials & Interfaces* **2013,** *5* (3), 807-814.
7. Song, K.; Zhang, Y.; Meng, J.; Minus, M. L., Lubrication of Poly(vinyl alcohol) Chain Orientation by Carbon Nano-Chips in Composite Tapes. *J. Appl. Polym. Sci.* **2013,** *127* (4), 2977-2982.
8. Wilchinsky, Z. W., Measurement of Orientation in Polypropylene Film. *J. App. Phys.* **1960,** *31* (11), 1969-1973.
9. Minus, M. L.; Chae, H. G.; Kumar, S., Observations on Solution Crystallization of Poly(vinyl alcohol) in the Presence of Single-Wall Carbon Nanotubes. *Macromol. Rapid Commun.* **2010,** *31* (3), 310-316.
10. Peppas, N. A.; Hansen, P. J., Crystallization kinetics of poly(vinyl alcohol). *J. Appl. Polym. Sci.* **1982,** *27* (12), 4787-4797.

11. Balandin, A. A.; Ghosh, S.; Bao, W. Z.; Calizo, I.; Teweldebrhan, D.; Miao, F.; Lau, C. N., Superior thermal conductivity of single-layer graphene. *Nano Lett.* **2008,** *8* (3), 902-907.
12. Guo, H. N.; Minus, M. L.; Jagannathan, S.; Kumar, S., Polyacrylonitrile/Carbon Nanotube Composite Films. *ACS Appl. Mater. Interfaces* **2010,** *2* (5), 1331-1342.
13. Kuilla, T.; Bhadra, S.; Yao, D. H.; Kim, N. H.; Bose, S.; Lee, J. H., Recent advances in graphene based polymer composites. *Prog. Polym. Sci.* **2010,** *35* (11), 1350-1375.
14. Derek Hull; Clyne, T. W., *Introduction to Composite Materials*. 2nd ed.; Cambridge University Press: Cambridge, 1996.
15. Sakurada, I.; Ito, T.; Nakamae, K., Elastic moduli of the crystal lattices of polymers. *Journal of Polymer Science Part C: Polymer Symposia* **1967,** *15* (1), 75-91.
16. Allen, G.; Bevington, J. C.; Booth, C.; Price, C., Small-angle X-ray Scattering from Crystalline Polymers. In *Comprehensive Polymer Science: The Synthesis, Characterization, Reactions & Applications of Polymers*, 1st ed.; Hall, I. H., Ed. Pergamon Press, cop.: New York, 1990; Vol. 1, pp 674-675.
17. Sakurada, I., *Polyvinyl Alcohol Fibers*. Marcel Dekker, Inc.: New York, 1985.
18. Tasumi, M.; Shimanouchi, T.; Watanabe, A.; Goto, R., Infrared spectra of normal higher alcohols—I. *Spectrochimica Acta* **1964,** *20* (4), 629-666.
19. Fraser, R. D. B., The Interpretation of Infrared Dichroism in Fibrous Protein Structures. *The Journal of Chemical Physics* **1953,** *21* (9), 1511-1515.
20. Song, K.; Zhang, Y.; Minus, M. L., Polymer Interphase Reinforcement in Low Nano-Carbon Content Fibers: Part One –Understanding the Microstructure-Mechanical Property Relationship as a Function of Filler Loading. *Submitted* **2014**.
21. Song, K.; Zhang, Y.; Meng, J.; Green, E.; Tajaddod, N.; Li, H.; Minus, M., Structural Polymer-Based Carbon Nanotube Composite Fibers: Understanding the Processing–Structure–Performance Relationship. *Materials* **2013,** *6* (6), 2543-2577.
22. Bunn, C. W., Crystal Structure of Polyvinyl Alcohol. *Nature* **1948,** *161*, 929-930.
23. Sakurada, I., *Polyvinyl Alcohol Fibers*. Marcel Dekker, Inc.: New York, 1985; p 97-100.
24. Wilchinsky, Z. W., Measurement of Orientation in Polypropylene Film. *Jpn J Appl Phys* **1960,** *31* (11), 1969-1973.
25. Salem, D. R., *Structure Formation in Polymeric Fibers*. 1st ed.; Hanser Gardner Pubns: Cincinnati, OH, 2000.
26. Xu, X.; Uddin, A. J.; Aoki, K.; Gotoh, Y.; Saito, T.; Yumura, M., Fabrication of high strength PVA/SWCNT composite fibers by gel spinning. *Carbon* **2010,** *48* (7), 1977-1984.
27. Minus, M. L.; Chae, H. G.; Kumar, S., Interfacial Crystallization in Gel-Spun Poly(vinyl alcohol)/Single-Wall Carbon Nanotube Composite Fibers. *Macromolecular Chemistry and Physics* **2009,** *210* (21), 1799-1808.
28. Zhang, Y.; Minus, M. L., Characterization and Structural Analysis of Solution-Grown Polyacrylonitrile-co-Methacrylic Acid (PAN-co-MAA) Single Crystals. *Macromolecules* **2014,** *47* (12), 3987-3996.
29. Song, K.; Zhang, Y.; Meng, J.; Minus, M. L., Lubrication of poly(vinyl alcohol) chain orientation by carbon nano-chips in composite tapes. *J. Appl. Polym. Sci.* **2012,** *127* (4), 2977-2982.
30. Menard, H. P., *Dynamic mechanical analysis: a practical introduction*. 2nd ed.; CRC Press Taylor & Francis Group: Boca Raton, 2008; p 240.
31. Meng, J.; Zhang, Y.; Song, K.; Minus, M. L., Forming Crystalline Polymer-Nano Interphase Structures for High-Modulus and High-Tensile/Strength Composite Fibers. *Macromol. Mater. Eng.* **2014,** *299* (2), 144-153.
32. Vollrath, F.; Madsen, B.; Shao, Z. Z., The effect of spinning conditions on the mechanics of a spider's dragline silk. *Proc. R. Soc. Lond. Ser. B-Biol. Sci.* **2001,** *268* (1483), 2339-2346.
33. Vigolo, B.; Penicaud, A.; Coulon, C.; Sauder, C.; Pailler, R.; Journet, C.; Bernier, P.; Poulin, P., Macroscopic fibers and ribbons of oriented carbon nanotubes. *SCIENCE* **2000,** *290* (5495), 1331-1334.
34. Young, K.; Blighe, F. M.; Vilatela, J. J.; Windle, A. H.; Kinloch, I. A.; Deng, L. B.; Young, R. J.; Coleman, J. N., Strong Dependence of Mechanical Properties on Fiber Diameter for Polymer-Nanotube Composite Fibers: Differentiating Defect from Orientation Effects. *ACS Nano* **2010,** *4* (11), 6989-6997.

35. Coleman, J. N.; Khan, U.; Blau, W. J.; Gun'ko, Y. K., Small but strong: A review of the mechanical properties of carbon nanotube-polymer composites. *Carbon* **2006,** *44* (9), 1624-1652.
36. Yu, M. F.; Files, B. S.; Arepalli, S.; Ruoff, R. S., Tensile Loading of Ropes of Single Wall Carbon Nanotubes and Their Mechanical Properties. *Phys. Rev. Lett.* **2000,** *84* (24), 5552-5555.
37. Treacy, M. M. J.; Ebbesen, T. W.; Gibson, J. M., Exceptionally high Young's modulus observed for individual carbon nanotubes. *Nature* **1996,** *381* (6584), 678-680.
38. Natsuki, T.; Tantrakarn, K.; Endo, M., Prediction of elastic properties for single-walled carbon nanotubes. *Carbon* **2004,** *42* (1), 39-45.
39. Ruoff, R. S.; Qian, D.; Liu, W. K., Mechanical properties of carbon nanotubes: theoretical predictions and experimental measurements. *C. R. Phys.* **2003,** *4* (9), 993-1008.
40. Belytschko, T.; Xiao, S. P.; Schatz, G. C.; Ruoff, R. S., Atomistic simulations of nanotube fracture. *Phys. Rev. B* **2002,** *65* (23), 235430.
41. Bunn, C. W., Crystal structure of polyvinyl alcohol. *Nature* **1948,** *161* (4102), 929-930.
42. Brown, I. D., Geometry of O-H...O hydrogen bonds. *Acta Crystallogr. Sect. A* **1976,** *32*, 24-31.
43. Satcurada, I.; Ito, T.; Nakamae, K., Elastic moduli of the crystal lattices of polymers. *Journal of Polymer Science Part C: Polymer Symposia* **1967,** *15* (1), 75-91.
44. Ke, C.; Zheng, M.; Bae, I.-T.; Zhou, G., Adhesion-driven buckling of single-walled carbon nanotube bundles. *JOURNAL OF APPLIED PHYSICS* **2010,** *107* (10), -.
45. Lu, J. P., Elastic Properties of Carbon Nanotubes and Nanoropes. *Phys. Rev. Lett.* **1997,** *79* (7), 1297-1300.
46. Meng, J.; Zhang, Y.; Cranford, S. W.; Minus, M. L., Nanotube Dispersion and Polymer Conformational Confinement in a Nanocomposite Fiber: A Joint Computational Experimental Study. *The Journal of Physical Chemistry B* **2014,** *118* (31), 9476-9485.
47. Plimpton, S., FAST PARALLEL ALGORITHMS FOR SHORT-RANGE MOLECULAR-DYNAMICS. *J. Comput. Phys.* **1995,** *117* (1), 1-19.
48. Dauber-Osguthorpe, P.; Roberts, V. A.; Osguthorpe, D. J.; Wolff, J.; Genest, M.; Hagler, A. T., Structure and energetics of ligand binding to proteins: Escherichia coli dihydrofolate reductase-trimethoprim, a drug-receptor system. *Proteins: Structure, Function, and Bioinformatics* **1988,** *4* (1), 31-47.
49. Chenoweth, K.; van Duin, A. C. T.; Goddard, W. A., ReaxFF reactive force field for molecular dynamics simulations of hydrocarbon oxidation. *J Phys Chem A* **2008,** *112* (5), 1040-1053.
50. Stuart, S. J.; Tutein, A. B.; Harrison, J. A., A reactive potential for hydrocarbons with intermolecular interactions. *J Chem Phys* **2000,** *112* (14), 6472-6486.
51. Brenner, D. W.; Shenderova, O. A.; Harrison, J. A.; Stuart, S. J.; Ni, B.; Sinnott, S. B., A second-generation reactive empirical bond order (REBO) potential energy expression for hydrocarbons. *J Phys-Condens Mat* **2002,** *14* (4), 783-802.
52. Los, J. H.; Ghiringhelli, L. M.; Meijer, E. J.; Fasolino, A., Improved long-range reactive bond-order potential for carbon. I. Construction. *Phys Rev B* **2005,** *72* (21).
53. Cranford, S. W.; Buehler, M. J., Variation of Weak Polyelectrolyte Persistence Length through an Electrostatic Contour Length. *Macromolecules* **2012,** *45* (19), 8067-8082.
54. Cranford, S. W.; Ortiz, C.; Buehler, M. J., Mechanomutable properties of a PAA/PAH polyelectrolyte complex: rate dependence and ionization effects on tunable adhesion strength. *Soft Matter* **2010,** *6* (17), 4175-4188.
55. Wilchinsky, Z. W., Measurement of Orientation in Polypropylene Film. *J. Appl. Phys.* **1960,** *31* (11), 1969 - 1972.
56. Sreekumar, T. V.; Liu, T.; Min, B. G.; Go, H.; Kumar, S.; Hauge, R. H.; Smalley, R. E., Polyacrylonitrile single-walled carbon nanotube composite fibers (vol 16, pg 58, 2004). *Advanced Materials* **2004,** *16* (18), 1583-1583.
57. Wei, C. Y.; Srivastava, D.; Cho, K. J., Thermal expansion and diffusion coefficients of carbon nanotube-polymer composites. *Nano Letters* **2002,** *2* (6), 647-650.
58. Salvetat, J. P.; Briggs, G. A. D.; Bonard, J. M.; Bacsa, R. R.; Kulik, A. J.; Stockli, T.; Burnham, N. A.; Forro, L., Elastic and Shear Moduli of Single-Walled Carbon Nanotube Ropes. *Phys. Rev. Lett.* **1999,** *82* (5), 944-947.
59. Valentino, O.; Sarno, M.; Rainone, N. G.; Nobile, M. R.; Ciambelli, P.; Neitzert, H. C.; Simon, G. P., Influence of the polymer structure and nanotube concentration on the conductivity and

rheological properties of polyethylene/CNT composites. *Physica E-Low-Dimensional Systems & Nanostructures* **2008,** *40* (7), 2440-2445.
60. Ci, L. J.; Bai, J. C., The reinforcement role of carbon nanotubes in epoxy composites with different matrix stiffness. *Composites Science and Technology* **2006,** *66* (3-4), 599-603.
61. Barber, A. H.; Cohen, S. R.; Wagner, H. D., Measurement of carbon nanotube-polymer interfacial strength. *Applied Physics Letters* **2003,** *82* (23), 4140-4142.
62. Liu, L. Q.; Wagner, H. D., Rubbery and glassy epoxy resins reinforced with carbon nanotubes. *Composites Science and Technology* **2005,** *65* (11-12), 1861-1868.
63. Song, Y. S.; Youn, J. R., Properties of epoxy nanocomposites filled with carbon nanomaterials. *E-Polymers* **2004**.
64. Szleifer, I.; Yerushalmi-Rozen, R., Polymers and carbon nanotubes - dimensionality, interactions and nanotechnology. *Polymer* **2005,** *46* (19), 7803-7818.
65. Zaminpayma, E.; Mirabbaszadeh, K., Interaction between single-walled carbon nanotubes and polymers: A molecular dynamics simulation study with reactive force field. *Computational Materials Science* **2012,** *58*, 7-11.
66. Li, Y., Pull-out simulations on interfacial properties of carbon nanotube-reinforced polymer nanocomposites. *Computational Materials Science* **2011,** *50*, 1854 - 1860.
67. J.I.Minchaca, Size and Velocity Characteristics of Droplets Generated by Thin Steel Slab Continuous Casting Secondary Cooling Air-Mist Nozzles. *Metallurgical and Materials Transactions* **2011,** *42B*, 500 - 515.
68. Shokrieh, M. M.; Rafiee, R., Prediction of mechanical properties of an embedded carbon nanotube in polymer matrix based on developing an equivalent long fiber. *Mechanics Research Communications* **2010,** *37* (2), 235-240.
69. Tallury, S. S.; Pasquinelli, M. A., Molecular Dynamics Simulations of Polymers with Stiff Backbones Interacting with Single-Walled Carbon Nanotubes. *J. Phys. Chem. B* **2010,** *114* (29), 9349-9355.
70. Pennings, A. J.; van der Mark, J. M. A. A.; Kiel, A. M., Hydrodynamically induced crystallization of polymers from solution III. *Colloid. Polym. Sci.* **1969,** *237* (2), 336-358.
71. Pennings, A. J.; Zwijnenburg, A., Longitudinal Growth of Polymer Crystals from Flowing Solutions. VI. Melting Behavior of Continuous Fibrillar Polyethylene Crystals. *J. Polym. Sci., Part B: Polym. Phys.* **1979,** *17*, 1011-1032.
72. Minus, M. L.; Chae, H. G.; Kumar, S., Polyethylene Crystallization Nucleated by Carbon Nanotubes under Shear. *ACS Appl. Mater. Interfaces* **2012,** *4* (1), 326-330.
73. Pennings, A. J., Lamellar and fibrillar crystallization of polymers. *Makromol. Chem. Suppl.* **1979,** *2*, 99-142.
74. Green, E. C.; Zhang, Y.; Minus, M. L., Understanding the effects of nanocarbons on flexible polymer chain orientation and crystallization: Polyethylene/carbon nanochip hybrid fibrillar crystal growth. *J. Appl. Polym. Sci.* **2014,** *131* (18), 9235-9245.
75. Zwijnenburg, A.; Van Hutten, P. F.; Pennings, A. J.; Chanzy, H. D., Longitudinal growth of polymer crystals from flowing solutions V." Structure and morphology of fibrillar polyethylene crystals. *Colloid. Polym. Sci.* **1978,** *256* (8), 729-740.
76. Song, K.; Zhang, Y.; Meng, J.; Minus, M. L., Lubrication of Poly(vinyl alcohol) Chain Orientation by Carbon Nano-Chips in Composite Tapes. *J. Appl. Polym. Sci.* **2012,** *127* (4), 2977-2982.
77. Klug, H. P.; Alexander, L. E., *X-Ray Diffraction Procedures For Polycrystalline and Amorphous Materials*. Second ed.; John Wiley & Sons: New York, 1954.
78. Minus, M. L.; Chea, H. G.; Kumar, S., Single wall carbon nanotube templated oriented crystallization of poly(vinyl alcohol). *Polym.* **2006,** *47*, 3705.
79. Garcia-Gutierrez, M. C.; Nogales, A.; Rueda, D. R.; Domingo, C.; Garcia-Ramos, J. V.; Broza, G.; Roslaniec, Z.; Schulte, K.; Davies, R. J.; Ezquerra, T. A., Templating of crystallization and shear-induced self-assembly of single-wall carbon nanotubes in a polymer-nanocomposite. *Polym.* **2006,** *47* (1), 341-345.
80. Somani, R. H.; Yang, L.; Zhu, L.; Hsiao, B. S., Flow-induced shish-kebab precursor structures in entangled polymer melts. *Polym.* **2005,** *46*, 8587-8623.
81. Camarillo, A. A.; Stribeck, N., SAXS Observations of the Oriented Crystallisation of Polyolefines from the Melt. *Fibres Text. East. Eur* **2005,** *13* (5), 27-29.

82. Ran, S.; Zong, X.; Fang, D.; Hsiao, B. S.; Chu, B.; Ross, R., Novel image analysis of two-dimensional X-ray fiber diffraction patterns: example of a polypropylene fiber drawing study. *J. Appl. Crystallogr.* **2000,** *33*, 1031-1036.
83. Liu, K.; Zhang, L.; Liu, H.; Deng, P.; Du, H.; Li, X.; Zhang, J., Recrystallization of shish-kebab structures induced by self-seeding nucleation. *Mater. Lett.* **2013,** *90*, 145-147.
84. Smith, P.; Lemstra, P. J., Ultra-high-strength polyethylene filaments by solution spinning/drawing. *J. Mater. Sci.* **1980,** *15*, 505.
85. Honeywell International, Inc. http://www.honeywell-advancedfibersandcomposites.com/.
86. DSM, http://www.dsm.com/corporate/about/business-entities/dsm-dyneema.html.
87. Minus, M. L.; Chae, H. G.; Kumar, S., Polyethylene Crystallization Nucleated by Carbon Nanotubes under Shear. *Acs Appl Mater Inter* **2012,** *4* (1), 326-330.
88. Tajaddod, N.; Song, K.; Green, E. C.; Zhang, Y.; Minus, M. L., Exfoliation of Boron Nitride particles by Drawing the Ultra High Molecular Weight Polyethylene/Boron Nitride Composite. *Submitted* **2014**.
89. Nemanich, R.; Solin, S.; Martin, R. M., Light scattering study of boron nitride microcrystals. *Phys Rev B* **1981,** *23* (12), 6348.
90. Zwijnenburg, A.; Pennings, A. J., Longitudinal Growth of Polymer Crystals from Flowing Solutions .2. Polyethylene Crystals in Poiseuille Flow. *Colloid Polym Sci* **1975,** *253* (6), 452-461.
91. Nogales, A.; Hsiao, B. S.; Somani, R. H.; Srinivas, S.; Tsou, A. H.; Balta-Calleja, F. J.; Ezquerra, T. A., Shear-induced crystallization of isotactic polypropylene with different molecular weight distributions: in situ small- and wide-angle X-ray scattering studies. *Polymer* **2001,** *42* (12), 5247-5256.
92. Kimata, S.; Sakurai, T.; Nozue, Y.; Kasahara, T.; Yamaguchi, N.; Karino, T.; Shibayama, M.; Kornfield, J. A., Molecular basis of the shish-kebab morphology in polymer crystallization. *Science* **2007,** *316* (5827), 1014-1017.
93. Wang, M. X.; Hu, W. B.; Ma, Y.; Ma, Y. Q., Orientational relaxation together with polydispersity decides precursor formation in polymer melt crystallization. *Macromolecules* **2005,** *38* (7), 2806-2812.
94. I, D.; Muthukumar, M., Langevin dynamics simulations of early stage shish-kebab crystallization of polymers in extensional flow. *J Chem Phys* **2003,** *118* (14), 6648-6655.
95. Wilchinsky, Z. W., Measurement of Orientation in Polypropylene Film. *Journal of Applied Physics* **1960,** *11* (11).
96. Pennings, A. J.; Zwijnenburg, A., Longitudinal Growth of Polymer Crystals from Flowing Solutions .6. Melting Behavior of Continuous Fibrillar Polyethylene Crystals. *J Polym Sci Pol Phys* **1979,** *17* (6), 1011-1032.
97. Economy, J. a. A., A. G., Morphological modification of UHMPE fibers. *Polym Advan Technol* **1994,** *5* (7), 8.
98. Kwon, Y. K.; Boller, A.; Pyda, M.; Wunderlich, B., Melting and heat capacity of gel-spun, ultra-high molar mass polyethylene fibers. *Polymer* **2000,** *41* (16), 6237-6249.
99. Ratner, S.; Weinberg, A.; Wachtel, E.; Moret, P. M.; Marom, G., Phase transitions in UHMWPE fiber compacts studied by in situ synchrotron microbeam WAXS. *Macromol Rapid Comm* **2004,** *25* (12), 1150-1154.
100. Kim, J.; Kim, S. S.; Park, M.; Jang, M., Effects of precursor properties on the preparation of polyethylene hollow fiber membranes by stretching. *J Membrane Sci* **2008,** *318* (1-2), 201-209.
101. Alberola, N.; Cavaille, J.; Perez, J., Mechanical spectrometry of alpha relaxations of high-density polyethylene. *Journal of Polymer Science Part B: Polymer Physics* **1990,** *28* (4), 569-586.